**PSFC/RR-03-1** **DOE-ET-54512-344**

# Visible Spectroscopic Imaging on the Alcator C-Mod Tokamak

C.J. Boswell

February 2003

Plasma Science and Fusion Center
Massachusetts Institute of Technology
Cambridge, MA 02139 USA

This work was supported by the U.S. Department of Energy, Cooperative Grant No. DE-FC02-99ER54512. Reproduction, translation, publication, use and disposal, in whole or in part, by or for the United States government is permitted.

# Visible Spectroscopic Imaging on the Alcator C-Mod Tokamak

by

Christopher James Boswell

B.S., Dickinson College (1996)

Submitted to the Department of Nuclear Engineering
in partial fulfillment of the requirements for the degree of

Doctor of Philosophy in Nuclear Science and Engineering

at the

MASSACHUSETTS INSTITUTE OF TECHNOLOGY

June 2003



Author .....
Department of Nuclear Engineering
February 4, 2003

Certified by .....
James L. Terry
Research Scientist
Thesis Supervisor

Read by .....
Ian H. Hutchinson
Professor of Nuclear Engineering
Thesis Reader

Accepted by .....
Jeffrey A. Coderre
Chairman, Department Committee on Graduate Students

# Visible Spectroscopic Imaging on the Alcator C-Mod Tokamak

by

Christopher James Boswell

Submitted to the Department of Nuclear Engineering
on February 4, 2003, in partial fulfillment of the
requirements for the degree of
Doctor of Philosophy in Nuclear Science and Engineering

## Abstract

This dissertation reports on the development of a diagnostic visible imaging system on the Alcator C-Mod tokamak and the results from that system. The dissertation asserts the value of this system as a qualitative and quantitative diagnostic for magnetically confined plasmas. The visible imaging system consists of six CCD cameras, absolutely calibrated and filtered for specific spectral ranges. Two of these cameras view the divertor region tangentially, two view RF antenna structures and two are used for a wide-angle survey of the vacuum vessel. The divertor viewing cameras are used to generate two-dimensional emissivity profiles using tomography. Three physics issues have been addressed using the visible imaging system: 1) Using two-dimensional emissivity profiles of $D_\gamma$, volumetric recombination rate profiles have been measured and found to have a structure that depends on a poloidal temperature gradient in the outer scrape-off-layer. 2) A camera viewing the inner wall tangentially was used to measure $D_\alpha$ emission profiles. A sharp break in slope of the radial density profile was found at the location of the secondary separatrix near the inner wall by using these profiles and a kinetic model of the neutrals. 3) Two-dimensional emissivity profiles of visible continuum (420-430nm) have been measured and found to be an order of magnitude too large when compared to expected levels from electron-ion bremsstrahlung and radiative recombination. Several atomic and molecular processes have been considered to explain the enhanced continuum. However, none of the considered processes could explain the continuum level without particle densities inconsistent with current modeling efforts. The visible imaging system was also used in identifying the causes of impurity injections during discharges, in identifying the failure of invessel components, and as a monitor of vessel and plasma conditions. Both the physics results and the operational benefits of the visible imaging system show that the system is a valuable quantitative and qualitative diagnostic.

Thesis Supervisor: James L. Terry
Title: Research Scientist

# Acknowledgments

I would like to offer an tremendous amount of thanks to the many people who have helped me through the difficult task of producing this dissertation. Specifically, I would like to thank John Rice and John Goetz for their helpful discussions not only about what eventually made it into this dissertation but also about physics and life in general. Also, Bruce Lipschultz, Brian Labombard, and Spencer Pitcher deserve many thanks for their insight and help in the understanding and direction of this dissertation. Josh Stillerman deserves more thanks than he normally receives. His help on the data acquisition hardware and software made what could have be a very painful process much easier and smoother. I would also like to thank Ian Hutchinson who helped me through my stay at M. I. T. with his advice and criticism. A tremendous amount of thanks and gratitude goes to Jim Terry for everything that he has done for me. I cannot begin to explain all of the help and support that he has given me through the years.

Special thanks go to my family, my mother, father and brother who have always supported me in all of my endeavors, and my wonderful wife, Michelle, who has given me emotional, mental, and spiritual support through everything.

# Contents

# List of Figures

# List of Tables

# Chapter 1

# Introduction

This introduction provides an general overview of the dissertation. A discussion of the visible imaging diagnostics on Alcator C-Mod is presented along with a very brief review of the current visible imaging systems on other tokamaks. The research question is then presented along with its short answer. Finally, a brief summary of the results from the dissertation is discussed.

## 1.1 Background

Visible imaging on Alcator C-Mod began with sets of linear diode arrays filtered for visible light.[59, 30] The imaging system consisted of four viewing arrays all of which, except one, employed 64-channel, linear diode arrays, which were read out serially. Variable frames rates ($\sim$1 Hz to $\sim$3.5 kHz) resulted in an extremely large dynamic range for these detectors. A 35-channel diode array was read out in parallel and tracked fast events. The desired sections of plasma were imaged through windows on re-entrant tubes onto coherent fiber bundles. The bundles did not transmit light usefully below 400nm and were subject to transmission degradation when exposed to neutron or gamma radiation. The images transmitted by each bundle could be viewed in two colors by employing a beamsplitter, lens and interference filter combination before being imaged onto the diode arrays. The interference filters were mounted in wheels and could be selected remotely, allowing for between shot changes of the

spectral lines to be viewed. This system was typically used to observe the brightness profiles of $D_\alpha$ and $C^{+2}$ emission.

Christian Kurz extended the use of the linear diode arrays by tomographically generating two-dimensional emissivity profiles of the visible light.[31] The reconstruction divided the field-of-view into pixels 2.5 cm square in the poloidal plane. Therefore the spatial resolution of the reconstruction was the size of one pixel. The viewing geometry was contained in a matrix and had been modelled accounting for the poloidal and toroidal extent of each individual detector chord. Emissivities were obtained by inverting the matrix in a least-squares sense under the constraints of smoothness and non-negativity. This technique was used on the emission of both $D_\alpha$ and a carbon line.

Aaron Allen used a single camera with a two-dimensional CCD to tomographically generate emissivity profiles.[1] The camera used was a wide-angle view of the vacuum vessel. Only a small region of the images was used to reconstruction the emissivity profiles. The reconstruction technique was similar to the that employed by Kurz, except no smoothness and non-negativity constraints were used. The camera was filtered for $D_\alpha$ emission using a wide bandpass colored glass combination. The emissivity solutions were reconstructed on 1 cm square grid elements, improving the resolution over the linear diode system employed by Kurz.

The technique of using CCD cameras to generate emissivity profiles is also employed by other tokamaks. The DIII-D tokamak in San Diego, California and the JET tokamak in Abingdon, England both employ a visible imaging camera system to generate two-dimensional emission profiles.[15, 24] The DIII-D system employs a lens, fiber image guide, and filter combination to relay the view to a charge induction device (CID) camera. These images are then inverted using a geometry matrix similar to the techniques of both Kurz and Allen. The JET system uses an endoscope to obtain the toroidal view, and a system of beam splitters to allow the observation of three wavelengths simultaneously. The reconstruction technique for the JET system involves using singular value decomposition to solve the matrix problem and then iteratively redistributing the negative values to obtain a non-negative solution.

## 1.2 Research Question

As a natural extension of previous work in visible imaging on Alcator C-Mod, this dissertation answers the question: Can visible imaging spectroscopy be a valuable qualitative and quantitative diagnostic for magnetically confined plasmas? The answer is that visible imaging spectroscopy *is* a valuable diagnostic as evidenced by the physics results and operational benefits obtained by this system, summarized in the following section and discussed in detail in Chapter 4.

## 1.3 Summary of Results

In answering the research question this dissertation presents three physics results and a discussion on the operational benefits of a visible imaging system. The physics results include an explanation of the divertor recombination profiles based on a radial drift induced by a poloidal temperature gradient, analysis of the $D_\alpha$ emission near the inner wall region of the tokamak and the influence the secondary separatrix has on the profiles, and a finding that the level of continuum emission from the divertor is not due to atomic or to a number of considered molecular processes. The discussion of the operational benefits of the visible imaging system focuses on its ability to locate impurity sources, identify failed invessel components and its use as a monitor of plasma and vessel behavior.

Using the technique and physical setup described in sections 4.1 and 4.2 the volumetric recombination rate profiles were measured and found to have a structure that depends on a poloidal temperature gradient in the outer scrape-off layer. The two dimensional volumetric recombination rate profiles where obtained using $D_\gamma$ emissivity profiles from the visible imaging system and electron density and temperature measurements from Langmuir probes and visible spectroscopy. Significant recombination was observed in the private flux region of the divertor during moderate density discharges ($\bar{n}_e \sim 0.8 - 1.9 \times 10^{20}$ m$^{-3}$). Using Braginskii's equations and deriving a radial drift, it was determined that the temperature gradient in the outer divertor

could generate the flux of plasma consistent with the recombination rate observed in the private flux region.

A sharp break in slope of the radial density profile was found at the location of the secondary separatrix near the inner wall of Alcator C-Mod by using $D_\alpha$ emissivity profiles from the visible imaging system and a kinetic neutral code (KN1D [32]). The inboard $D_\alpha$ emission was found to peak near and follow in time the secondary separatrix. The decay lengths of the inboard $D_\alpha$ emission were found to depend on either the neutral mean-free-path (emission decay length towards the plasma core) or on the electron density at the secondary separatrix (emission decay length towards the inner wall). This decay length towards the inner wall begins at the secondary separatrix and is found to be significantly shorter then the decay length on the same flux surfaces on the low-field-side of the plasma core.

Two dimensional visible continuum (420-430 nm) emissivity profiles in the scrape-off layer have been measured and found to be an order of magnitude too large when compared to expected levels from electron-ion bremsstrahlung and radiative recombination based on measured values of electron densities and temperatures. Various atomic and molecular processes were considered in an attempt to explain the continuum level. The atomic processes included: electron-atom bremsstrahlung, $H^-$ attachment, ion-atom bremsstrahlung, and $H_2^+$ attachment. For these processes to generate the level of continuum observed, the atomic density would have to be two orders of magnitude larger than the electron density. The molecular process considered is a radiative dissociation of the deuterium molecule ($a^3\Sigma_g^+ \rightarrow b^3\Sigma_u^+$). The deuterium molecule can decay radiatively from an excited electronic state into an unbound electronic state, thus dissociating the molecule and generating a continuum emission. Two mechanisms for populating the excited state were considered, excitation from ground and cascading decays from $H_2^+$ volume recombination. With both of these mechanisms it was estimated that the $H_2$ and the $H_2^+$ densities would need to be on the same order of the electron density, if the molecular process is the cause of the enhanced continuum. All the above mentioned processes require densities (molecular, atomic, and molecular ion) that are too high when compared to those predicted by

divertor plasma modelling, therefore it is not likely that any of these processes are the cause of the observed continuum emission in the divertor and the cause remains unknown.

Besides physics results the visible imaging system has been shown to have significant operational benefits. The system has been used in identifying the causes of impurity injections during discharges, in identifying the failure of invessel components, and as a monitor of vessel and plasma behavior. There are three main causes of impurity injection in Alcator C-Mod. The injections typically either originate from the RF antenna structure, the Langmuir scanning probes or from the molybdenum protection tiles that line the inside of the vacuum vessel. All of these injections have been observed and are monitored by the visible imaging system. This system has been useful in identifying when certain invessel components fail. Three specific incidents were noted, the bending of a viewing dump, the complete dislocation of a viewing dump, and the breaking and falling of boron nitride protection tiles from an RF antenna structure. In its capacity as a vacuum vessel and plasma behavior monitor, the system is used to observe during electron cyclotron discharge cleaning, during, and after the discharge, sometimes recording the flight of debris around the vacuum vessel after a disruption.

# Chapter 2

# Review of Current Visible Spectroscopic Imaging Techniques

This chapter reviews the current visible imaging systems on tokamaks and gives a review of the two most commonly used algorithms for solving the tomographic problem. Section 2.1 will describe the visible imaging systems on two of the largest tokamaks in the world, the DIII-D tokamak in San Diego, California and the Joint European Torus (JET) in Abingdon, England. Section 2.2 will describe the most commonly used algorithms for solving the linear problem of $Ax = b$, using least squares methods. They are the Singular Value Decomposition (SVD) method and the Conjugate-Gradient method. Section 2.2 will also discuss the advantages and disadvantages of the two algorithms applied to visible imaging.

## 2.1 Review of Current Visible Imaging Systems on Tokamaks

### 2.1.1 DIII-D Visible Imaging System

The DIII-D visible imaging system consists of several components that give a tangential view of the DIII-D divertor region.[15] The tangential view is obtained by the use of a mirror located at the end of a reentrant tube in vacuum. Figure 2-1 shows the

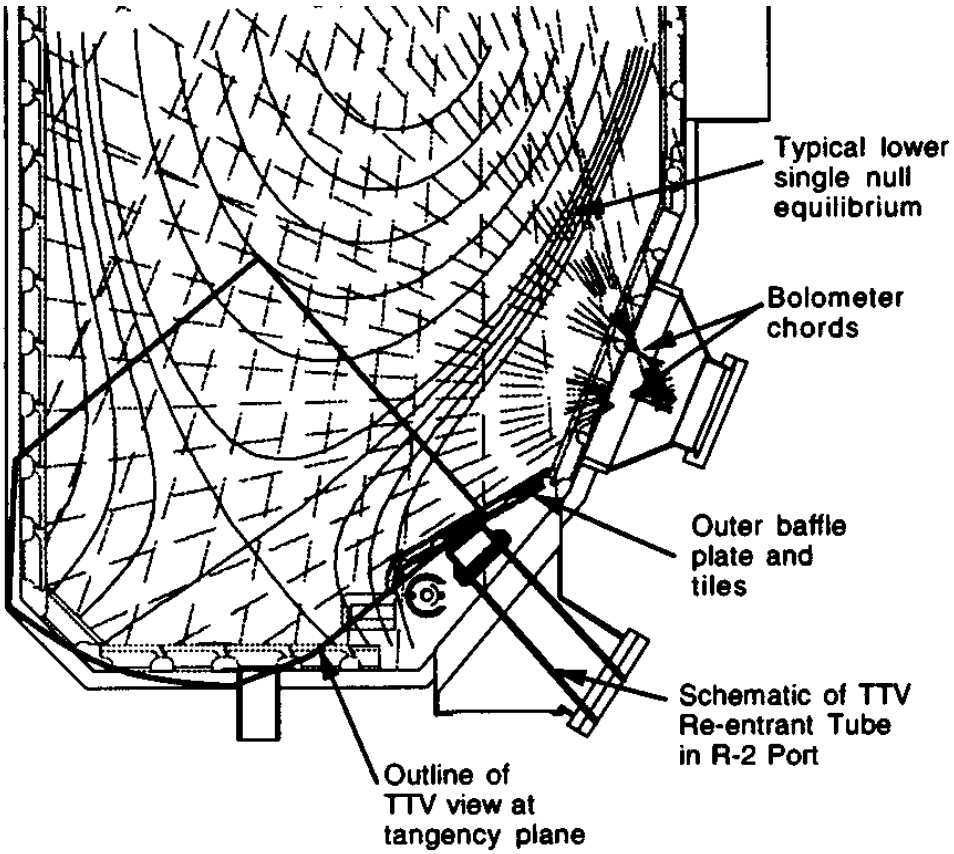


Figure 2-1: Cross section of the lower divertor region of DIII-D showing the location of the DIII-D imaging system reentrant tube and viewing region. [15]

location of the DIII-D imaging system reentrant tube and viewing area. This mirror is protected from the plasma by having the top of the mirror recessed below the level of surrounding carbon tiles. At the vacuum end of the reentrant tube, a vacuum glass window is mounted, allowing all other components of the imaging system to be at atmosphere. The light is brought out of the vacuum vessel through this glass window and then through a lens and fiber image guide. The fiber image guide is coupled to a charge induction device (CID) camera through a series of lenses and a remotely controllable filter changer. Figure 2-2 shows schematically the DIII-D imaging system from the vacuum-side mirror to the CID camera. The images from the CID camera are recorded onto a high quality VHS tape for subsequent digitization. Both the spatial and intensity calibrations are done *in situ* during vents of the DIII-D vacuum vessel.

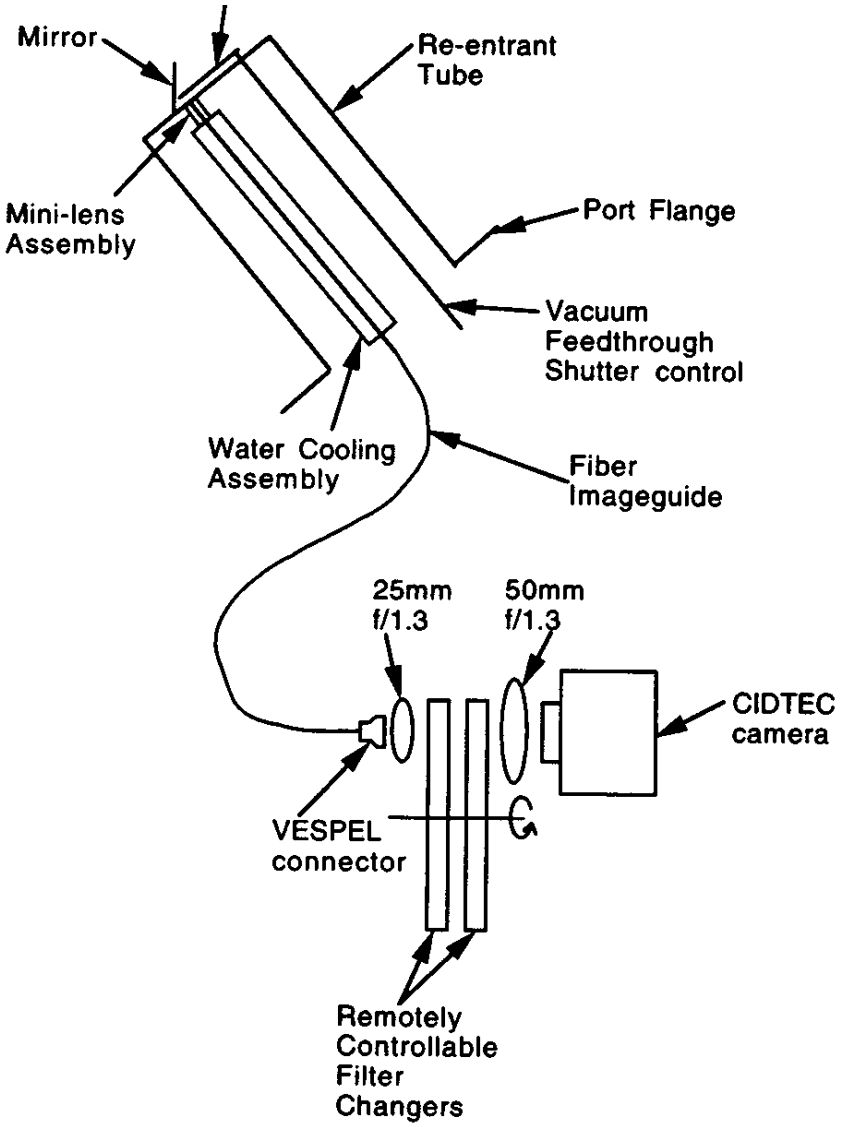


Figure 2-2: Schematic layout of the DIII-D imaging system showing the reentrant tube assembly, the fiber image guide, optics, remotely controllable filter changers, and the CID camera. [15]

The two-dimensional emissivity reconstructions are generated using least squares regression techniques to solve the matrix equation $Ax = b$, where $x$ is the desired two-dimensional emission profile, $A$ is the transformation matrix that takes into account the imaging geometry, and $b$ is the raw data from the CID camera. Due to computer memory constraints, the $512 \times 512$ image array is resampled at $128 \times 128$ and the reconstructed image is generated with a 2 cm resolution. A three-dimensional integral must be evaluated for each matrix element in $A$. These calculations are done using distributed computing techniques on $\sim 45$ workstations across the U.S.

The DIII-D imaging system has several benefits, including the ability to remotely control the spectral line being recorded by the use of filter changers and its nearly horizontal tangential view. A drawback to this system is the possible "browning" of the image guide fibers due to neutron damage. This effect is minimized by removing the image guide when the imaging system is not in use.

### 2.1.2 Joint European Torus Visible Imaging System

The Joint European Torus (JET) also employs a visible imaging system that views the divertor. [24] The JET system uses an endoscope to obtain the toroidal view, and a series of beam splitters to allow the observation of three wavelengths simultaneously. The CCD cameras record images at a rate of 25 frames per second, where each frame is an interleaved image recorded at twice the frequency. Using these interleaved images the JET visible imaging system has a time resolution of 20 ms. Both spatial and intensity calibrations are done using the light from plasma discharges. The spatial calibration is done by comparing the observed locations of the divertor tile gaps and the silhouette of the divertor structure on the camera image to the expected location of these features. The spatial parameters are then solved iteratively for until the expected and observed features overlap on the camera image. The intensity calibration is accomplished by using a visible survey spectrometer, that provides line-of-sight integrated signals through the emission profiles. Using the emission profiles generated from the visible imaging system, data simulations of the visible survey spectrometer signals are created and compared to the actual recorded signals of the

visible survey spectrometer. The comparison between these two signals calibrates the emission profiles. Figure 2-3 shows a simulated view of the divertor with the video grid and a cross-section of the divertor structure with the emission grid.

JET scientists solve the matrix equation $Ax = b$ using singular value decomposition (SVD). Because the resulting emission profile using this technique has negative values–which are non-physical in this problem–a more reasonable solution is constructed by iteratively redistributing the negative values. In this iterative process only the negative elements of the solution are used to reconstruct a virtual brightness negative image. This negative brightness image is inverted again using SVD in which divertor grid elements that originally contained negative elements are constrained to zero. This new negative solution is added to the original solution and the iteration process continues until the absolute value of the negative values is less than 20 percent of the maximum value.

## 2.2 Review of Reconstruction Techniques

The reconstruction problem of visible imaging can be reduced to solving a linear set of equations, $Ax = b$, where $A$ is the relationship between the volumetric emission cells, $x$, and the measured brightnesses, $b$. In all of the previously mentioned systems the number of viewing chords is significantly larger than the number of emission cells. Therefore this linear problem is an overdetermined system, and can be solved by a least-squares method. Of the methods used to solve this problem, the Singular Value Decomposition (SVD) and the Conjugate-Gradient methods are the most commonly used. In this section I will discuss the algorithms for these two methods and the relative benefits and difficulties of using each in visible imaging.

### 2.2.1 Singular Value Decomposition

We desire $x = A^{-1}b$, where $A$ is an $m \times n$ matrix with $m$ indicating the number of brightness chords or views and $n$ indicating the number of emission cells. This problem is solved if $A^{-1}$ can be found. Singular value decomposition (SVD) is one

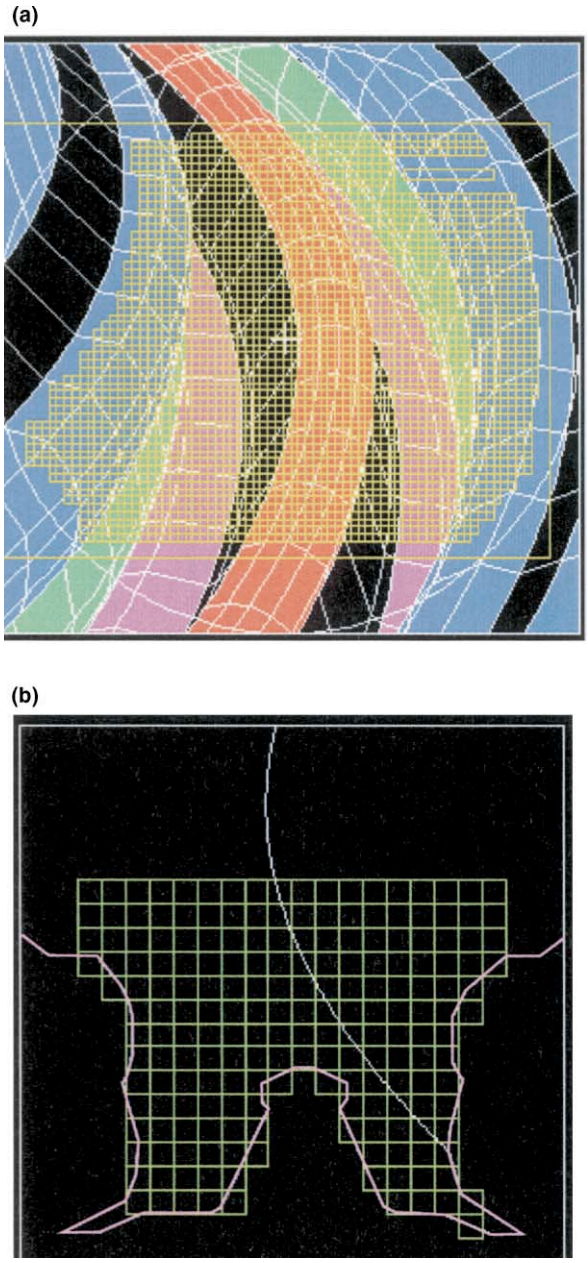


Figure 2-3: (a) A simulated view of the JET divertor with the overlaid video grid. (b) A cross-section of the JET divertor with the overlaid emission grid and a sample trajectory of the video pixel mapped to a poloidal plane. [24]

way to find an estimate of $A^{-1}$. SVD is based on the mathematical theorem that states that any $m \times n$ matrix $A$ can be reduced into three components such that

$$A = U\Sigma V^{\mathrm{T}}, \tag{2.1}$$

where $U$ is an $m \times n$ matrix consisting of $n$ orthonormalized eigenvectors of the $n$ largest eigenvalues of $AA^{\mathrm{T}}$, $V$ is the $n$ orthonormalized eigenvectors of $A^{\mathrm{T}}A$, and $\Sigma$ is a diagonal matrix consisting of the "singular values" of $A$, $\Sigma = diag(\sigma_1, \cdots, \sigma_n)$. With this decomposition, an approximation to the inverse of $A$ can be found to be

$$A^{-1} = V\Sigma^{-1}U^{\mathrm{T}}, \tag{2.2}$$

where $\Sigma^{-1} = diag(1/\sigma_1, \cdots, 1/\sigma_r, 0, \cdots, 0)$, and $r \leq n$ and is the cutoff for singular values. Due to rounding errors in computations, the cutoff value for the singular values is typically taken to be near the relative accuracy for the computer being used. Higher values for the cutoff are taken if it is known that the error in the matrix $A$ is above the rounding error of computer.

The particular algorithm described in this section is based on the algorithm developed by Golub and Reinsch. [16] There is another popular method for computing the SVD of a matrix when $m \gg n$, which is the typical case in the visible imaging systems, and is described by Chan[7]. The algorithm is completed in two parts; the first part creates two sequences of Householder transforms to create a bidiagonal matrix $B$:

$$B = P^{(n)} \cdots P^{(1)} A Q^{(1)} \cdots Q^{(n)} = \begin{bmatrix} x & x & & 0 \\ & \ddots & \ddots & \\ 0 & & x & x \\ 0 & \cdots & & \\ \vdots & \ddots & & \end{bmatrix}. \tag{2.3}$$

Householder transforms are orthogonal and therefore a singular value decomposition

applied to $B$ will yield the same singular values as those of $A$,

$$B = G\Sigma H^{\mathrm{T}} \tag{2.4}$$

$$A = PG\Sigma H^{\mathrm{T}}Q^{\mathrm{T}}, \tag{2.5}$$

where $P = P^{(1)} \cdots P^{(n)}$ and $Q = Q^{(1)} \cdots Q^{(n)}$. Therefore in the final decomposition of $A$, $U = PG$ and $V = QH$.

The second part of the SVD algorithm finds the singular values by diagonalizing $B$ using the QR method,

$$G^{\mathrm{T}}BH = \Sigma. \tag{2.6}$$

Golub[17] discusses the precise methods used in diagonalizing the matrix $B$, as well as some of the necessary subtleties. With this final step, all of the components of the decomposition are known. The inverse can now be found using equation 2.2 and by choosing the appropriate cutoff value for the inverse singular values.

There are two important advantages to using SVD in tomographic reconstruction. The first is that because the geometry matrix, $A$, does not change unless the view of the camera changes, the inverse need only be computed once and applied to all measurements obtained with the same camera view. The other advantage is the amount of information obtained in doing the SVD of the geometry matrix. SVD can be used to estimate the rank, or degrees of freedom of the system, where the number of non-zero singular values is the estimate of the rank. Using this estimate of rank, the effectiveness of the viewing chords can be determined and therefore a system can be devised to improve the tomographic reconstruction by choosing the most effective chords.

There are also two main disadvantages of using SVD in tomographic reconstructions. The first is that SVD is both a computationally intensive and memory intensive process. The number of computations required goes as $2m^2n + 4mn^2 + \frac{14}{3}n^3$ or $2m^2n + 11n^3$ if using the Golub-Reinsch or Chan SVD algorithms, respectively.[7] Problems of the size described in this thesis have $n \sim 2000$ and $m \sim 4000$, creating computations that take prohibitively long on desktop workstations. The other

disadvantage is that this method of doing the tomographic reconstruction will create negative values for the solution due to errors, an unphysical solution. Therefore there is a desire to apply a non-negativity constraint on the solution. Most of the non-negativity algorithms are iterative, and since SVD is computationally intensive to begin with, coupling it with an iterative process will make it more so.

### 2.2.2 Conjugate-Gradient

The conjugate-gradient method of solving the least squares problem $Ax = b$ is to minimize iteratively the function $\phi(x) = \frac{1}{2}x^{\mathrm{T}}Ax - x^{\mathrm{T}}b$. The minimum of the function $\phi(x)$ occurs when $\nabla\phi(x) = Ax - b = 0$. This is the same as finding the solution to $Ax = b$.

The method described here is based on the method published by Hestenes and Stiefel, [19] and a more detailed discussion can be found in Golub. [17] The following discussion will assume that $A$ is a symmetric positive-definite array. If $A$ is not symmetric positive-definite but does have $m > n$, then this algorithm could be used to solve the normal equation $A^{\mathrm{T}}Ax = A^{\mathrm{T}}b$.

The method of steepest descent is the most simple method of minimizing the function $\phi(x)$. In this method one simply steps in the negative direction of the gradient, $-\nabla\phi = b - Ax_k = r_k$ for the $k$th step, until the minimum is found. The successive solutions would be found by $x_k = x_{k-1} + \alpha_k r_{k-1}$, where $\alpha_k = r_{k-1}^{\mathrm{T}} r_{k-1} / r_{k-1}^{\mathrm{T}} A r_{k-1}$. This method may be prohibitively slow if the solution lies in a region of a relatively flat part of a steep sided valley. In this case the steepest decent method would traverse the valley many times before settling on the solution.

An improvement on the steepest decent method would be to choose a direction, $p_k$, that is not equal to the previous residual, $r_{k-1}$, but also not normal to it either, $p_k^{\mathrm{T}} r_{k-1} \neq 0$. Therefore, the successive solutions would be $x_k = x_{k-1} + \alpha_k p_k$, where $\alpha_k = p_k^{\mathrm{T}} r_{k-1} / p_k^{\mathrm{T}} A p_k$.

One such method of choosing the direction to step is to use directions that are

$A$-conjugate with all previous step directions:

$$p_k^{\mathrm{T}} A p_i = 0 \text{ for } i = 1, \cdots, k-1. \tag{2.7}$$

Choosing this property of the step directions requires that the iteration process be finite, and the solution will be found in at most $n$ iterations. When using $A$-conjugate vectors to choose the step directions, several other properties arise between the residuals and the step directions:

1. The residuals are mutually orthogonal and

2. The step direction $p_k$ is a linear combination of the previous residual and the previous step direction, $p_k = r_{k-1} + \beta p_{k-1}$.

Using these properties it can be shown that the $k$th step direction is orthogonal to the $k$th residual, $p_k^{\mathrm{T}} r_k = 0$. Now using these relations we can determine the values of $\alpha_k$ and $\beta_k$,

$$\alpha_k = \frac{r_{k-1}^{\mathrm{T}} r_{k-1}}{p_k^{\mathrm{T}} A p_k}, \tag{2.8}$$

and

$$\beta_k = \frac{p_{k-1}^{\mathrm{T}} A r_{k-1}}{p_{k-1}^{\mathrm{T}} A p_{k-1}}. \tag{2.9}$$

Therefore, an algorithm to find the minimum of the function $\phi$ could be described as

follows.

$$
\begin{aligned}
&x_0 = 0 \\
&\text{For } k = 1, \cdots, n \\
&\quad r_{k-1} = b - Ax_{k-1} \\
&\quad \text{if } r_{k-1} = 0 \\
&\qquad \textit{then} \\
&\qquad\quad \text{Set } x = x_{k-1} \text{and quit.} \\
&\qquad \textit{else} \\
&\qquad\quad \text{If } k = 1 \\
&\qquad\qquad \textit{then} \\
&\qquad\qquad\quad p_k = r_0 \\
&\qquad\qquad \textit{else} \\
&\qquad\qquad\quad \beta_k = -p_{k-1}^{\mathrm{T}} A r_{k-1} / p_{k-1}^{\mathrm{T}} A p_{k-1} \\
&\qquad\qquad\quad p_k = r_{k-1} + \beta_k p_{k-1} \\
&\qquad\quad \alpha_k = r_{k-1}^{\mathrm{T}} r_{k-1} / p_k^{\mathrm{T}} A p_k \\
&\qquad\quad x_k = x_{k-1} + \alpha_k p_k \\
&x = x_n.
\end{aligned}
\tag{2.10}
$$

A problem with this algorithm is that it requires two matrix-vector multiplications per iteration, $Ap_k$ and $Ap_{k-1}$. This can be reduced to one matrix-vector multiplication by using the following relation to calculate recursively the residual,

$$r_k = r_{k-1} - \alpha_k A p_k, \tag{2.11}$$

and substituting

$$r_{k-1}^{\mathrm{T}} r_{k-1} = -\alpha_k r_{k-1}^{\mathrm{T}} A p_{k-1}, \tag{2.12}$$

and

$$r_{k-2}^{\mathrm{T}} r_{k-2} = \alpha_k p_{k-1}^{\mathrm{T}} A p_{k-1} \tag{2.13}$$

into the formula for $\beta_k$. This more efficient algorithm can be written as follows,

$$
\begin{aligned}
&x_0 = 0 \\
&r_0 = b \\
&\text{For } k = 1, \cdots, n \\
&\quad \text{if } r_{k-1} = 0 \\
&\qquad \textit{then} \\
&\qquad\quad \text{Set } x = x_{k-1} \text{and quit.} \\
&\qquad \textit{else} \\
&\qquad\quad \beta_k = r_{k-1}^{\mathrm{T}} r_{k-1} / r_{k-2}^{\mathrm{T}} r_{k-2} \qquad (\beta_1 \equiv 0) \\
&\qquad\quad p_k = r_{k-1} + \beta_k p_{k-1} \qquad (p_1 \equiv r_0) \\
&\qquad\quad \alpha_k = r_{k-1}^{\mathrm{T}} r_{k-1} / p_k^{\mathrm{T}} A p_k \\
&\qquad\quad x_k = x_{k-1} + \alpha_k p_k \\
&\qquad\quad r_k = r_{k-1} - \alpha_k A p_k \\
&x = x_n
\end{aligned}
\tag{2.14}
$$

This final conjugate-gradient algorithm is essentially the algorithm put forth by Hestenes and Stiefel [19]. Since the original formulation of the conjugate-gradient method, several improvements have been made in the stability of the algorithm and required computational time, but all have the above basic algorithm at the core of the routines.

There are several advantages to using the conjugate-gradient method for tomographic reconstructions. First, the least squares solution of the linear problem can be solved much more quickly than SVD. For example, the conjugate-gradient algorithm created by Paige and Saunders[47] requires only $3m+5n$ multiplications per iteration, of which there are at most $n$ iterations. This computation enhancement can be even greater in sparse matrices by using a multiplication algorithm that does not multiply the zero valued elements of the matrices. Second, the conjugate-gradient method requires significantly less memory because it does not need to store the decompositions of the array $A$; only the vector solution, the residual, the step direction, and the original array are required in the calculation. Because the solution can be found sig-

nificantly more quickly than when using SVD, this method is more conducive to being used in non-negativity algorithms, which are desired for tomographic reconstructions.

The conjugate-gradient method also has some disadvantages, of which two are listed here. First, for every time slice a least-squares solution must be found. This may or may not be a significant disadvantage, depending on the level of sparseness of the matrix $A$. One could imagine a sparse enough matrix such that the conjugate-gradient calculation actually requires fewer computations per solution. Next, one obtains almost no information about the geometry matrix. There is no way to mitigate this fact; it is a property of the conjugate-gradient method.

The next two chapters will discuss what has been done on the Alcator C-Mod device. Both methods of reconstruction were investigated, with the conjugate-gradient method being the preferred choice.

# Chapter 3

# Research Question

The research question that this thesis answers is: Can visible imaging spectroscopy be a valuable qualitative and quantitative diagnostic for magnetically confined plasmas? To answer this question I will first define what is meant by a "valuable qualitative and quantitative diagnostic."

A valuable qualitative diagnostic is one that gives a definitive answer as to whether or where an event has occurred and its possible cause. Although it gives no firm numbers with which to determine what has occurred, an example of the visible imaging system on Alcator C-Mod as a valuable qualitative diagnostic would be its use in monitoring the large arcs and impurity injections from RF heating antennas. In this use the cameras viewed the RF antennas and were left unfiltered to record light in the entire visible spectrum. The cameras observed injections in the form of "sparks" emanating from various regions on and around the antennas, such as those shown in figure 3-1. Because the camera was unfiltered and had no ability to determine spectral, distribution it was only able to determine the location of the "spark" and its time of occurrence, not the composition of the injected material. However, the ability to locate the source of the injection was of significant help in determining the cause. The value of such observations, when combined with other information about the antenna behavior, lies in its use in formulating improvements that were made to design of the antennas and the antenna protection structure. These improvements substantially reduced, and in some cases eliminated, the "sparks" altogether. Further

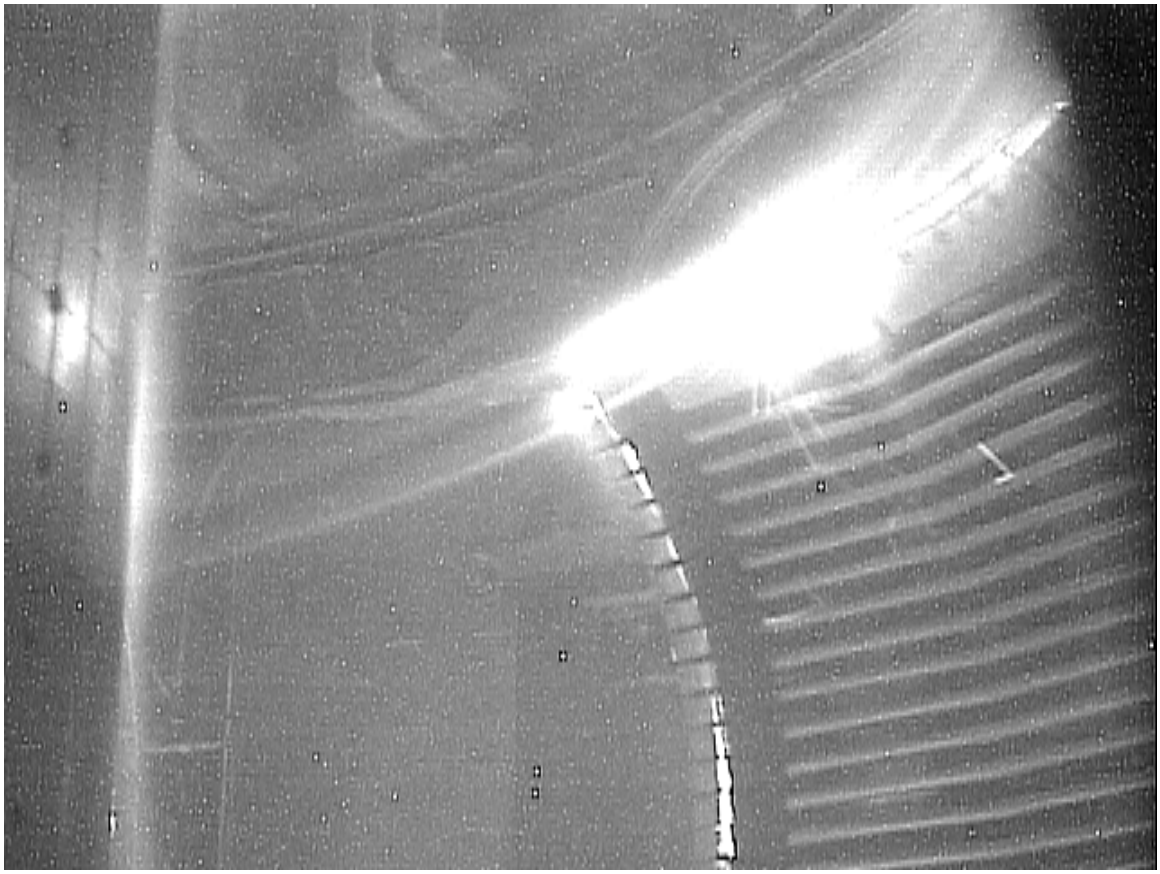

Figure 3-1: Sample camera image showing "sparks" coming from the RF heating antenna structure.

discussion of this example is given in chapter 4.

A valuable quantitative diagnostic yields quantitative information that otherwise would not have been available. An example of the visible imaging system on Alcator C-Mod as a valuable quantitative diagnostic is using it to determine two-dimensional poloidal cross-sections of plasma recombination in the divertor region. Using the system, two-dimensional profiles of the plasma recombination were determined for both attached and detached divertor cases. In both of these cases it was known that recombinations were occurring in the divertor. What was not known was where these recombinations were occurring. The two-dimensional profiles were able to determine quantitatively that in the detached case nearly all of the volumetric recombinations were occurring on common flux surfaces (magnetic flux surfaces corresponding to the scrape-off layer). In the attached divertor operation, a significant number of the

recombinations were occurring in the private flux zone (a region of flux surfaces below the x-point and between the inner and outer divertor legs). Figure 3-2 shows the two-dimensional $D_\gamma$ emission profiles for the attached and detached cases. $D_\gamma$ emission can be used to determine recombination rates and is discussed further in chapter 4. The two-dimensional profiles have since been incorporated into edge- and divertor-modelling programs and have been yielding modelling results that more closely agree with the measurements on Alcator C-Mod. Further examples of the visible imaging system on Alcator C-Mod as a valuable quantitative diagnostic are given in chapter 4.

Although the benefits and difficulties of visible imaging systems on other tokamaks have been discussed in section 2.1, a comparison of those systems to the system employed on Alcator C-Mod is discussed here and summarized in table 3.1. A detailed discussion of the Alcator C-Mod system can be found in chapter 4. There are 8 main categories where the three visible imaging systems differ: number of pixels recorded, ratio of the resolution of reconstructions to the minor radius, the frequency at which fields are recorded, the flexibility of the view, the method of bringing light to the camera, the spectroscopic filtering system, the recording system, and the method of tomographic reconstruction.

In terms of the number of pixels, the resolution relative to the minor radius, and the frequency with which the fields are recorded, the three systems are very similar. The number of pixels are all near each other with the DIII-D system having fewer pixels because the CID chip used is a $512 \times 512$ pixel chip instead of a $640 \times 480$ chip used by Alcator C-Mod and JET. The resolution of the Alcator C-Mod, DIII-D, and JET systems are 0.5 cm, 2 cm, and 3.3 cm respectively. When the resolutions for the various systems are taken as a fraction of their respective minor radii, the similarity in viewing areas can be seen. The difference in terms of frequency of recorded fields between the systems is due to the electrical systems in the United Kingdom (50 Hz) and the United States (60 Hz).

With respect to the flexibility of view, the Alcator C-Mod system has the advantage because it does not rely on mirrors or a fixed viewing location. The view of

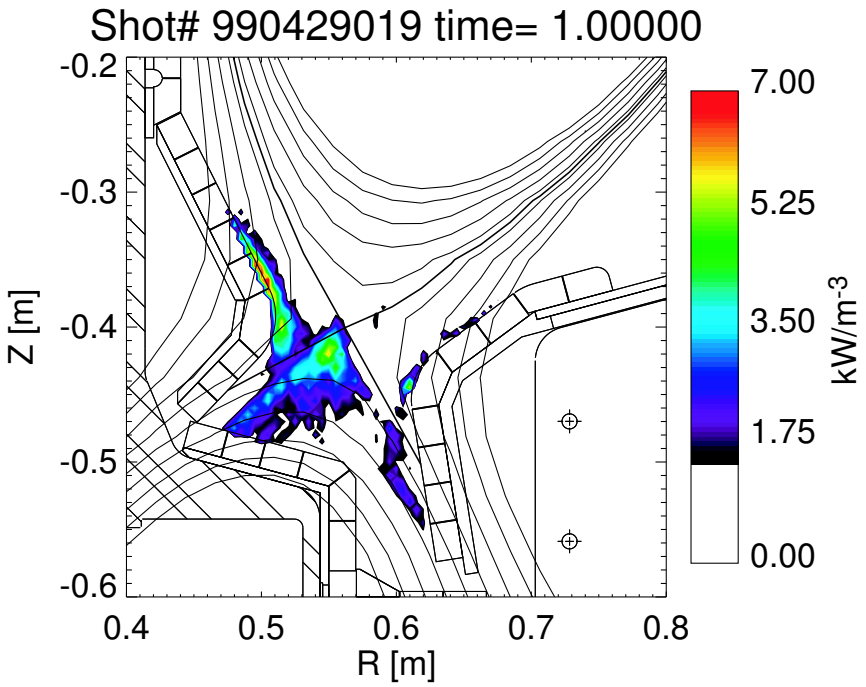


(a)

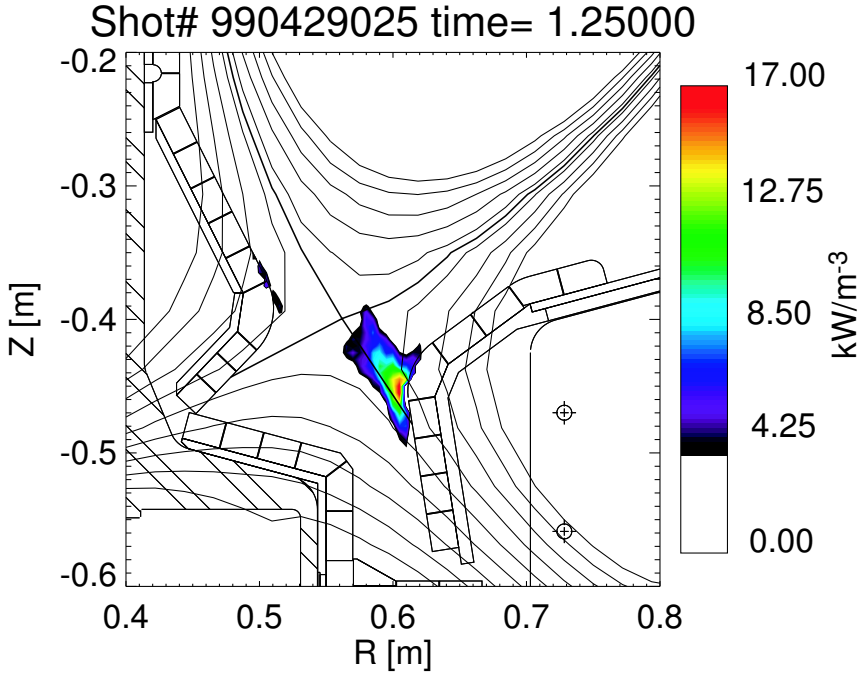


(b)

Figure 3-2: Two-dimensional profiles of $D_\gamma$ emission during (a) attached and (b) detached divertor operation.

| Area of Comparison | Alcator C-Mod | DIII-D | JET |
|---|---|---|---|
| Number of Pixels | 307,200 | 262,144 | 307,200 |
| Resolution / Minor Radius | 0.025 | 0.0357 | 0.0264 |
| Recorded Field Frequency (Hz) | 60 | 60 | 50 |
| Flexibility of View | View can be changed by changing mount | Fixed view | Fixed View |
| How visible light is is brought to camera | Direct camera view | Fiber image guide | Endoscope |
| Filter system | Fixed filter | Remotely controlled filter wheel | Image split with three fixed filter cameras |
| Recording system | Digitized directly to computer | Recorded to VHS tape and then digitized | Digitized directly to computer |
| Tomographic Reconstruction | Conjugate-Gradient | Conjugate-Gradient | SVD with non-negativity |

Table 3.1: Comparison of the visible imaging systems on various tokamaks.

the Alcator C-Mod system can be changed by making simple modifications to the mount. The same cannot be said of the other imaging systems. In terms of how the visible light is brought to the cameras, again, Alcator C-Mod has the advantage. Since the Alcator system uses very small remote head cameras that can be placed inside a re-entrant tube and can obtain a direct view of the plasma of interest. The other systems use either a fiber image guide or an endoscope, both of which can have throughput problems.

In the third category, the spectroscopic filtering system, both the DIII-D and the JET setups have the advantage. In the Alcator C-Mod system the filter is mounted directly in front of the camera lens and cannot be changed without removing the system. The DIII-D system has a remotely controlled filter wheel that allows a change of filter between shots. The JET system simultaneously records three wavelengths; though these cannot be changed between shots, the ability to record three wavelengths is better than being fixed at recording only one.

In final two categories, the three systems are more alike than different. In how the images are recorded, only DIII-D stands out as being different because the sys-

tem records first to a VHS tape before being digitized to a computer, while the JET and Alcator C-Mod systems digitize directly to the computer. Both Alcator C-Mod and the DIII-D systems use conjugate-gradient system to generate tomographic reconstructions, while the JET system employs SVD with an iterative non-negativity routine as described in section 2.1.

Although I have alluded to the fact that the answer to the posed research question is affirmative, the details of that affirmative answers will be shown in chapter 4. The evidence for how visible imaging spectroscopy can be a valuable quantitative diagnostic for magnetically confined plasmas is given by the physics results in sections 4.3.1, 4.3.2, and 4.3.3, and the evidence for how visible imaging spectroscopy can be a valuable qualitative diagnostic is given in section 4.4.

# Chapter 4

# Visible Imaging System of the Alcator C-Mod Tokamak

## 4.1 Physical Setup

On Alcator C-Mod there are six CCD cameras used in the analysis of either emission distribution or impurity injection. Of these six cameras two tangentially view the divertor region (DIV1, DIV2) and are used to obtain two-dimensional emission profiles, two view ICRF antennas (DANT, JANT) and are used to determine impurity injection location, and two cameras view have a wide-angle view of the tokamak (WIDE1,WIDE2). All six of the CCD cameras are off-the-shelf remote-head "pencil" cameras.[60] The cameras are 7 mm in diameter, 40 mm in length and a 3 or 10 m cable connects the camera to the electronics controlling its output. The cameras have an electronic shutter that can be remotely controlled through a serial port connection to a personal computer to allow exposures between 1/10,000 to 1/60 of a second. The images recorded by the personal computers have $640 \times 480$ pixels. The output from the camera control units (CCU's) is a video signal in NTSC format.[25]

Five of the six cameras are mounted in aluminum holders and affixed to a G-10 platform inside a reentrant tube and behind a shuttered quartz window 10 cm from the last closed flux surface of the Alcator C-Mod plasma. The sixth camera (WIDE2) is mounted 180° around the tokamak in a reentrant tube viewing the vessel with a

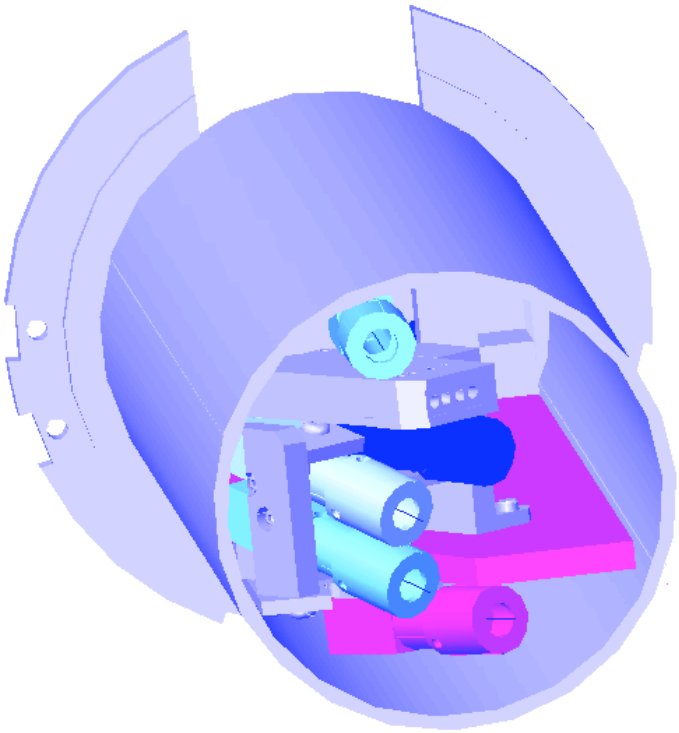

Figure 4-1: Five of the six CCD cameras used on Alcator C-Mod, their location and support structure inside the reentrant tube.

similar view as WIDE1 and also $\sim$ 10 cm from the last closed flux surface. Being mounted in the reentrant tube places the cameras inside the toroidal field coils and exposes the cameras to magnetic fields of up to $\sim$5.4 T. Fig. 4-1 shows the location of the cameras in the reentrant tube. Fig. 4-2 shows the top view of the tokamak with the typical view each of the cameras, with the WIDE2 camera having the same view as is shown in this figure, except displaced toroidally by 180°. A poloidal cross-section of the view of each camera is shown in figure 4-3.

The positions and views of the cameras are confirmed by fitting identifiable features (e.g., the vertical spacing between divertor tiles) with known positions inside the machine to their predicted positions in the view, using the image_divertor2 IDL[23] procedure. Due to disruptions and the occasional removal of the cameras for filter

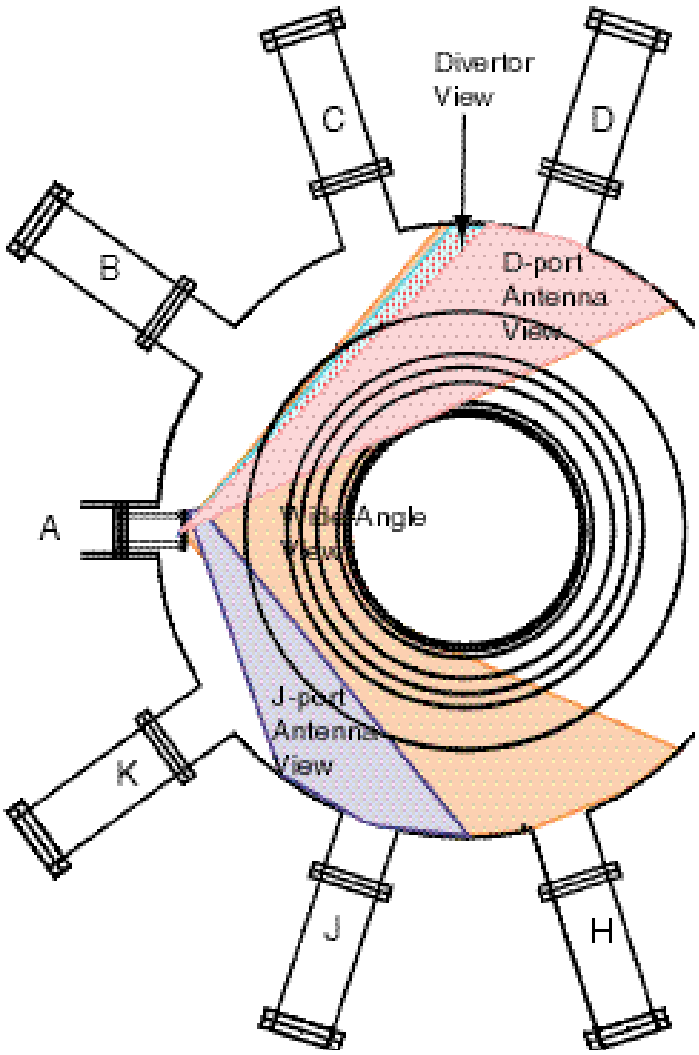


Figure 4-2: The view of each of the five cameras from figure 4-1, labeled accordingly.

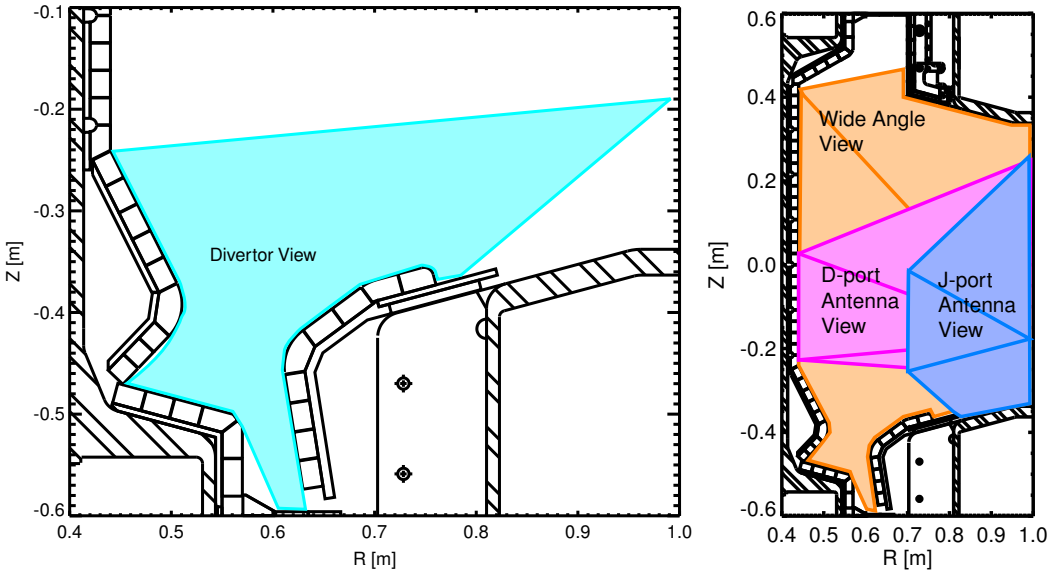


Figure 4-3: Poloidal cross-section of the area viewed by (a) the divertor cameras, (b) the camera viewing the D-port antenna, the camera viewing the J-port antenna, and the wide-angle viewing cameras.

changes the views can move by several degrees during a campaign. Therefore, the best method for calibrating the camera view is to compare the observed location of identifiable features during a disruption frame to expected location of those features and iteratively solving for the parameters that describe the location and view of the camera. This yields an accuracy of better than 1 millimeter at the tangency point of the chordal views. There are five independent parameters that describe the location of the effective lens and view of each cameras, the camera's vertical location, $Z$, its radial location, $R$, and the three angles used to describe the yaw, pitch, and roll, $(\theta_1, \theta_2, \theta_3)$. The toroidal location is not needed since the emission recorded is assumed to be toroidally symmetric. The vertical position is the distance from the midplane of the tokamak, and the radial position is the distance from the center of the tokamak. The angles are all referenced from a horizontal view looking radially inward. Figure 4-4 graphically shows the five parameters needed to determine the location and view of the cameras. Since the plasma emission is assumed to be toroidally symmetric the angular location of the camera around the tokamak is unnecessary. Figure 4-5 shows an example of a plasma frame with the expected location of tile spacings overlaid.

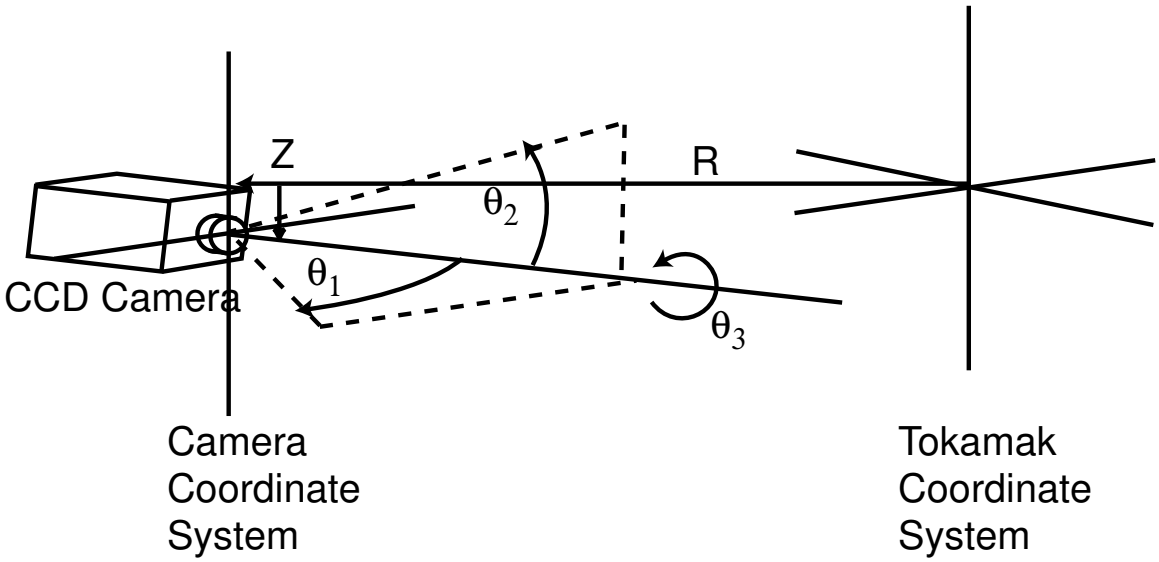


Figure 4-4: Graphical representation of five parameters needed to determine the camera view with respect to the tokamak coordinates.

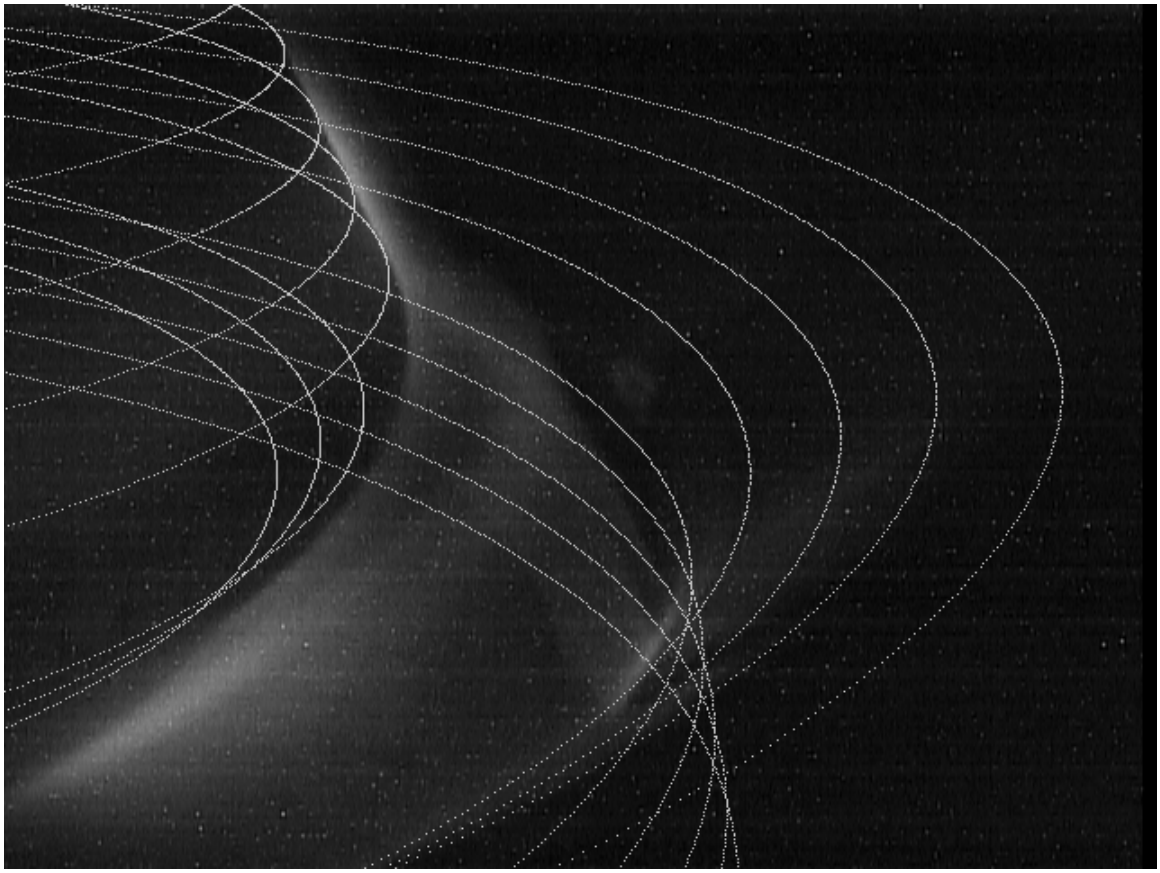

Figure 4-5: An example of a plasma frame with the location of the tile spacings overlaid.

The cameras can be spectrally filtered for emission within a particular wavelength range. This is done by placing an interference filter or color-glass filter, in the case of the wide-angle camera, in front of the lens of each camera. The spectral bandpass of an interference filter is a function of the angle of incidence. The wavelength of the center of the bandpass, $\lambda_\theta$, is

$$\lambda_\theta = \lambda_o \left(1 - \frac{n^2}{2n_*^2} \sin^2 \theta\right), \tag{4.1}$$

where $\theta$ is the angle of incidence, $\lambda_o$ is the center of the bandpass when $\theta = 0$, $n$ is the index of refraction in the medium surrounding the interference filter, in this case air, and $n_*$ is the effective index of refraction in the interference filter, the shape of the filter function changes negligibly with the incidence angle.[43] Using Eq. (4.1) interference filters are chosen such that the spectral line of interest is within the bandpass for all possible viewing angles of the cameras. The viewing angle dependence on the transmission of a desired wavelength due to the interference filter is taken into account when the camera is absolutely calibrated.

In the case where the desired measurement is an emission line, two calibrations are done, 1) to determine the transmission function over the entire field-of-view of the camera and 2) to determine the absolute sensitivity of each camera chord measured by each pixel to a given incident energy for a given filter/lens combination. The first calibration is done by knowing the filter function of an interference filter, angle of incidence of a viewing chord, and the wavelength of the desired line. Since the shape of the filter function of the interference filter changes negligibly over the angles of incidence of interest the transmission for the desired spectral line can be calculated using the known filter function and equation 4.1. This calculation is then checked by scanning a lamp of the element of interest (i.e., deuterium for the calibration for deuterium lines) across the view of the camera and comparing the measured relative intensities with the expected values. Figure 4-6 shows the transmission of the $D_\alpha$ spectral line across the CCD chip for one of the divertor viewing cameras.

The absolute calibration is done by mapping the measured pixel value recorded

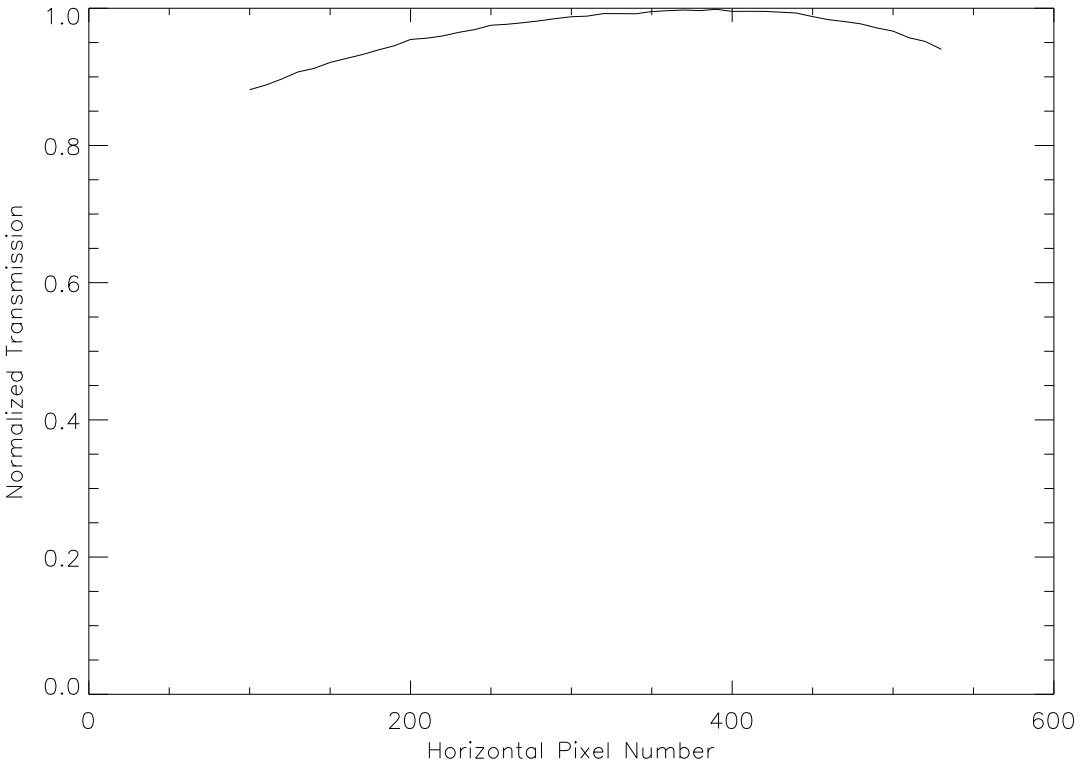


Figure 4-6: The transmission of the $D_\alpha$ spectral line across the center of the CCD chip for one of the divertor viewing cameras.

by the camera when observing a calibrated continuum source of spatially uniform brightness [37]. The basic relation between the measured pixel value and the applied brightness is,

$$B = \frac{C}{A_{\text{pixel}}\Omega}\frac{10^{ND}}{t_{\text{int}}}P, \tag{4.2}$$

where $B$ is the brightness incident on a given pixel, $C$ is the Joules/pixel value constant, $A_{\text{pixel}}$ is the area of the pixel, $\Omega$ is the solid angle of the pixel view, $ND$ is the neutral density of the the neutral density filter placed in-front of the camera, $t_{\text{int}}$ is the integration time of the pixel, and $P$ is the pixel value recorded by the personal computer and has integer values between 0 and 255. We can relate the pixel values measured when observing the plasma to an absolute brightness value by taking the ratio of equation 4.2 for the calibrated brightness and the for the plasma brightness and solving for the plasma brightness yielding,

$$B_{\text{pla}} = \left(\frac{t_{\text{cal}}}{10^{ND_{\text{cal}}}}\frac{B_{\text{cal}}}{P_{\text{cal}}}\right)\frac{10^{ND_{\text{pla}}}}{t_{\text{pla}}}P_{\text{pla}} \tag{4.3}$$

where the subscript "cal" refers to quantities used when recording the images of the calibrated source and the subscript "pla" refers to the quantities used when observing the plasma. Since in the calibration the brightness measured is the integrated product of the filter function and the continuum spectral brightness of the source,

$$B = \int b\left(\lambda\right) T\left(\lambda\right)\ d\lambda. \tag{4.4}$$

In the case of the uniform brightness source this can be approximated as,

$$B_{\text{cal}} = \langle b_{\text{cal}}\rangle \int T\left(\lambda\right)\ d\lambda, \tag{4.5}$$

where $\langle b_{\text{cal}}\rangle$ is the average spectral brightness of the uniform brightness source in the filter function with the units of $\text{Wm}^{-2}\text{ster}^{-1}\text{nm}^{-1}$. In the case of the plasma where a spectral line is present the brightness can be written as,

$$B_{\text{pla}} \quad = \quad \int \left[b_{\text{pla,line}}\delta(\lambda - \lambda_o) + b_{\text{pla,cont}}\right] T\left(\lambda\right)\ d\lambda$$

$$= \quad b_{\text{pla,line}} T(\lambda_o) + b_{\text{pla,cont}} \int T(\lambda)\ d\lambda, \tag{4.6}$$

where $b_{\text{pla,line}}$ is the brightness of the line of interest at $\lambda_o$, and $b_{\text{pla,cont}}$ is the continuum spectral emission from the plasma in units of $\text{Wm}^{-2}\text{ster}^{-1}\text{nm}^{-1}$. Substituting equations 4.5 and 4.6 into equation 4.3 and solving for the brightness of the line of interest yields,

$$b_{\text{pla,line}} = \left[ \left( \frac{t_{\text{cal}} \langle b_{\text{cal}} \rangle}{10^{ND_{\text{cal}}} P_{\text{cal}}} \right) \frac{10^{ND_{\text{pla}}}}{t_{\text{pla}}} P_{\text{pla}} - b_{\text{pla,cont}} \right] \frac{\int T(\lambda)\ d\lambda}{T(\lambda_o)}. \tag{4.7}$$

For the case of deuterium line emission in a deuterium plasma, the $b_{\text{pla,cont}}$ can be neglected and the equation that yields the brightness of the desired line from the pixel value of the camera is

$$b_{\text{pla,line}} \approx \left( \frac{t_{\text{cal}} \langle b_{\text{cal}} \rangle}{10^{ND_{\text{cal}}} P_{\text{cal}}} \right) \frac{10^{ND_{\text{pla}}}}{t_{\text{pla}}} P_{\text{pla}} \frac{\int T(\lambda)\ d\lambda}{T(\lambda_o)}. \tag{4.8}$$

All "cal" terms, except the pixel value ($P_{\text{cal}}$), are known for every pixel on the CCD chip. The pixel value ($P_{\text{cal}}$) is measured by recording 30 frames viewing the uniform brightness source and averaging the pixel value over those 30 frames. The filter function, $T(\lambda)$, is measured using the filter, a continuum brightness source, and a visible spectrometer. Figure 4-7 shows the measured filter function for the $D_\alpha$ filter used. All other terms are measured ($P_{\text{pla}}$) or chosen ($ND_{\text{pla}}, t_{\text{pla}}$) during the experiments. Figure 4-8 shows the calibration factor ($\frac{t_{\text{cal}} \langle b_{\text{cal}} \rangle}{10^{ND_{\text{cal}}} P_{\text{cal}}} \frac{\int T(\lambda)\, d\lambda}{T(\lambda_o)}$) for the $D_\alpha$ camera. This means that for $D_\alpha$ brightnesses typical of the divertor, $\sim 10^4$ $\text{Wm}^{-2}\text{ster}^{-1}$, an ND filter of 4 was used, where as for typical main chamber brightnesses, $\sim 100$ $\text{Wm}^{-2}\text{ster}^{-1}$, an ND filter of 2 was used.

All six cameras are synchronized and recorded on two personal computers. Each computer is equipped with a three color frame-grabber that is set-up to record three cameras simultaneously (instead of three colors). The recorded camera data is then saved to the hard drive of the local computer in an MDSplus[54] data tree structure or to the main experiment's MDSplus data tree structure for easy retrieval from the Alcator C-Mod data analysis system. The data saved to the local hard drive is then

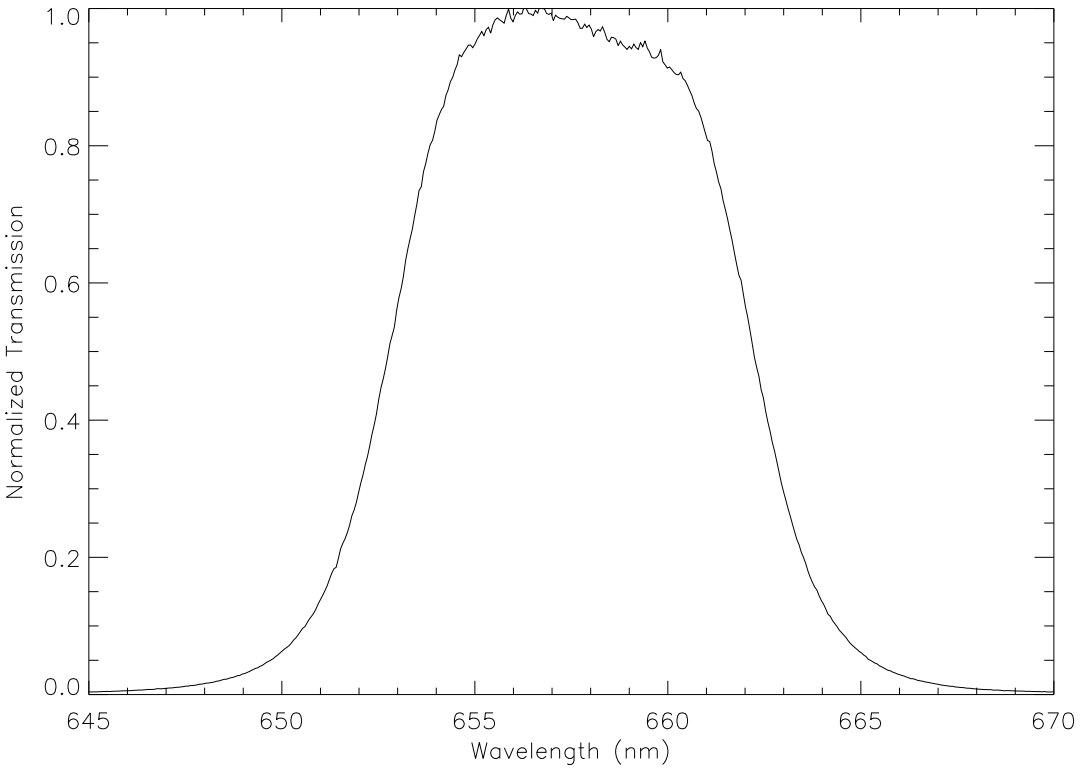


Figure 4-7: The measured filter function for the $D_\alpha$ filter used.

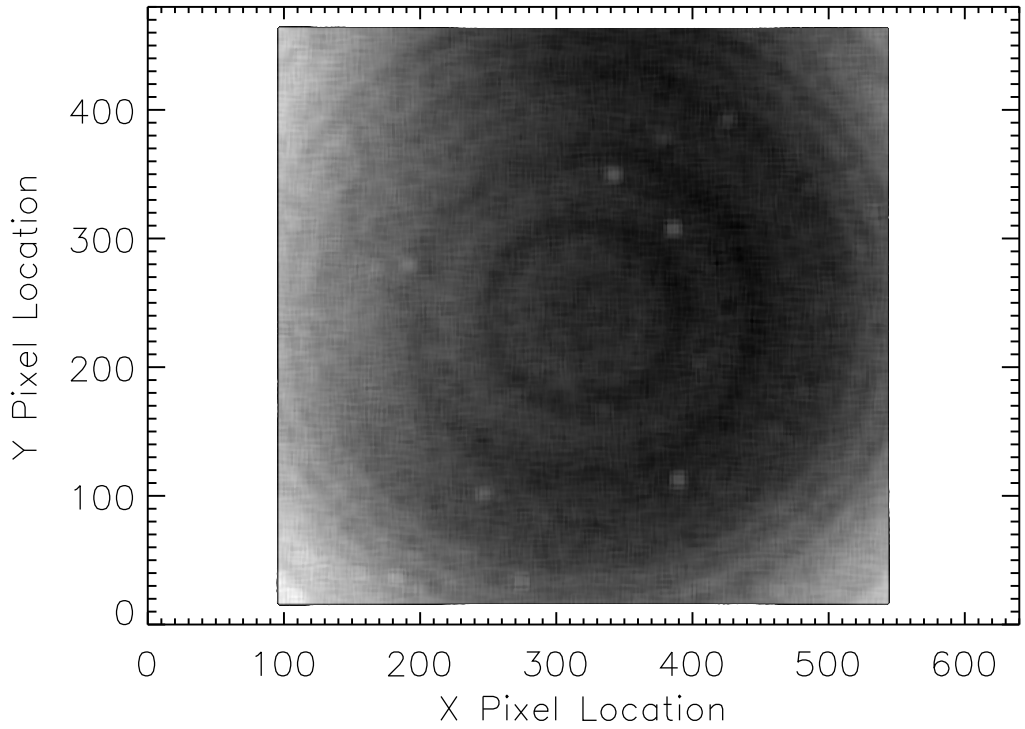


Figure 4-8: The calibration factor for the $D_\alpha$ camera. The variation is in a linear gray scale and has a minimum value of 0.0161 and a maximum value of 0.0201 W $m^{-2}$ $ster^{-1}$ Pixel $Value^{-1}$.

periodically transferred to compact discs for archiving. The output from the CCD cameras is in NTSC format, which limits the frame rate to 30 per second. In this format a frame is made of two interlaced fields recorded at twice the frame rate of the camera. Therefore each recorded frame has two recorded time steps (one in each field, separated in time by 16.7 ms) and therefore brightness data is obtained at 60 Hz.

## 4.2 Data Analysis for Divertor Viewing Cameras

The two cameras viewing the divertor are used to obtain two-dimensional emission profiles of the divertor. As was described in Sec. 4.1, the view of the camera and therefore the view of the individual pixels are calibrated and known. Because of this it is possible to model the views of the pixels through a region of the divertor and obtain two-dimensional profiles of emission. In order to create this model the emission region must be discretized into finite-sized elements. The size of the emission elements determines the spatial resolution of the emission profile. The only fundamental limit on the size of the emission elements is the spacing of the pixel views used. Another constraint that can be added to ease calculations is that the emission elements must be several times larger than the projection of the solid angle of a pixel view through the emission elements. This constraint allows the use of the thin-chord approximation, which assumes that each camera pixel view is a line integral through the emission region of the divertor. Using an 8mm focal length lens for these cameras, the projections of the camera pixels are less than 0.7 mm wide at any point in the emission region and the inversion box size or emission element size used is 5 mm wide. Therefore, the thin-chord approximation is valid.

The emissivity, $\varepsilon$, is derived from the brightness, $b$, measured by the camera pixels (using the thin-chord approximation). The brightness is

$$b = \frac{1}{4\pi} \int \varepsilon(s)\, ds, \tag{4.9}$$

where $s$ is the distance along camera pixel view. To solve for the emission profile, Eq. (4.9) is discretized into the following form,

$$b_i = \frac{1}{4\pi}\varepsilon_j \Delta s_{ij}, \tag{4.10}$$

where the index $i$ represents the quantity for the $i^{\text{th}}$ camera pixel, and $\Delta s_{ij}$ is the chordal length through $\epsilon_j$ for chord $i$, and the repeated subscript implies a sum. Of the possible 307,200 pixels chords only $\sim$ 4000 are used to obtain the emissivity profiles of $\sim$ 2000 grid elements. In these cases less than 200 chords pass through any given emission grid element. This gives sufficient coverage of each emission grid element while allowing the matrix $\Delta s_{ij}$ to be sparse enough that Eq. (4.10) can be solved, in a least squares sense, using the conjugate-gradient method [47].

Using this model and conjugate-gradient method for solving the problem, the emissivities are readily generated. The conjugate-gradient method used in solving the linear equations is similar to that described in Sec. 2.2 with the exception that the procedure used solves a "damped least-squares" problem [47]. A "damped least-squares" problem actually minimizes

$$\left\| \begin{bmatrix} A \\ \lambda I \end{bmatrix} x - \begin{bmatrix} b \\ 0 \end{bmatrix} \right\|_2, \tag{4.11}$$

where $A$ is the geometry matrix in meters, $b$ is the vector of the brightness measurements in arbitrary brightness units (BU), $x$ is the emission profile values in BU/m, $I$ is the identity matrix, and $\lambda$ is a real scalar that represents the damping term also in meters. This regularizes ill-conditioned problems, and has a similar effect to truncating the singular values when generating an inverted matrix from singular value decomposition. The benefits of the conjugate-gradient method over other methods for solving the linear equation has been discussed in Sec. 2.2.

In an effort to test the reconstruction algorithm and determine the error in the reconstructed profiles, test emission patterns were used to generate brightness profiles, using the geometry matrix. These brightness profiles were then used by the recon-

struction algorithm and the resulting emission profile was compared to the original test emission pattern. Several of these tests were done,

1. "checkerboard" test emission pattern and no noise on the generated brightness profile,

2. "checkerboard" test emission pattern and a noise level typical of the imaging cameras on the generated brightness profile, and

3. a mock-up of a typical divertor emission profile and the noise level typical of the imaging cameras on the generated brightness profile.

The most difficult emission pattern to reconstruct is a "checkerboard" emission pattern. In this pattern emission grid elements alternate between a finite value of emissivity and zero emissivity. Figure 4-9 shows the "checkerboard" emission test pattern used to estimate the error generated by the reconstruction algorithm. This emission pattern is difficult because it represents a emission field with the finest scale structure the algorithm could possibly reconstruct. Therefore, if the algorithm can reconstruct the "checkerboard" emission pattern, one can be confident that it can reconstruct most emission patterns.

For test # 1 the "checkerboard" emission pattern is used to generate a brightness profile by matrix multiplying it with the geometry matrix (the same geometry matrix that the reconstruction algorithm uses). In the absence of any noise added to the generated brightness profile, one would expect that the reconstruction algorithm will reproduce the original emission pattern to within the computer machine accuracy ($\epsilon = 10^{-6}$). Figure 4-10 shows a plot of the absolute value of the difference between the initial specified emission and the reconstructed emission. As can be seen in this figure the reconstruction algorithm did not perform in this way. There are two regions where the reconstruction algorithm failed, deep in the divertor slot and along the top of the reconstruction region. The failure in the divertor slot can be explained by the lack of adequate unique views in this region. Most of the viewing chords that record information from this region are parallel and can not distinguish the fine structure of

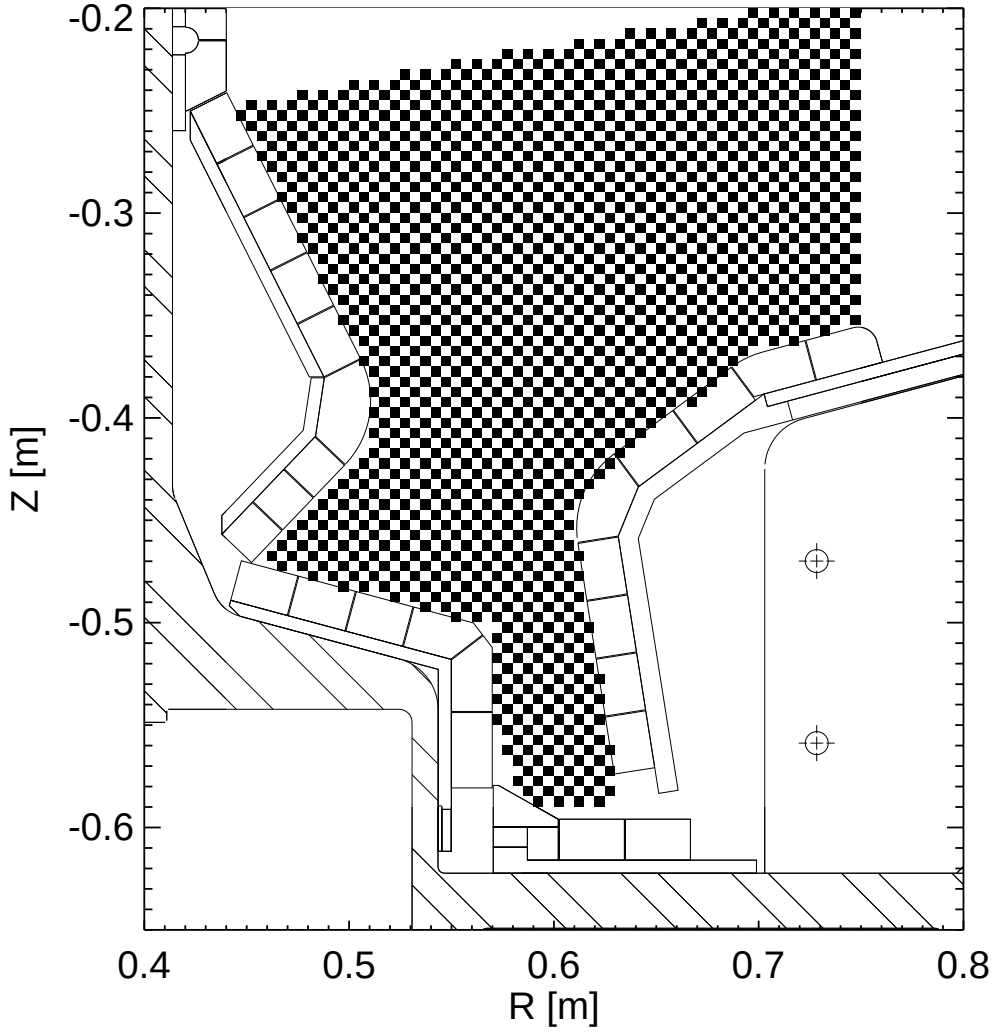


Figure 4-9: The "checkerboard" emission test pattern used to estimate the error generated by the reconstruction algorithm.

emission from this area. The region along the top of the reconstruction area is also poorly covered by different viewing chords. This region is viewed mostly by chords from the edge of the camera view and therefore only a few chords pass through this region, limiting the ability of the reconstruction algorithm to properly recreate the emission along this area. This result represents the best the reconstruction algorithm can do. Therefore, when noise is added to the brightness data there is no expectation that the reconstruction algorithm can accurately reproduce the emission profile from these areas.

The next test was to add noise to the brightness data. To simulate accurately the data from the camera, the camera's inherent noise level was measured. This was done by averaging the value of each pixel over 150 frames and subtracting this average from each pixel in all of the frames. This removes the pixel to pixel variation in the CCD chip. A histogram of this difference over the entire CCD chip is then plotted. This histogram, see figure 4-11, was then fit to a Gaussian distribution and its FWHM is a measure of the noise on the brightness measurement. The FWHM for the camera system used was found to be 15.3 in pixel value (which is an integer from 0 to 255) and was found not to vary as a function of the brightness of the incident light. This constant noise level is attributed to the electrical noise inherent in the system.

With the noise from the camera known, the test of the reconstruction of the "checkerboard" emission pattern with noise on the brightness signal was done. This test used the same geometry matrix and the initial calculation of the brightness as in test # 1. The noise was added by using a normal distribution random number generator with a width in the distribution of 6% ($\approx$ 15.3/255) of the maximum value of the initial brightness calculations. When there is an error on the brightness measurement, the reconstruction routine requires the use of the damping parameter to obtain realistic solutions. A scan was done to obtain the damping parameter that yielded a solution closest to the "checkerboard" emission profile. It was determined that a damping parameter of 0.01 m was an adequate value, although a 50% variation (0.005-0.015 m) provided results that were not significantly different from the 0.01 m case. Figure 4-12 shows a plot of the absolute value of the difference between the

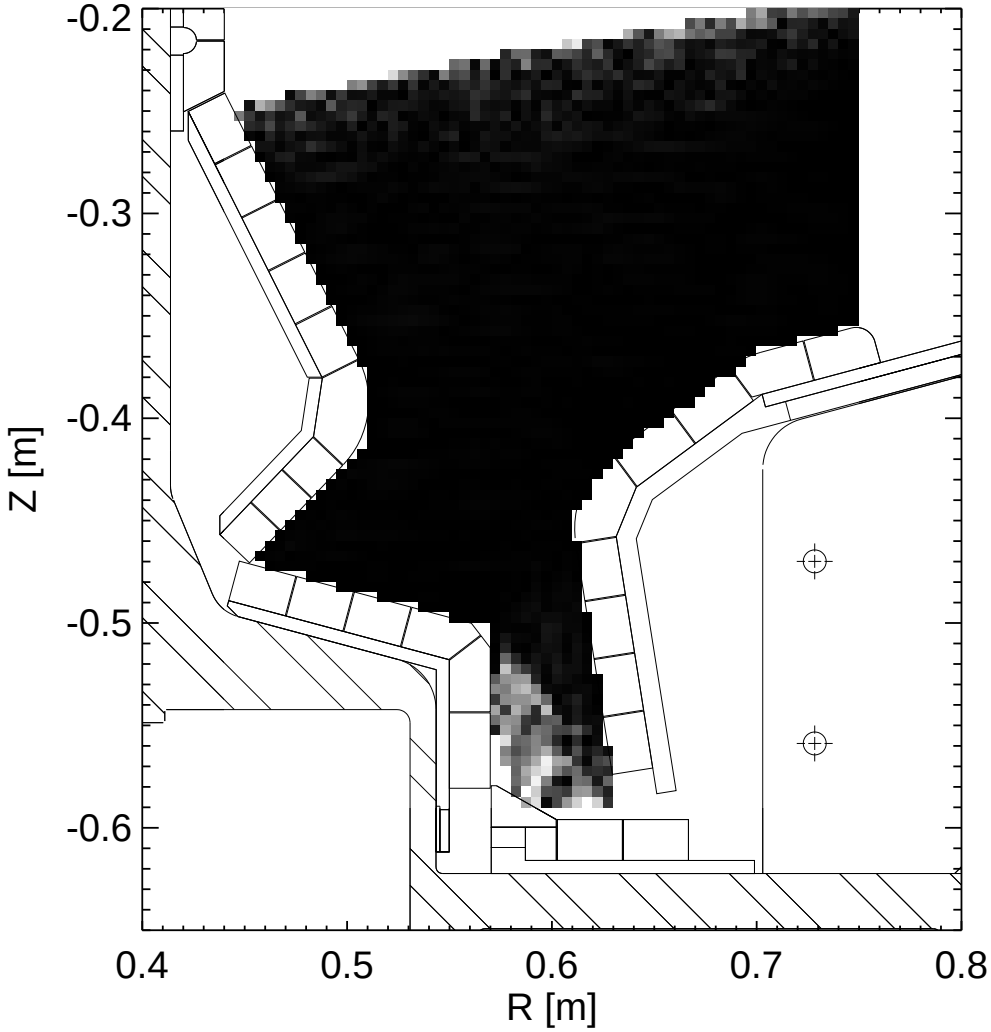


Figure 4-10: Plot of the absolute value of the difference between the initial specified emission and the reconstructed emission profile. The scale is a linear gray scale with white elements representing a difference between the original emission and the reconstructed emission of 0.9 BU/m and black representing a difference of 0.0 BU/m. The maximum value of the initial emission profile was 1 BU/m.

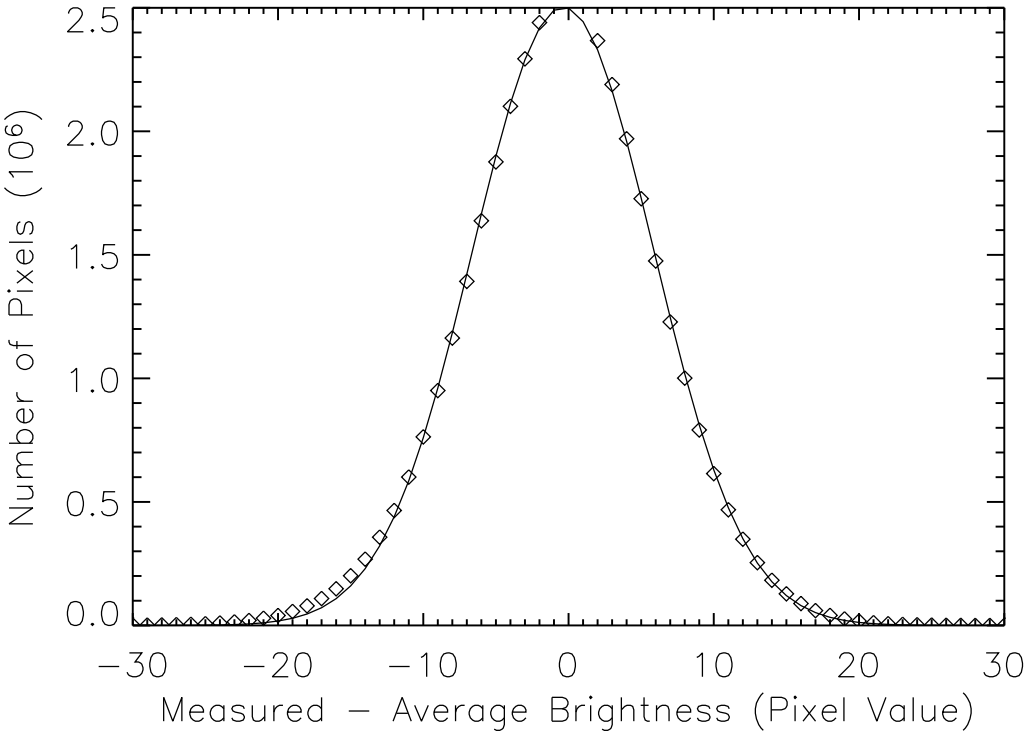


Figure 4-11: A plot of the histogram of the difference between the measured pixel value and the average pixel value for each pixel from the entire CCD chip over 150 frames, when viewing a constant brightness source.

initial specified emission and the reconstructed emission. In this plot the scale is linear with white representing a difference of 1 BU/m or more (up to 10 BU/m) and black representing no difference. The maximum value of the initial emission is 1.0 BU/m and the average absolute difference between the two emission profiles was 110% the maximum original value. Therefore, with the measured inherent statistical error on the brightness measurements, the reconstruction algorithm cannot adequately resolve the "checkerboard" emission profile.

In the previous tests the test emission profile used was the most difficult for the reconstruction algorithm to solve for. Therefore, in the final test a more typical (but still artificial) emission profile was used as the test emission. Figure 4-13 shows the test emission used in this test. Using this emission profile to generate the brightness measurements, and keeping the noise on those brightness measurements and the damping parameter the same, yields an average difference between the test emission pattern and the reconstructed emission pattern of 0.1 BU/m, where the peak of the emission has a value of 1 BU/m. Figure 4-14 shows the reconstruction of the "typical" emission using the same noise level and damping parameter as that used in the "checkerboard" tests. Although the average error found in this test is significantly better than that for "checkerboard" case with noise added, the error was substantially improved by choosing a different damping parameter. The solution with the lowest average error (0.02 BU/m) occurred when the damping parameter was set to 0.15 m. Figure 4-15 shows the reconstruction of the "typical" emission profile using a damping parameter value of 0.15 m. Since increasing the damping term has a similar effect on the reconstruction that truncating the singular values in SVD does, i.e., smoothing the reconstruction, the best value for the damping parameter depends on the size of the emission features. This implies that small scale features of the emission profiles from the divertor are not accurately reconstructed, but the larger features are reconstructed accurately.

The optimized reconstruction technique described above generates two-dimensional profiles consistent with the visible spectrometer viewing the divertor. The reconstruction method was applied to a calibrated image of $D_\gamma$ brightness recorded by one of

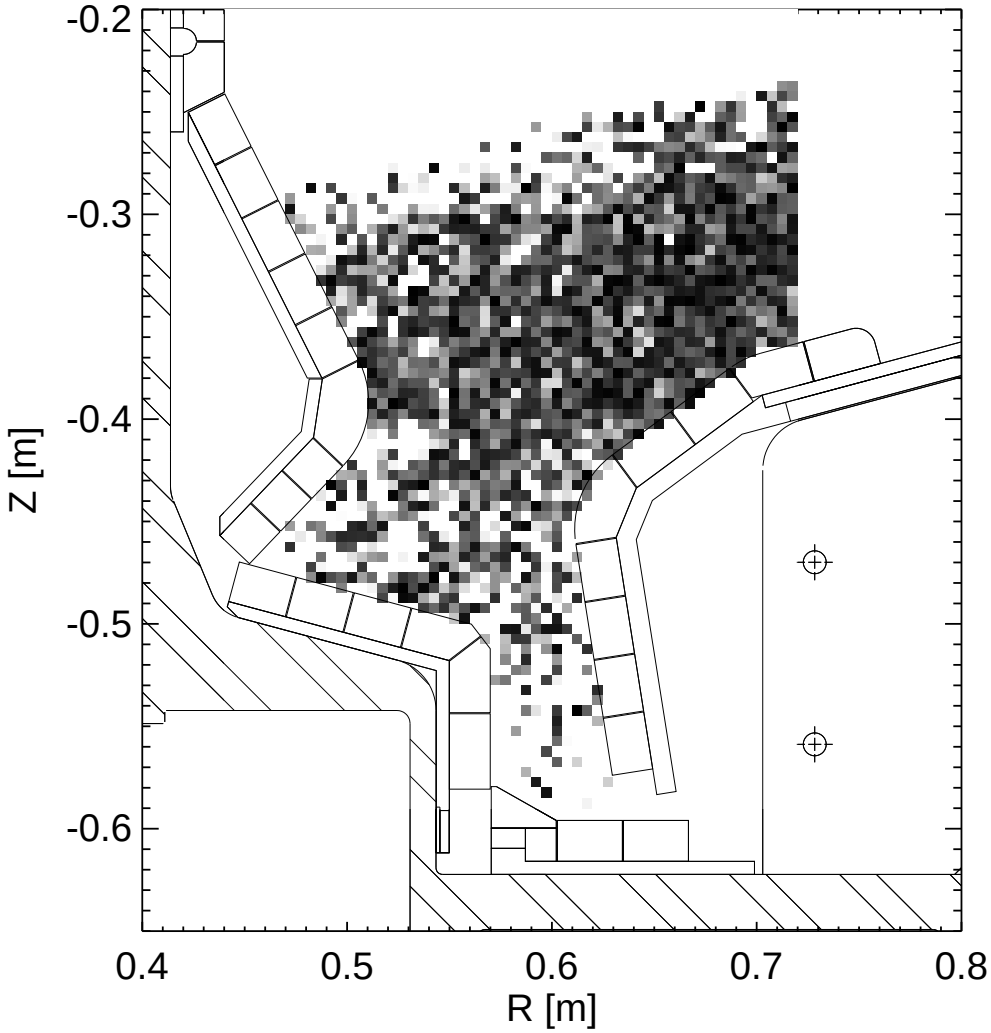


Figure 4-12: Plot of the absolute value of the difference between the initial specified emission and the reconstructed emission, when the brightness has a normal distributed noise with a FWHM of 6% of the maximum brightness and a damping parameter of 0.01 m. In this plot the scale is linear with white representing a difference of 1 BU/m or more and black representing no difference.

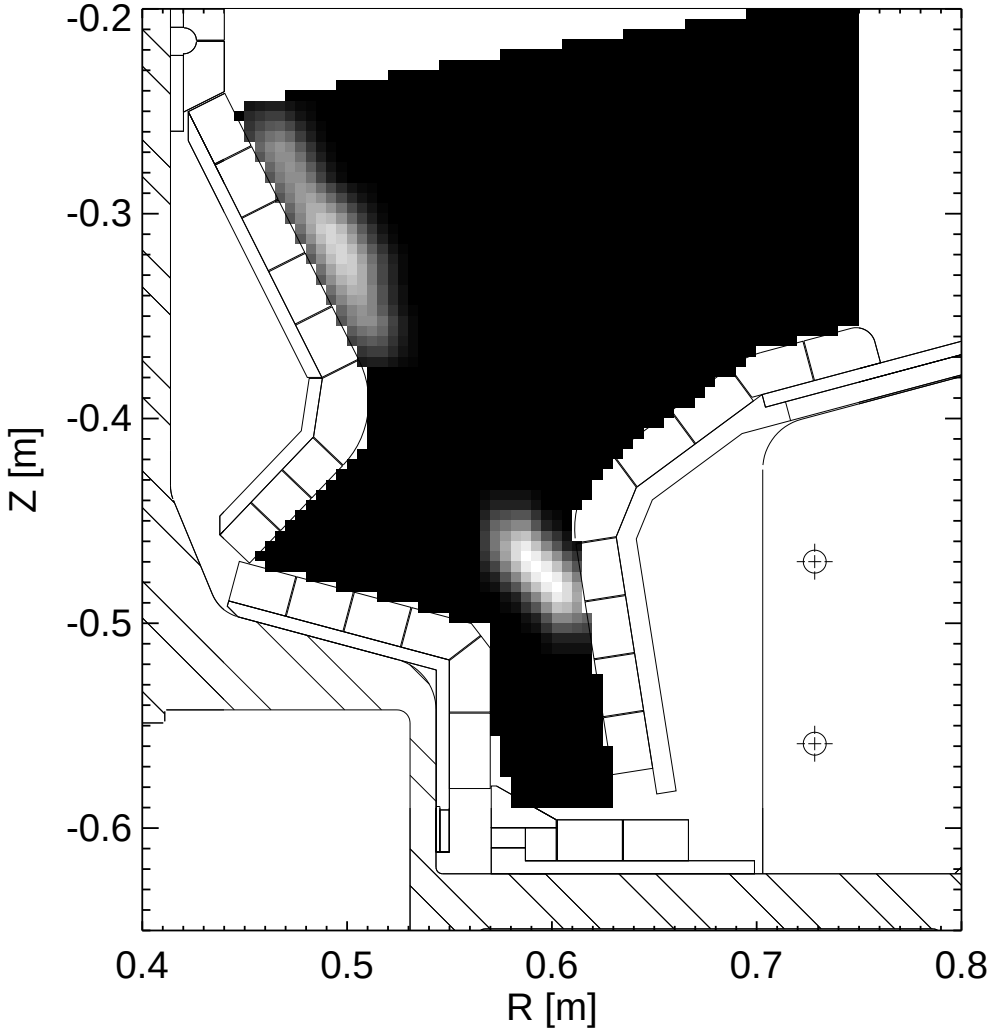


Figure 4-13: Plot of the emission profile used in the third test of the reconstruction algorithm. This profile is more typical of those seen in the divertor of Alcator C-Mod. This plot uses a linear gray scale with the maximum value being 1 BU/m and minimum being 0 BU/m.

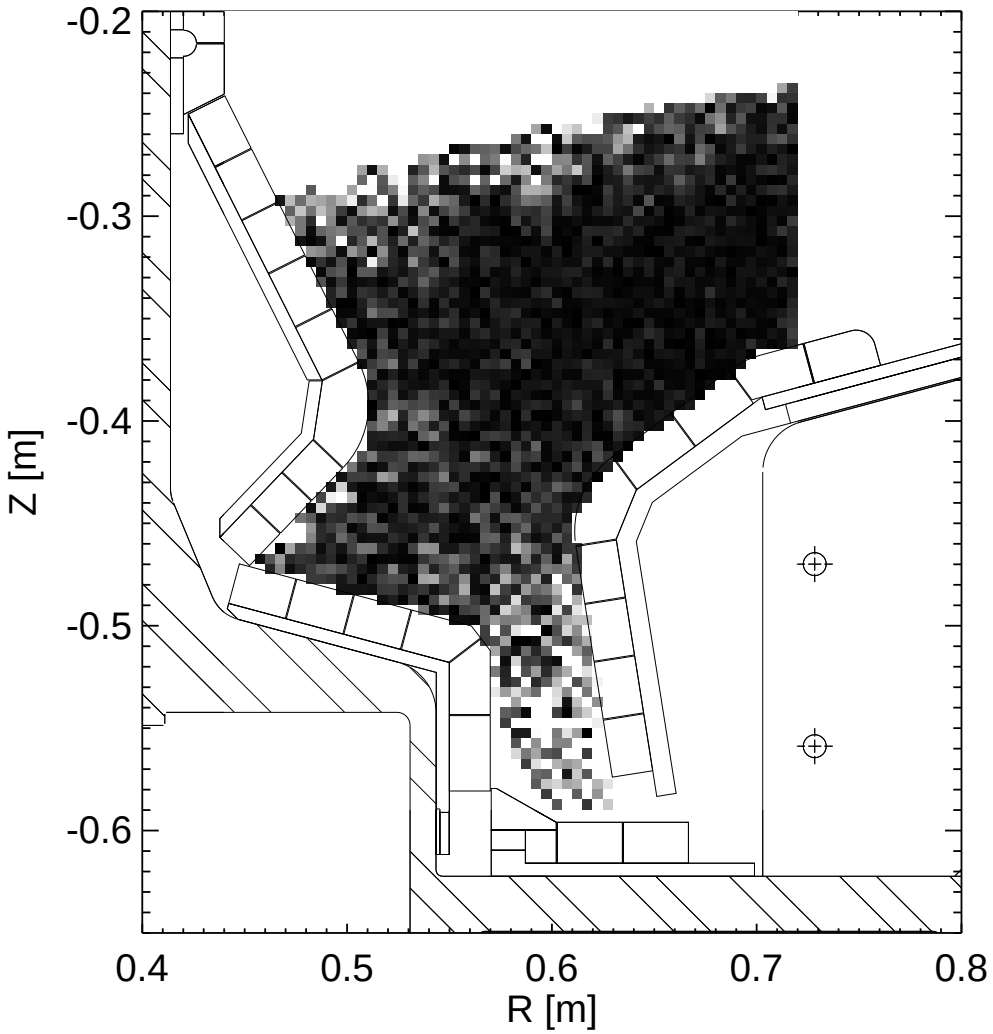


Figure 4-14: Plot of the absolute value of the difference between the initial specified emission used in the third test of the reconstruction algorithm and the reconstructed emission, when the brightness has a normal distributed noise with a width of 6% of the maximum brightness and a damping parameter from the "checkerboard" tests. This plot uses a linear gray scale with the white cells representing a difference of 1 BU/m and above and the black cells representing a difference of 0 BU/m.

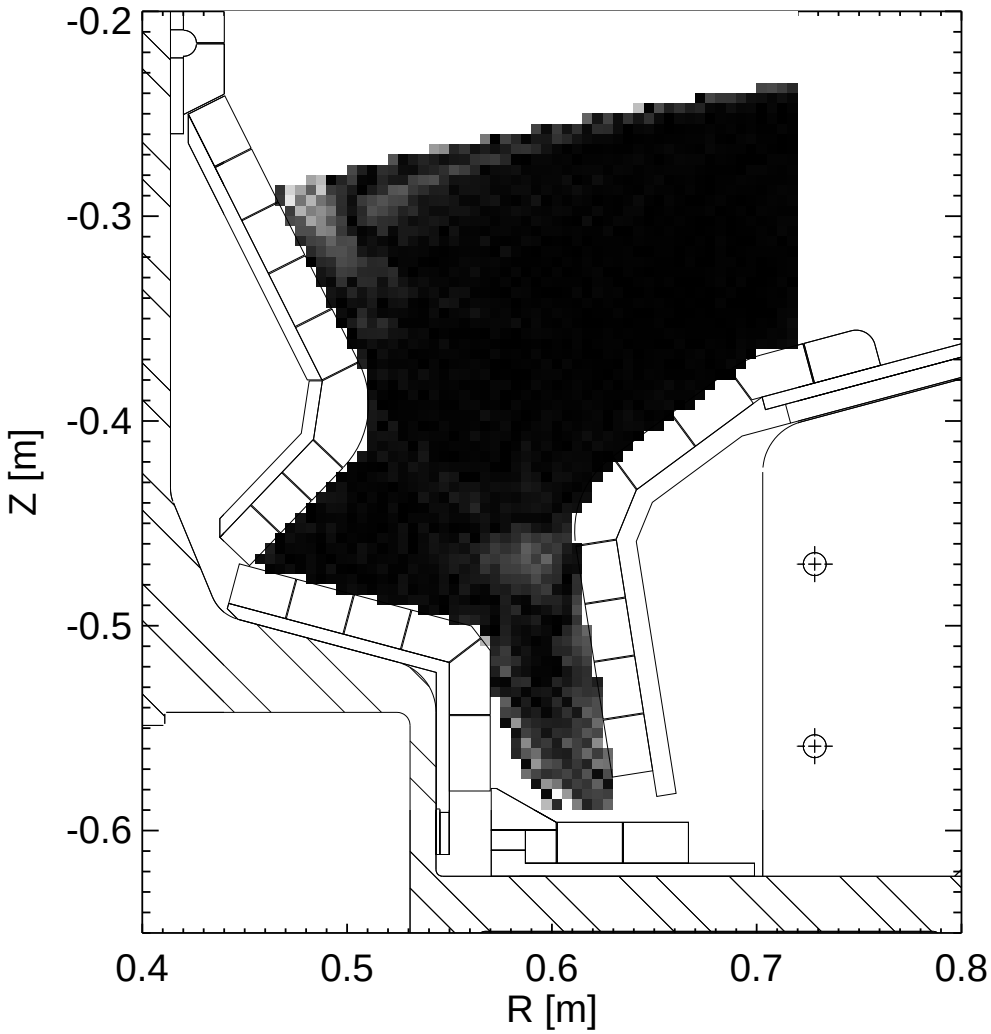


Figure 4-15: Plot of the absolute value of the difference between the initial specified emission used in the third test of the reconstruction algorithm and the reconstructed emission, when the brightness has a normal distributed noise with a width of 6% of the maximum brightness and a damping parameter of 0.15 m. This plot uses a linear gray scale with the white cells representing a difference of 1 BU/m and above and the black cells representing a difference of 0 BU/m.

the divertor viewing cameras. In this and all emission reconstructions following the damping parameter value was 0.15 m. Figure 4-16 shows the raw brightness image and reconstructed emission profile for a moderate density ($\bar{n}_e = 1.5 \times 10^{20}$ m$^{-3}$), Ohmic L-mode discharge. To validate the reconstructed emission, $D_\gamma$ measurements from a visible spectrometer viewing the the divertor region were compared to the value predicted by the reconstructed emission. Figure 4-17 shows the views of the divertor from visible spectrometer. Figure 4-18 shows the comparison between the measured values obtained from the visible spectrometer and the predicted values from the reconstructed emission. As figure 4-18 shows the measurements and the predicted values agree to within the experimental error of both diagnostics.

## 4.3 Physics Problems Addressed

### 4.3.1 Divertor Recombination Profiles

One method of controlling the interaction of the hot core region of the tokamak plasma with the vacuum vessel is by placing a physical limiter into the plasma some distance away from the vacuum vessel wall. This is an effective method of controlling the interactions, but it does have its drawbacks. The main problem with using a limiter to define the core plasma is the close proximity of material surfaces to the hot plasma core. When the hot plasma ions strikes the plasma-facing-components (PFC) of the limiter, material will be sputtered and quickly arrive in the core plasma, both diluting the main species and increasing the radiation from this region. A solution to the problems that the limiter generates is the use of a separatrix and divertor. A separatrix magnetically defines the hot core plasma, and directs plasma that comes from the core to a material surface (the divertor plates) away from the core. Any impurities sputtered have to travel through the plasma outside the separatrix to reach the core where they can be ionized and flow back to the divertor plates.

Future tokamak designs rely on the use of a divertor to control impurity production and contamination, enhance particle pumping, and control power deposition on

(a)

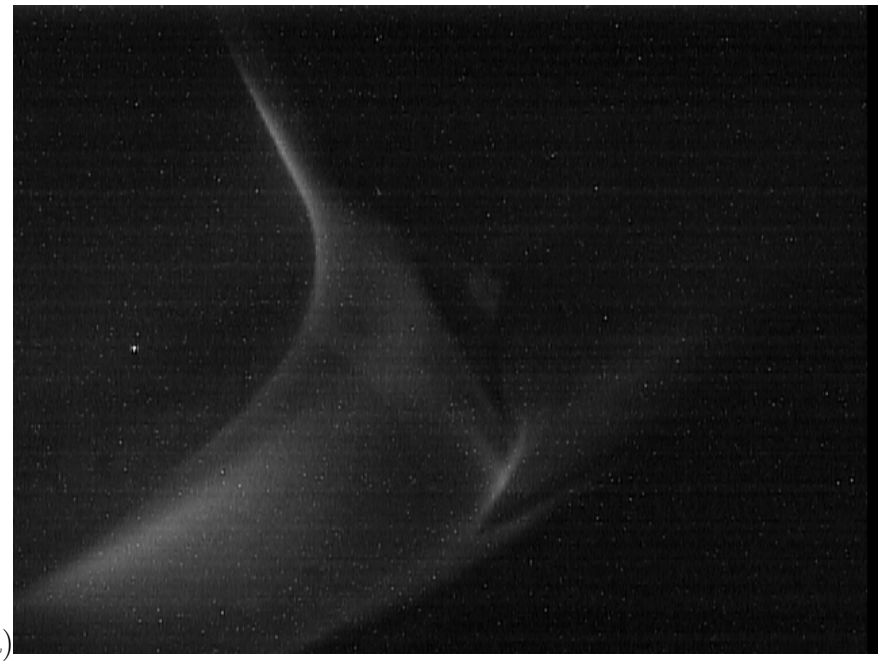

(b)

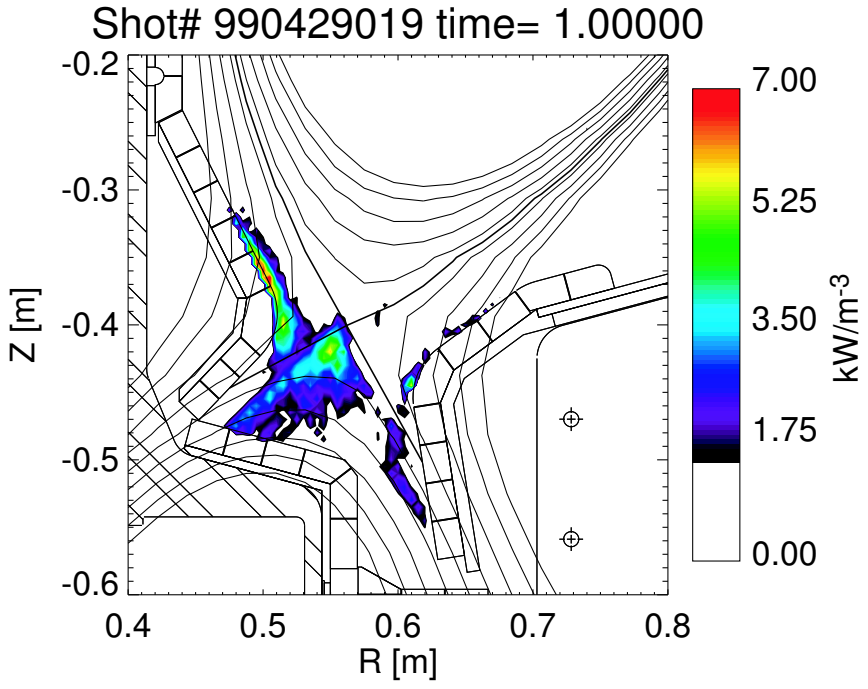


Figure 4-16: (a) The raw brightness image of $D_\gamma$ emission and (b) the reconstructed emission profile for a moderate density ($\bar{n}_e = 1.5 \times 10^{20}$ m$^{-3}$), Ohmic L-mode discharge.

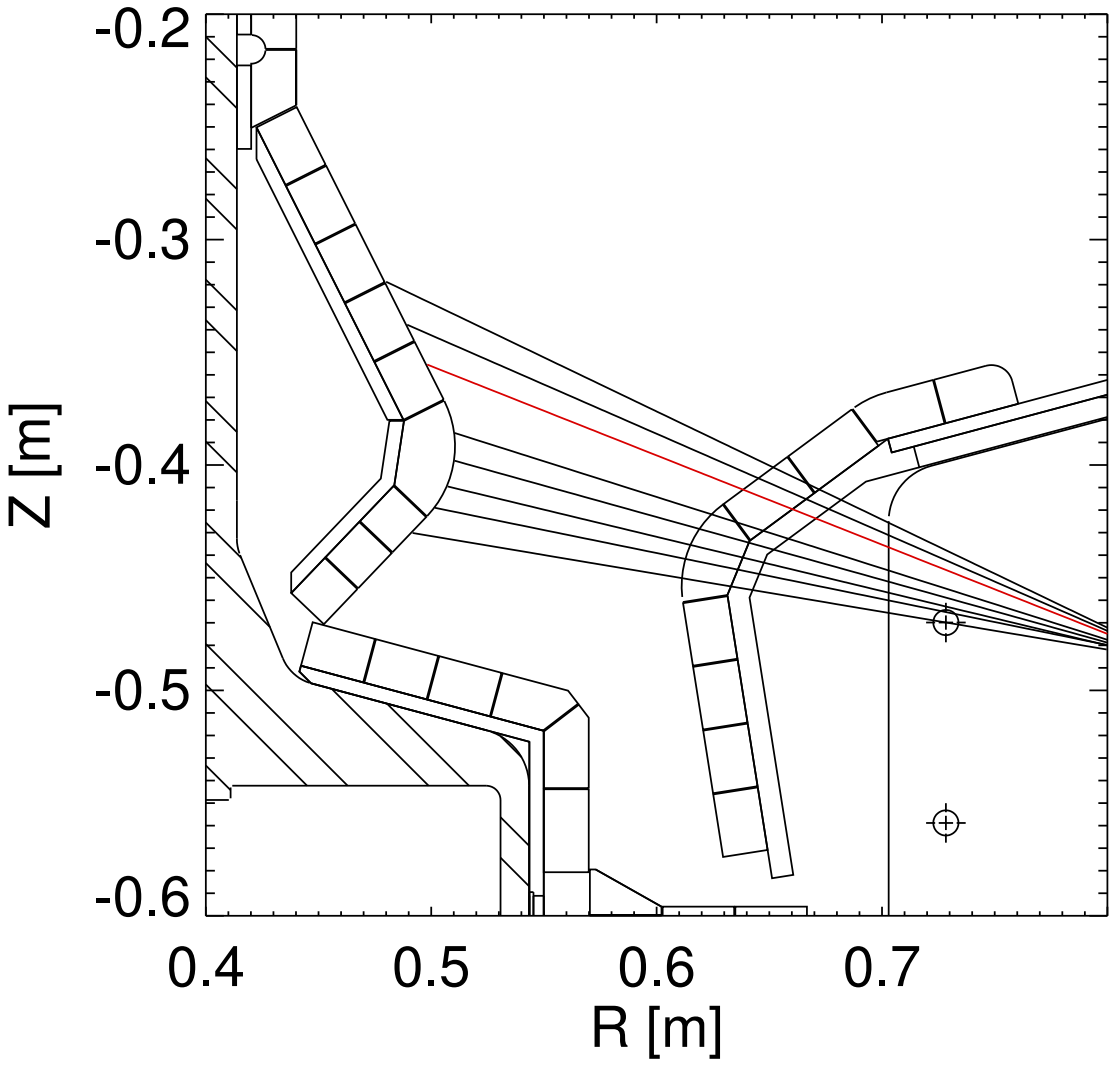


Figure 4-17: The views from the visible spectrometer. The red chord is the chord used in figure 4-18.

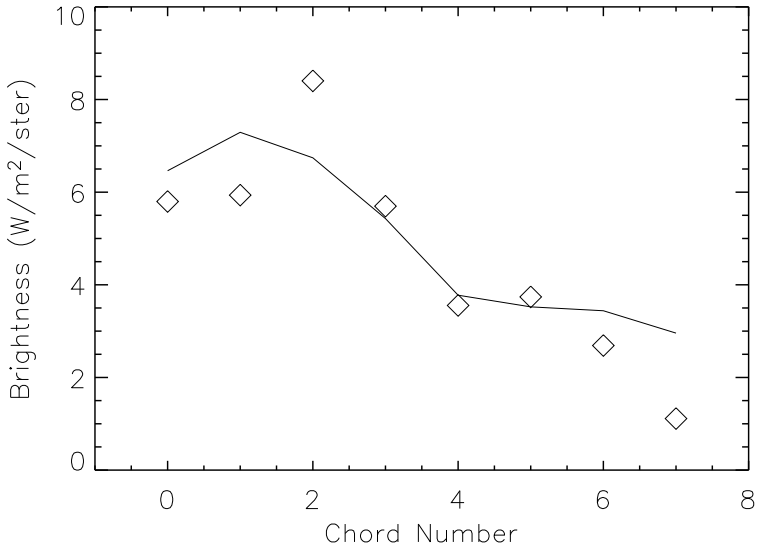


(a)

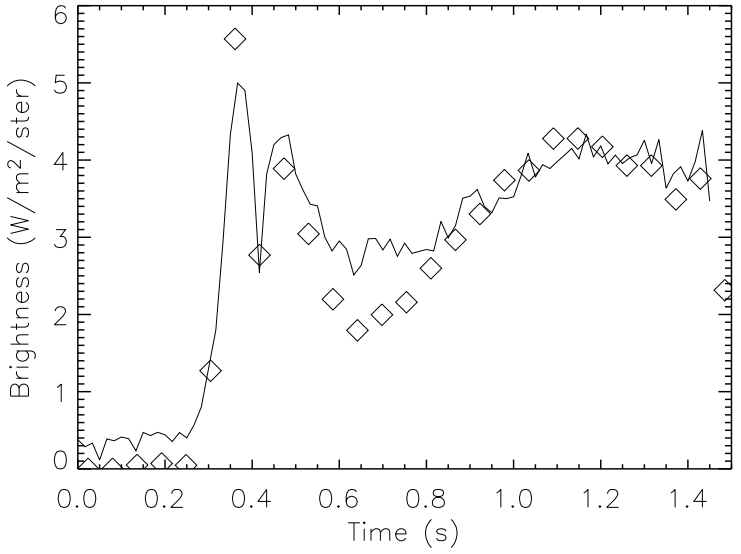


(b)

Figure 4-18: Comparison between the measured values obtained from the visible spectrometer (⋄) and the predicted values from the reconstructed emission (-). (a) shows the comparison between the measured and predicted values for all chords shown in figure 4-17 at one time and (b) shows the comparison for the chord in red from figure 4-17 as a function of time.

the plasma-facing-components. Two major tokamak designs (ITER-FEAT [2] and FIRE [6]) for the "next step" burning plasma experiments have divertors as a main component in the design. In these cases the peak heat flux is expected to be $\leq 10$ MW $m^{-2}$ for the ITER-FEAT [29] case and $\sim 25$ MW $m^{-2}$ for the FIRE [6] case. The particle pumping required for these designs is $10^{23}$ particles/sec and $10^{21}$ particles/sec respectively. This is a higher heat flux than most materials can handle in a passively cooled steady-state situation. The pumping rate is also high enough that, for the pumping rate to be achieved feasibly, a compression of the neutral gas in the chamber near the pumping system must be accomplished.

A solution to both the problems of power deposition and particle control is a dissipative divertor, of which there are two types — a radiative divertor and a detached divertor. In a radiative divertor a significant portion of the power is radiated away before the plasma particles strike the divertor plates. By radiating the power, the power deposition is distributed over the entire divertor region therefore reducing the peak heat flux on the material surfaces. The other solution, a detached divertor, reduces both the power and the particle fluxes on the divertor plates. The power is primarily dissipated by radiation until plasma-neutral friction forces and/or plasma volumetric recombination reduce the local particle flux.

Volumetric recombination is an important element in solving the divertor problem by reducing the plasma particle flux to the divertor plates. Volumetric recombination is a signature of the so-called deeply detached divertor and can be a major contributor to the reduction of particle flux (up to half of the entire plasma particle flux to the divertor region). The two-dimensional evolution and spatial distribution of the volumetric recombination regions yield insights into the mechanism of divertor detachment and the flows of plasma in the divertor.

### Experimental Technique

Two-dimensional emission profiles of $D_\gamma$ in the divertor are generated using the same technique as described in Sec. 4.2. The reconstructions use a thin-chord approximation and assume toroidal symmetry. They are also absolutely calibrated and checked

using the chordal $D_\gamma$ measurements from the visible spectrometer.

Electron temperature and density measurements in the divertor region are obtained by analysis of data taken by flush-mounted Langmuir probes and a visible spectrometer. The flush-mounted Langmuir probes are mounted on the outer and inner divertor plates [34] having the locations shown in Fig. 4-19 by green triangles. The visible spectrometer has multiple views of the divertor shown in Fig. 4-19. The visible spectrometer may be used to determine the electron temperature and density of the plasma in the region of maximum deuterium emission along each line-of-sight. The electron density is determined by measuring the Stark broadening of the $p = 6, 7, 8 \rightarrow 2$ deuterium lines where $p$ is the principal quantum. [18] The electron temperature is determined by using the knowledge that the population densities of deuterium atoms with energy levels greater than $p = 5$ are in Saha equilibrium and therefore have the temperature dependent distribution of

$$n_p \propto \frac{p^2}{T_e^{3/2}} \exp\left(\frac{13.6}{T_e p^2}\right), \tag{4.12}$$

where $n_p$ is the population density of electrons in level $p$ and $T_e$ is the electron temperature in eV.[39]

While the Langmuir probes provide a local electron temperature and density measurements, the visible spectrometer's data is line integrated and is localized by using the 2D $D_\gamma$ divertor emission profiles. As long as the electron temperature in the line-of-sight is above $\sim$0.33 eV the emission from the $p = 6, 7, 8 \rightarrow 2$ deuterium lines will be approximately proportional to the $D_\gamma$ emission. Therefore, by determining the distribution of the $D_\gamma$ emission along a visible spectrometer chordal view the temperature and density measurements can be localized to the peak of the emission. This implies that there is one temperature and density measurement per visible spectrometer viewing chord.

Using the 13 (one per spectrometer line-of-sight) localized electron temperature and density measurements, and the $D_\gamma$ emission profiles volumetric recombination profiles can be estimated for the divertor. Beginning with the $D_\gamma$ emission profiles,

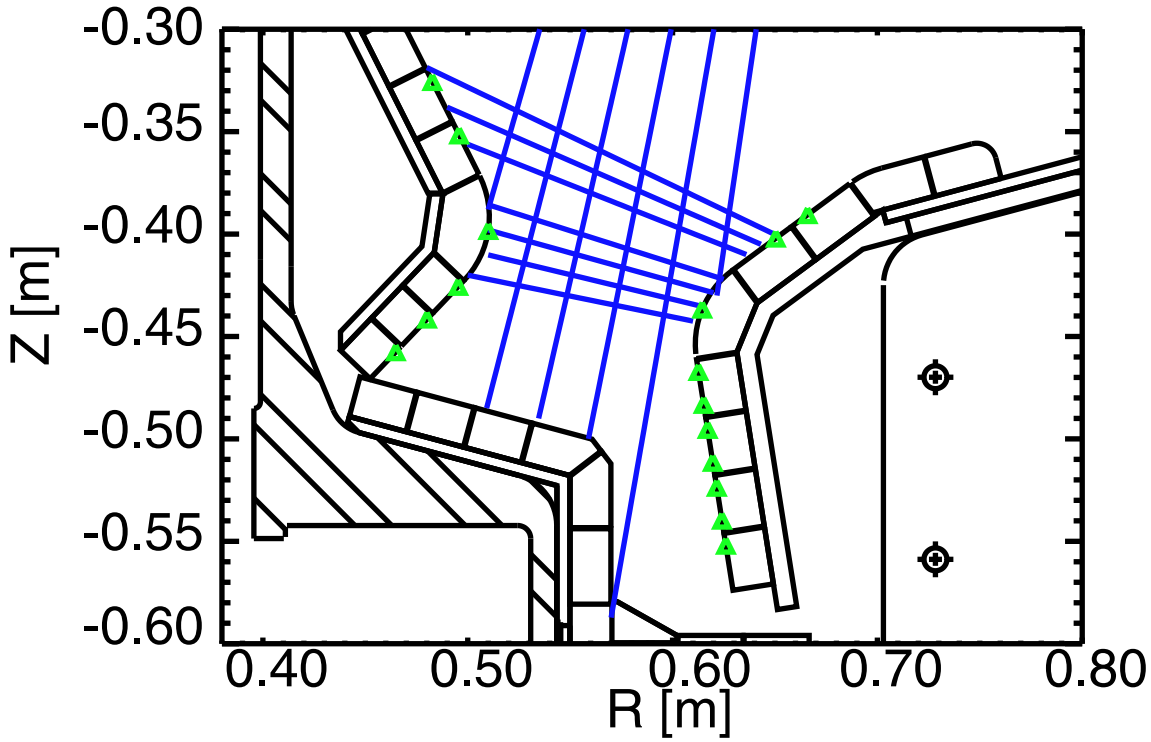


Figure 4-19: The triangles are the locations of the flush-mounted probes and the straight lines are the chordal views of the visible spectrometer.

electron density and temperature values can be assigned to each $D_\gamma$ emission element based on the nearest localized temperature and density measurement. Since there is a $D_\gamma$ emissivity, electron density, and electron temperature measurement associated with each emission element, and since this is a strongly recombining plasma, the $D_\gamma$ photon per recombination curves [42] can be applied directly, yielding the recombination profiles in the divertor. In a strongly recombining plasma, such as the type studied here, the amount of $D_\gamma$ photons caused by excitation, and therefore related to the ionization rate, is less than 1 percent.

**Results**

Using the two-dimensional profiles of recombination rate in the divertor, a comparison can be done of the total recombination rates of the inner divertor, outer divertor and private flux regions. The inner (outer) divertor region in this case is defined as the scrape-off layer region bounded by the inner (outer) leg and extends in the direction of decreasing (increasing) major radius. The private flux region is the area below the x-point and bounded by the inner and outer legs. Figures 4-20, 4-21, and 4-22 show the total recombination rates for these regions as a function of the line-averaged density of the plasma. All other parameters were kept constant in this Ohmic, L-mode discharge, i.e., plasma current ($I_p = 800$kA), toroidal magnetic field ($B_T = 5.4$ T), and magnetic configuration.

When comparing the recombination rates of the three regions two regimes can be identified, one where the outer divertor region is attached and one where outer divertor region is detached. This is most easily delineated in figure 4-22 where the peak of the private flux region's recombination rate is used as a boundary between these regions.

The three regions have clear and different behavior in the two regimes. In the attached regime the inner divertor's recombination rate actually shows little if any trend when the line-averaged density is increased. The outer divertor region also shows a slow increase with density while in the attached regime. The private flux region, on the other hand, shows a substantial increase in its recombination rate as the

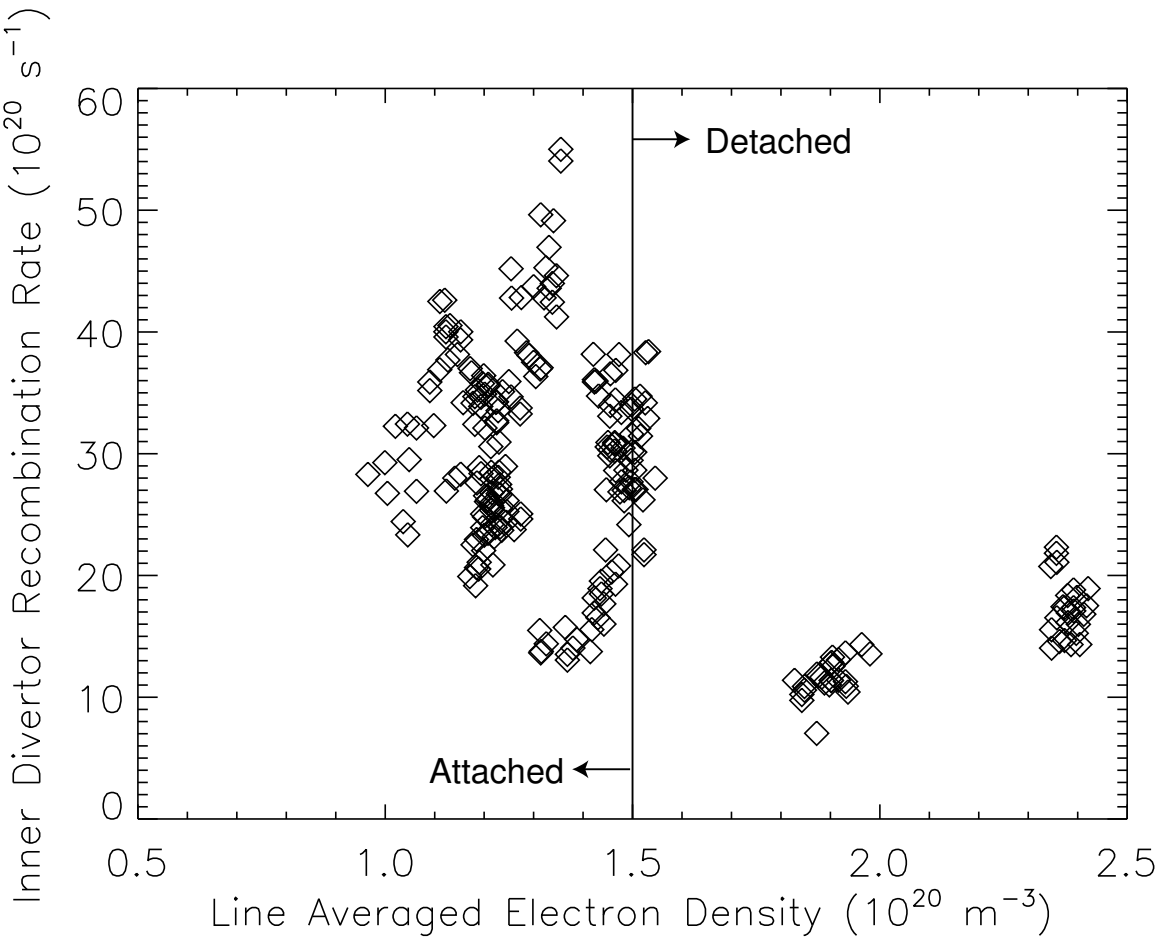


Figure 4-20: Total volumetric recombinations in the inner divertor region as a function of line-averaged density

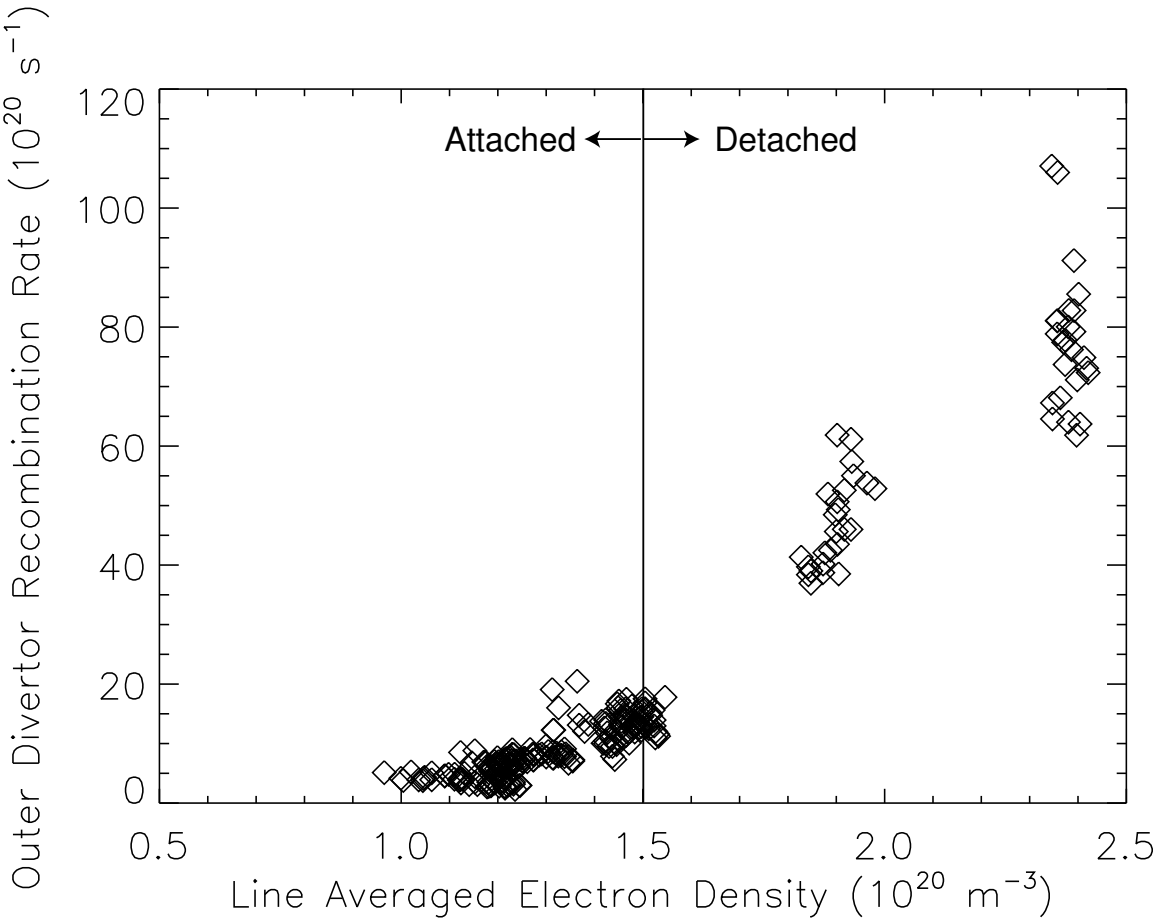


Figure 4-21: Total volumetric recombinations in the outer divertor region as a function of line-averaged density

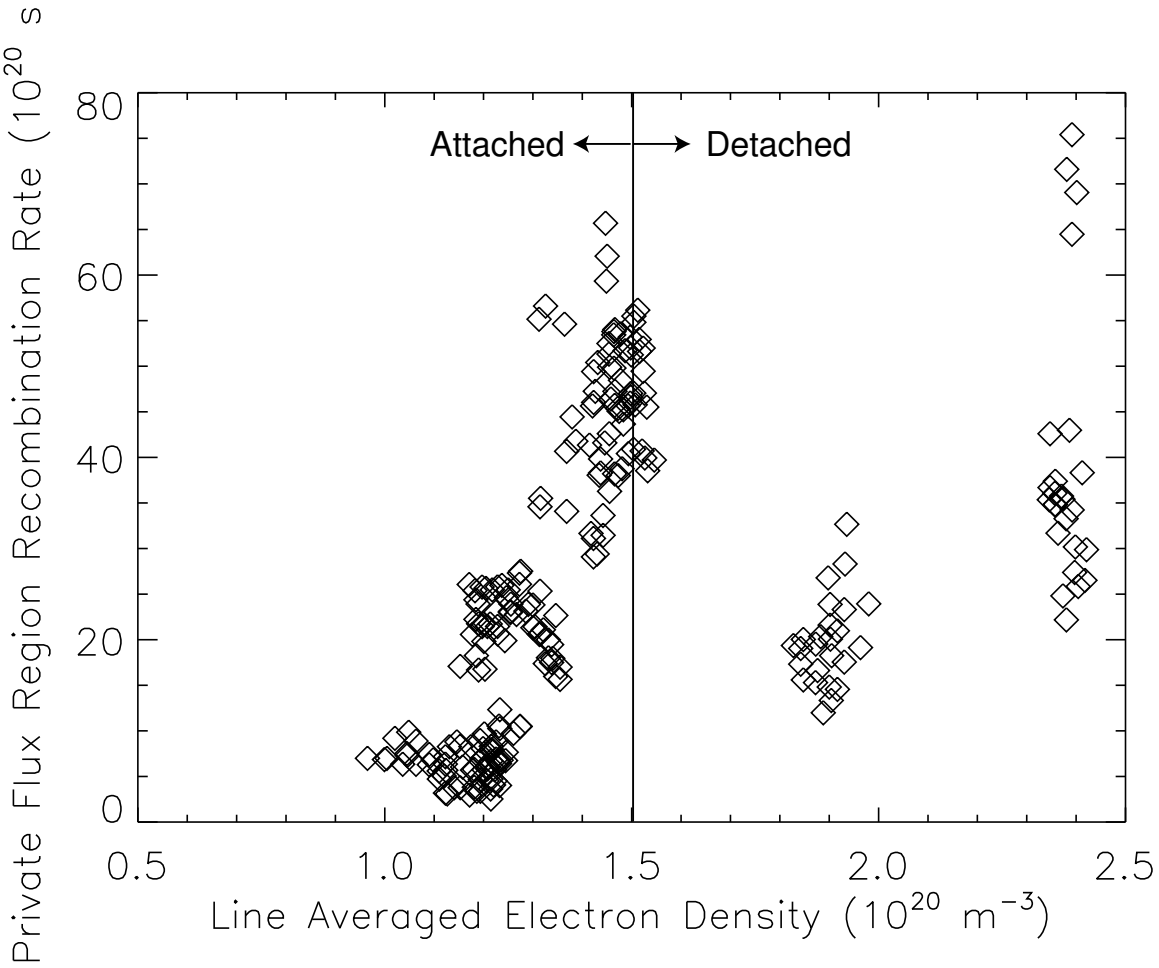


Figure 4-22: Total volumetric recombinations in the private flux region as a function of line-averaged density

line-averaged density is increased in the attached regime. In the detached regime the recombination rate in the inner divertor region still shows little variation although it is generally lower in magnitude. The recombination rate in the outer divertor region in the detached regime increases significantly as the line averaged density is increased. Finally, in the private flux region the recombination rate decreases as the line averaged density increases. The recombination rate measurements in the private flux region for the highest values of the line averaged density are due entirely to the recombinations along the outer leg, but still in the PFZ.

Figures 4-20, 4-21, and 4-22 show the general trend of recombinations in the different divertor regions, but since we have the two-dimensional data a closer inspection of the recombination distribution in the two regimes was also undertaken. Figures 4-23, 4-24, and 4-25 show the $D_\gamma$ profiles (which, in these cases, have similar distributions to the recombination rates) for the attached regime ($\bar{n}_e = 1.2 \times 10^{20}$ m$^{-3}$), at the boundary between the two regimes($\bar{n}_e = 1.5 \times 10^{20}$ m$^{-3}$), and detached regime ($\bar{n}_e = 1.9 \times 10^{20}$ m$^{-3}$). Figure 4-23 clearly shows that nearly all of the recombinations in the divertor are occurring in the inner divertor region in the attached regime. Figure 4-24 shows the typical distribution at the boundary between attached and detached regimes, and it is at this boundary that the largest amount of recombinations is seen in the PFZ. At the boundary of the the two regimes the inner divertor region and the outer divertor region look very similar to the attached divertor regime with the main difference being the private flux region. In the third and detached case, figure 4-25, the recombinations are dominantly occurring in the outer divertor region. In this case, the distribution within the inner divertor region appears similar to the previous cases, while the magnitude has decreased. It should also be noted that the emission in the private flux region near the outer leg is included in the calculation of the total private flux region recombination rate, and leads to the observed increase in the private flux region recombination rate at higher values of line-averaged density, although this should more properly be attributed to the outer divertor region, since the reason for its existence is more properly described by the conditions of the detached outer divertor.

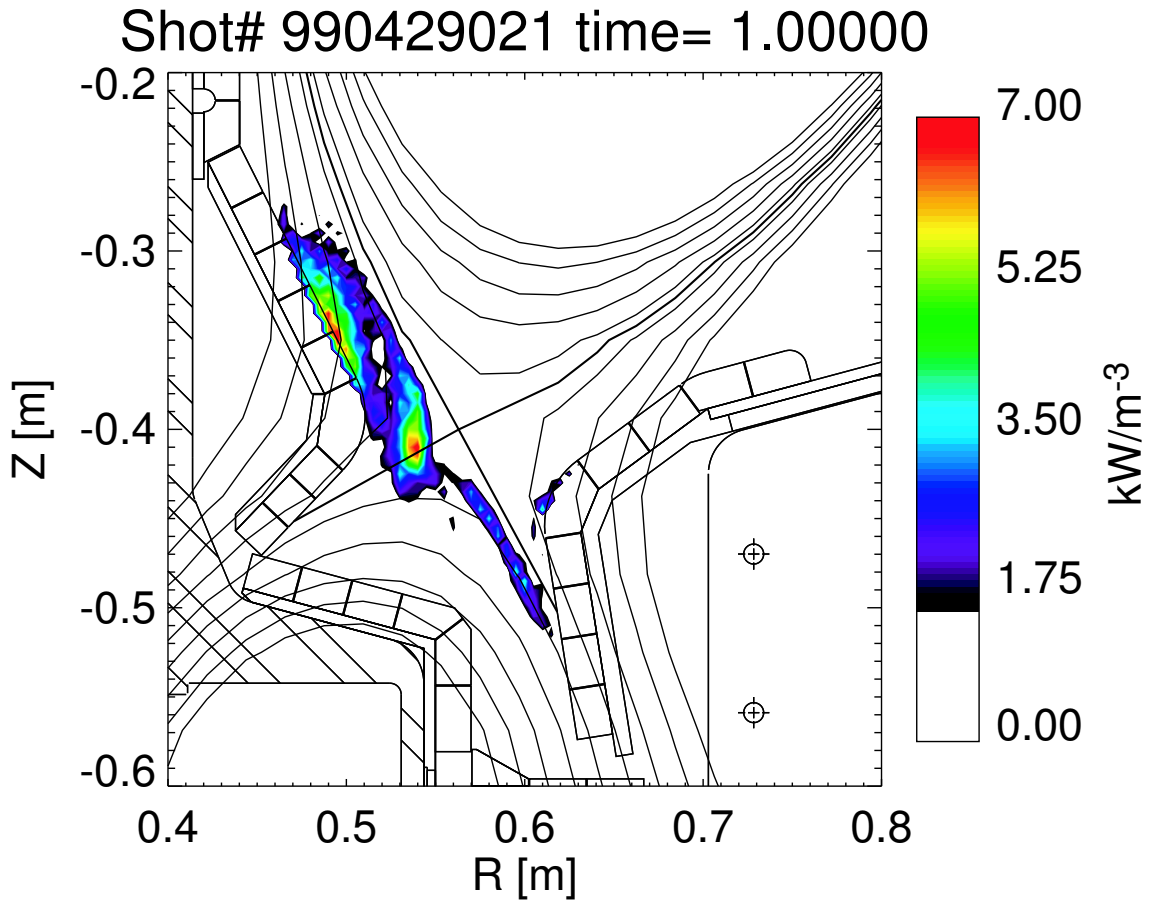


Figure 4-23: The $D_\gamma$ emission profile in the attached regime with a $\bar{n}_e = 1.2 \times 10^{20}$ $m^{-3}$.

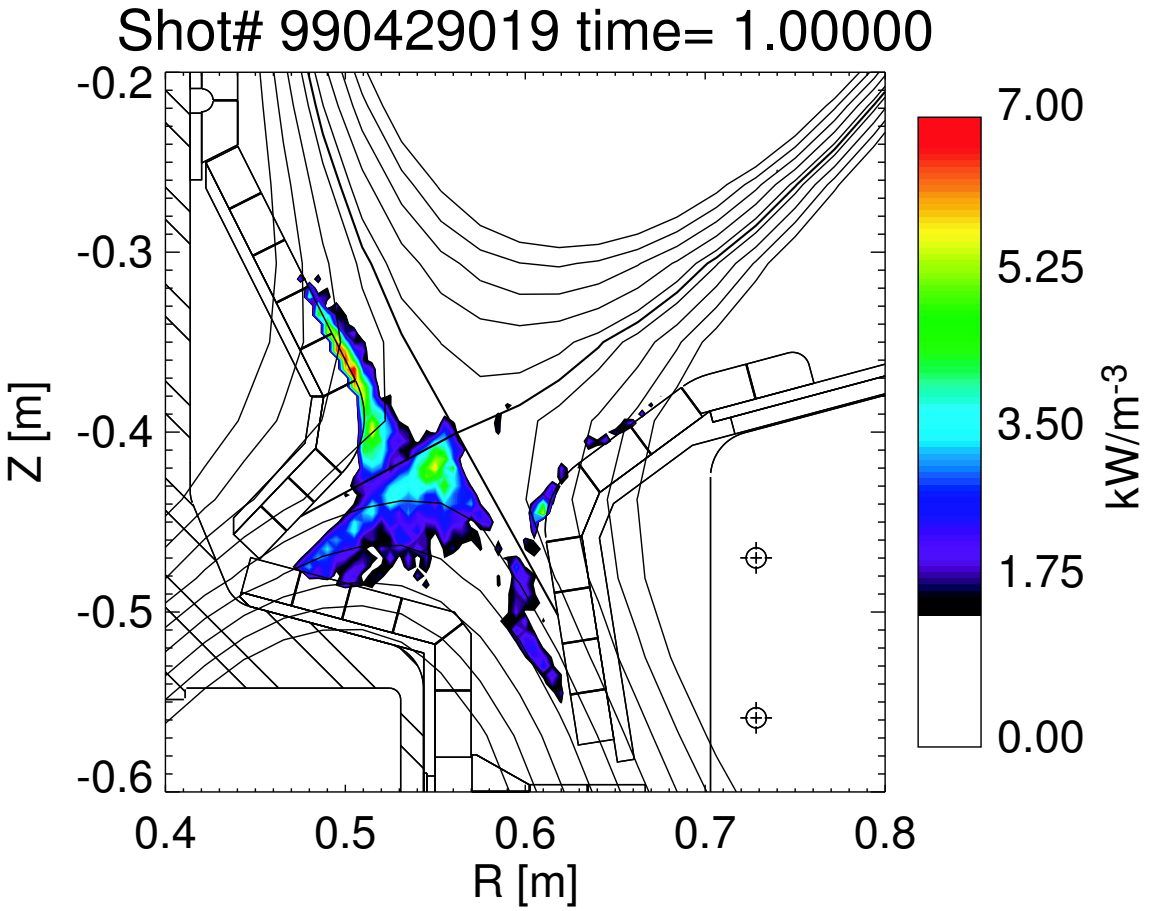


Figure 4-24: The $D_\gamma$ emission profile on the boundary of the attached and detached regime with a $\bar{n}_e = 1.5 \times 10^{20}$ m$^{-3}$.

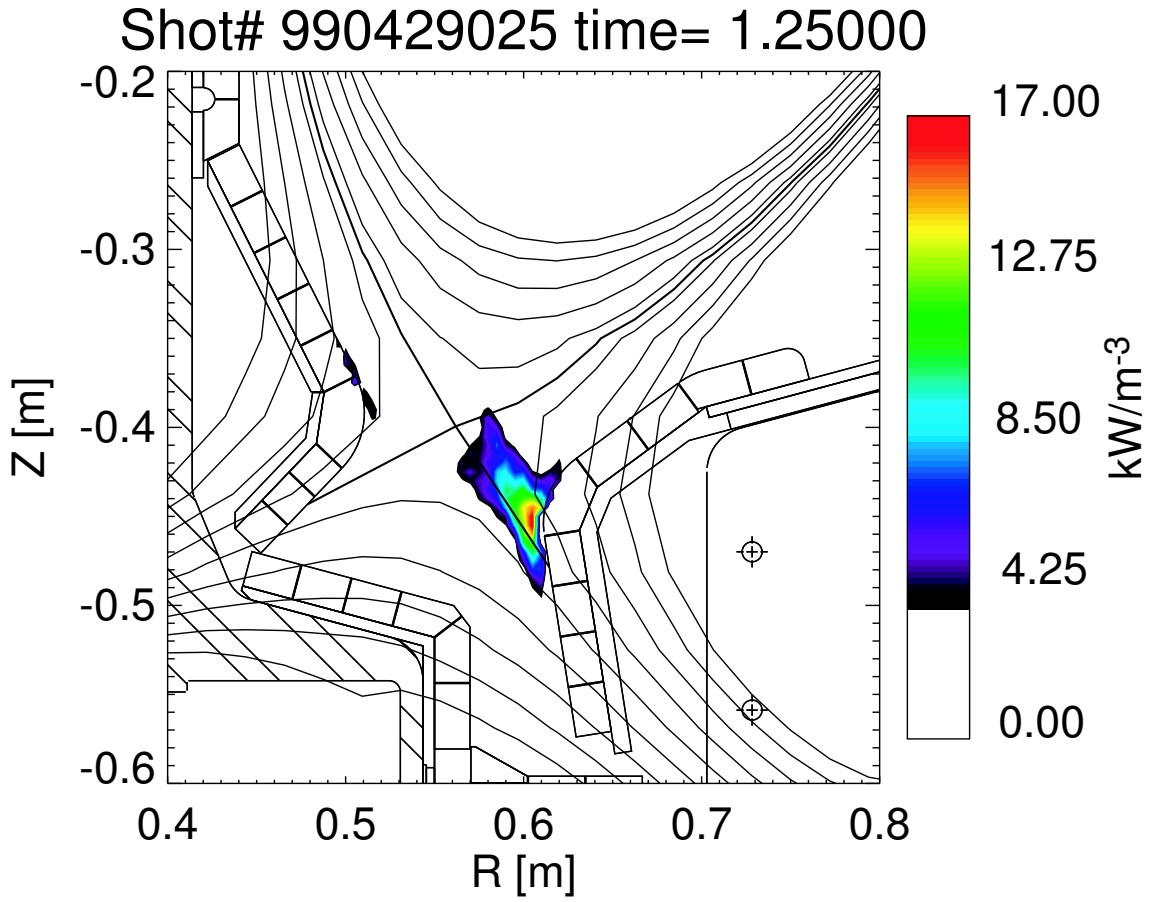


Figure 4-25: The $D_\gamma$ emission profile in the detached regime with a $\bar{n}_e = 1.9 \times 10^{20}$ $m^{-3}$.

### Discussion

By the visible spectrometer measurements ($n_e \approx 10^{21}$ m$^{-3}$, $T_e \leq 1$ eV) there is a significant amount of plasma in the private flux region of the divertor. Therefore the question is how did this plasma get into the private flux region, which can only be accessed by perpendicular diffusion and be driven flows.

There has been only one previously published observation of deuterium emission in the private flux region. [14] The author offered an explanation stating that neutrals enter the private flux region from the inner divertor region and as the discharge progresses to higher density (closer to detachment) the emission from the neutrals fills the private flux region. Then the outer divertor region detaches when the neutral emission from the private flux region begins to enter the outer divertor region. There is one complication to this analysis, all of the observations were taken during an ELMing plasma discharge. In an ELMing discharge it is unknown what the effects of the rapid bursts of power and particles are on the divertor region plasma. Although the observations are similar the plasma discharges studied in this dissertation are all L-mode and therefore have no ELMs to cause the flow into the PFZ.

There have also been other discussions of plasma flows in the scrape-off layer (SOL) and divertor [52, 20, 51] involving a radial $\mathbf{E} \times \mathbf{B}$ drift due to an electron temperature gradient. The discussions of the radial drift were mainly focused on the cause of the in/out asymmetry of the inner and outer divertor electron temperature and density and not the source of the private flux region plasma. Reference [22] specifically discusses the in/out asymmetry on Alcator C-Mod in terms of $\mathbf{E} \times \mathbf{B}$ drifts. The arguments for a radial $\mathbf{E} \times \mathbf{B}$ drift due to a poloidal temperature gradient are the same in this case as in the previously mentioned discussions cited above, and therefore will not be repeated. A brief derivation of the drift from Braginskii's Equations [5] follows.

From the momentum conservation equation

$$m_e n_e \frac{d\vec{v}_e}{dt} = -\nabla \mathsf{P}_e - e n_e \left(\vec{E} + \vec{v}_e \times \vec{B}\right) + \vec{R}. \tag{4.13}$$

By neglecting the electron inertia term ($m_e \to 0$) and assuming a scalar pressure, Eq. (4.13) is reduced to

$$0 = -\nabla p_e - en_e\left(\vec{E} + \vec{v}_e \times \vec{B}\right) + \vec{R}, \tag{4.14}$$

where

$$\vec{R} = -\frac{m_e n_e}{\tau_e}\left(0.51 u_{\|}\hat{\vec{b}} + \vec{u}_{\perp}\right) - 0.71 n_e \hat{\vec{b}} \cdot \nabla T_e - \frac{3}{2}\frac{n_e}{\omega_e \tau_e}\hat{\vec{b}} \times \nabla T_e \tag{4.15}$$

is the momentum exchange term due to friction between the two species for a hydrogenic plasma, $\hat{\vec{b}}$ is the unit vector parallel to the magnetic field, $\vec{u} = \vec{v}_e - \vec{v}_i$, $\omega_e$ is the electron cyclotron frequency, and $\tau_e$ is the inverse electron-ion collision frequency. Figure (4-26) shows the coordinate system used for this analysis. The $s$-direction is parallel to the magnetic field, $w$-direction is perpendicular to the magnetic field but on the flux surface, and the $r$-direction is normal to the magnetic flux surface. The toroidal component of Eqs. (4.14) and (4.15) with the assumption of toroidal symmetry ($\partial/\partial\phi = 0$) is

$$\begin{aligned} 0 &= -en_e E_\phi + en_e v_{er} B_\theta - \frac{m_e n_e}{\tau_e} u_\phi + 0.49 \frac{m_e n_e}{\tau_e}\frac{B_\phi}{B} u_s \\ &\quad -0.71 n_e \frac{B_\phi}{B}\frac{\partial T_e}{\partial s} - \frac{3}{2}\frac{B_\theta}{B}\frac{n_e}{\omega_e \tau_e}\frac{\partial T_e}{\partial r}, \end{aligned} \tag{4.16}$$

where $\phi$ represents the toroidal direction and $\theta$ represents the poloidal direction. Solving Eq. (4.16) for $v_{er}$, the bulk electron (and ion) flow in the r direction, yields

$$\begin{aligned} v_{er} &= \frac{E_\phi}{B_\theta} - \frac{m_e}{e^2 n_e}\frac{1}{\tau_e B_\theta} J_\phi - 0.49 \frac{m_e}{e\tau_e B_\theta}\frac{B_\phi}{B} u_s + 0.71 \frac{B_\phi}{B}\frac{1}{eB_\theta}\frac{\partial T_e}{\partial s} \\ &\quad + \frac{3}{2}\frac{1}{eB}\frac{1}{\omega_e \tau_e}\frac{\partial T_e}{\partial r}, \end{aligned} \tag{4.17}$$

where $J_\phi = -en_e u_\phi$. $u_s$ and the temperature gradient can be reduced to toroidal and poloidal projections using toroidal symmetry and the assumption that there is

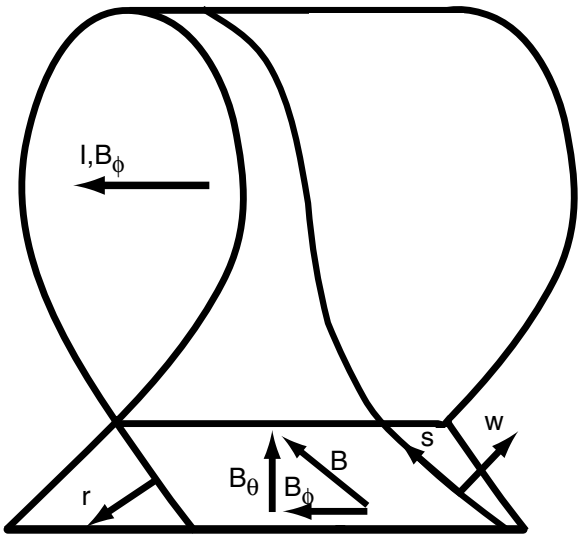


Figure 4-26: Coordinate system used in the derivation of the thermoelectric radial drift.

no poloidal current in this region ($u_\theta = 0$). Therefore Eq. (4.17) can be written as,

$$\begin{aligned} v_{er} &= \frac{E_\phi}{B_\theta} + \frac{m_e}{e^2 n_e}\frac{1}{\tau_e B_\theta}\left[1 - 0.49\alpha^{-1}\right] J_\phi + 0.71\alpha^{-1}\frac{1}{eB_\phi}\frac{\partial T_e}{\partial l_\theta} \\ &\quad + \frac{3}{2}\frac{1}{eB_\phi}\alpha^{-\frac{1}{2}}\frac{1}{\omega_e \tau_e}\frac{\partial T_e}{\partial r}, \end{aligned} \tag{4.18}$$

where $\alpha = \left(1 + B_\theta^2/B_\phi^2\right)$ and $l_\theta$ is distance on a flux surface in the poloidal direction. Since, $\alpha \approx 1$,

$$v_{er} \approx \frac{E_\phi}{B_\theta} + 0.51\frac{m_e}{e^2 n_e}\frac{1}{\tau_e B_\theta} J_\phi + 0.71\frac{1}{eB_\phi}\frac{\partial T_e}{\partial l_\theta} + \frac{3}{2}\frac{1}{eB_\phi}\frac{1}{\omega_e \tau_e}\frac{\partial T_e}{\partial r}. \tag{4.19}$$

A similar derivation can be done for the ions and yields the same result.

The first term of equation 4.19 can be estimated to be $\sim 0.25$ m/s with $E_\phi \approx 0.25$ V/m and $B_\theta \approx 1$ Tesla. The third term can be estimated to be $\sim 60$ m/s with $\frac{\partial T_e}{\partial \ell_\theta} \approx 500$ eV/m and $B_\phi \approx 6$ Tesla. For the second term to on the same order as the third term it must have current densities of greater than 25 MA/m$^2$ (assuming $n_e = 5 \times 10^{19}$ m$^{-3}$ and $T_e = 30$ eV), which is larger than the current densities in the core. For the fourth term to be on the order of the third the radial temperature gradient

must be $\approx 10^5$ times steeper than the poloidal temperature gradient (typically only ten times steeper). Therefore, of the four terms in equation 4.19 the third term is dominant and will be dealt with exclusively,

$$v_{er} \approx 0.71 \frac{1}{eB_\phi} \frac{\partial T_e}{\partial l_\theta}. \tag{4.20}$$

This means that the existence of a poloidal temperature gradient on the outer leg from the X-point to the strikepoint leads to a radially inward drift of plasma into the PFZ which then recombines, this recombination is observed by the cameras through the $D_\gamma$ emission.

The hypothesis that the dominant source of plasma into the private flux region of the divertor is due to the temperature-gradient-driven $\mathbf{E} \times \mathbf{B}$ drift is also consistent with volumetric recombinations versus line-averaged density for the three divertor regions in figures 4-20, 4-21, and 4-22. Figure 4-22 shows a peak in the volumetric recombinations in the private flux region at $\bar{n}_e \approx 1.5 \times 10^{20}$ m$^{-3}$. The lower density increase in volumetric recombinations can be explained by the fact that the outer divertor in these plasmas is in a high-recycling regime and therefore the temperature gradient along the outer leg is increasing as the density is increasing. As the temperature gradient increases the flux into the divertor increases and the number of volumetric recombinations increases. At $\bar{n}_e \approx 1.5 \times 10^{20}$ m$^{-3}$ the outer divertor begins to detach and the region of shallow temperature gradient behind the detachment front begins to expand up the outer leg until it reaches the x-point at the highest densities. Therefore the region of steep temperature gradient decreases in length along the outer leg and corresponds to a decrease in the amount of volumetric recombinations in the private flux region. This also explains why the region below $\bar{n}_e \approx 1.5 \times 10^{20}$ m$^{-3}$ is referred to as the attached region and the region above this density referred to as the detached region. The outer divertor region, in figure 4-21, shows no change in the amount of volumetric recombination until it detaches and then there is a significant increase in the volumetric recombination rate. This is also as expected. The inner divertor region recombination rates, in figure 4-20, show no measurable change until

the outer divertor detaches and then the volumetric recombination rate decreases. This decrease could be due to an added poloidal flow towards the outer divertor due to the increase in recombinations in the outer divertor region.

The qualitative agreement between the hypothesis that the drift is due to poloidal temperature gradient (equation 4.20) and the observations can be seen beginning with the first case, Fig. (4-23), where the inner nose is detached and the outer nose is attached. The poloidal temperature gradient is shallow (50 $\rightarrow$ 25 eV) and the density is low enough along the outer leg that only a weak flux of particles ($\Gamma A \sim 10^{20}$ particles $s^{-1}$) enter the PFZ through the outer leg. With this weak flux of particles, the density, volumetric recombination, and the subsequent $D_\gamma$ emission is small, and in fact very little $D_\gamma$ emission is seen. In the second case, Fig. (4-24) can be described as a high-recycling case, where pressure is constant on a flux surface, but not poloidal density and temperature. Therefore there should be more plasma and recombination in the PFZ, since the poloidal $T_e$ gradient is larger, and in fact more recombination is observed. In the last case, Fig. (4-25), the region of sharp temperature gradient has moved all the way to the x-point. There is only a shallow gradient along the outer leg. [64] This yields no flow from the outer leg into the PFZ. Instead, in this case the large poloidal gradient will drive a flow into the closed-field line region directly above the x-point. As the density increases, the flux into the main plasma above the x-point increases, and a cold, dense MARFE [38] forms above the x-point eventually leading to a disruption. This is seen on Alcator C-Mod.[41, 40] Through all of these cases the parallel transport in the PFZ behaves as would be expected, the plasma travels along the magnetic field lines to the divertor plates with recombinations occurring simultaneously.

The distribution of the $D_\gamma$ emission does not agree with the hypothesis that perpendicular *diffusion* is the dominant mechanism fueling the PFZ. If diffusion were the main cause of particle flux into the PFZ, one would expect the particle flux to increase when the divertor detachment is extended to the x-point due to the large perpendicular density gradient formed on the outer leg. This is not observed and therefore cross-field diffusion is not considered to be the dominant mechanism.

Although the temperature gradient driven $\mathbf{E} \times \mathbf{B}$ can qualitatively explain the divertor recombination profiles, the next question must be does it quantitatively explain the recombination measurements? Below is a quantitative analysis of a single high-recycling outer divertor discharge.

The total number of particles per second that drift into the private flux region is

$$I_e = \int n_e v_{er} \, dA, \tag{4.21}$$

where $\int \ldots dA$ is the integral over the total area of the outer leg. By substituting Eq. (4.20) into Eq. (4.21) and recognizing that in a tokamak $B_\phi = B_o R_o / R$, where $B_o$ and $R_o$ are the magnetic field and radial position of the center of the main plasma, the particle current into the PFZ can be written as

$$I_e \approx \frac{1.42\pi}{e B_o R_o} \int_{\mathrm{sp}}^{\mathrm{x}} n_e R^2 \frac{\partial T_e}{\partial l_\theta} \, dl_\theta, \tag{4.22}$$

where sp is the strikepoint, x is the x-point. In the attached case ($\partial p_e / \partial s = 0$) this integral can be approximated as,

$$I_e \approx \frac{1.42\pi R^2 p_e}{e B_o R_o} \ln\left(\frac{T_{\mathrm{x}}}{T_{\mathrm{sp}}}\right) \tag{4.23}$$

assuming the variation in $R^2$ is small enough to remove it from inside the integral.

Using the assumption that all plasma particles that enter the PFZ volumetrically recombine in the PFZ and using the approximations that yielded Eq. (4.23), the relation between the PFZ recombination rate and the particle current into the PFZ is

$$\left(\frac{\partial N_e}{\partial t}\right)_{\mathrm{recomb}} \approx \beta p_e, \tag{4.24}$$

where

$$\beta = \frac{1.42\pi R^2}{e B_o R_o} \ln\left(\frac{T_{\mathrm{x}}}{T_{\mathrm{sp}}}\right). \tag{4.25}$$

Figure (4-27) shows the comparison of the PFZ recombination rate as a function of peak plasma pressure on the outer leg for a shot where the line-averaged density

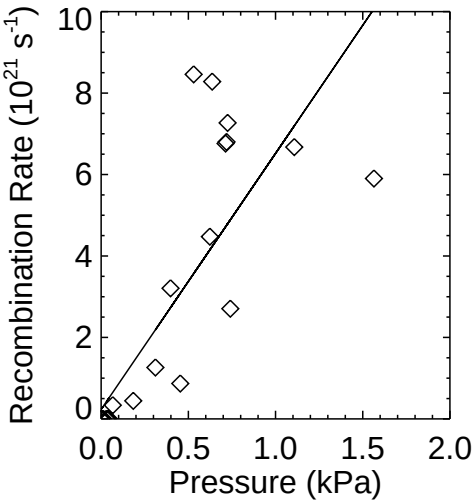


Figure 4-27: A plot of the PFZ recombination rate as a function of the peak electron pressure on the outer leg when the outer leg was attached. The line shown in is a linear regression fit of the data.

ranged from $1.0\times10^{20}$ m$^{-3}$ to $1.3\times10^{20}$ m$^{-3}$, and was entirely in the attached divertor regime. The linear dependence is what is expected from Eq. (4.24).

The line shown in Fig. (4-27) is a linear regression fit of the data. This yields a slope of $6.3 \times 10^{18}$ recombinations s$^{-1}$ Pa$^{-1}$ with an R$^2$ value of 0.826. Given that $R \approx 0.6$m, $B_o = 5.4$T, and $R_o = 0.67$m and if $ln\left(T_{\rm X}/T_{\rm sp}\right) \approx 2.25$ then, the slope is the same as predicted from Eq. (4.25).

**Conclusions**

$D_\gamma$ emission shows the existence of plasma in the private flux zone of the Alcator C-Mod tokamak. It is generated by the volumetric recombination of a cold, high density plasma. Using spectroscopic measurements we observe that there is a significant recombination rate in this region, which is most likely fed by cross-field transport from across the separatrix. From the parallel fluid equations, which on Alcator C-Mod is believed to be described classically, a radial drift is derived to explain the behavior of the PFZ plasma. The dominant drift is due to a poloidal temperature gradient. This mechanism for the flux into the PFZ is consistent with the observed

behavior of the plasma.

In the attached case the flux into the PFZ is linear with the plasma pressure and logarithmic with respect to the ratio of x-point temperature to temperature at the divertor plate. This linear behavior is consistent with Alcator C-Mod observations based on the recombination rate determinations.

As the line averaged density is increased, the outer divertor leg becomes detached and a sharp poloidal temperature gradient is located at or slightly above the x-point, thus reducing the flow into the private flux region. As the density is increased further, plasma flows into the x-point from the outer divertor region due to the large local temperature gradient. This cools the plasma on the closed flux surfaces enough to generate an x-point MARFE, which subsequently leads to disruption. This also has been observed on Alcator C-Mod.[41, 40]

### 4.3.2 Inner Wall $D_\alpha$ Emission on Alcator C-Mod

Little work has been published on measuring or characterizing the scrape-off layer (SOL) near the inner wall of a tokamak. What work that has been done noted significant differences between the inner SOL (high-field-side) and the outer (low-field-side) SOL. On Alcator C [35] (a limited tokamak) it was noted that there was a poloidal variation of density in the shadow of the limiter with the minimum occurring on the high-field-side. Another result was that the radial density e-folding length also had a minimum value on the high-field-side SOL, with the maximum occurring on the low-field-side SOL. Another interesting result from the ASDEX tokamak [12] (a diverted tokamak) is that fluctuations typical of the low-field-side SOL would be observed on the high-field-side SOL when in a single null discharge, but when in a balanced double null discharge the fluctuations were absent from the high-field-side SOL. More recently, it has been observed on Alcator C-Mod that the $D_\alpha$ emission at the inner SOL peaks not on the primary separatrix but on the secondary separatrix (defined precisely below and in Fig 4-28). The previous, but not fully understood, observations along with the more recent observations from Alcator C-Mod have prompted a more thorough investigation into the inner SOL.

The following sections will describe the experimental technique used to investigate the inner SOL, present the experimental results, compare these results with a simple one-dimensional kinetic neutral model, and interpret the results from the measurements and the model.

**Experimental Setup and Analysis**

To observe the $D_\alpha$ emission from the inner wall region, the visible imaging CCD camera (DANT), described in Sec. 4.1, was used. This camera views the inner wall tangentially. A poloidal cross-section of the view is shown in Fig. 4-28. The camera is filtered for $D_\alpha$ using an interference filter located directly in front of the lens and is absolutely calibrated, as described in Sec. 4.1. The camera is located ~19.5 cm below the midplane of the tokamak and has a slight upward tilt of ~5 degrees. This view was calibrated by fitting the observed spacings between the tiles on the inner column to the expected location of the spacings on the image plane, similar to the calibration of the view for the divertor viewing cameras, see Section 4.1.

Although in principle an Abel inversion can be performed using the array of pixels whose view lies in the horizontal plane, the pixel to pixel noise renders this approach impractical. To obtain emission profiles from this region, the brightness profile was fitted to a line-integrated brightness profile based on an assumed emission profile shape. The emission profile was assumed to have the form,

$$\epsilon(r) = \begin{cases} c_0 \exp\left[\frac{r-r_0}{\lambda_-}\right] & \text{if } r \le r_- \\ \epsilon_0 + c_1 (r-r_0)^2 & \text{if } r_- \le r \le r_+ \\ c_2 \exp\left[\frac{-r+r_0}{\lambda_+}\right] & \text{if } r_+ \le r \end{cases} . \tag{4.26}$$

Figure 4-29 shows a sample emission based on equation 4.26. The variables $r_0$, $r_-$, and $r_+$ are the locations of the peak emission, the high-field-side boundary between the parabolic and exponential sections of the emission and the low-field-side boundary between the parabolic and exponential sections, respectively. The total number of free parameters can be reduced to 5 (i.e., $\epsilon_0$, $r_0$, $\lambda_-$, $\lambda_+$, and $c_2$) by requiring that the function be differentiable at $r_-$ and $r_+$. This constraint and the constraints

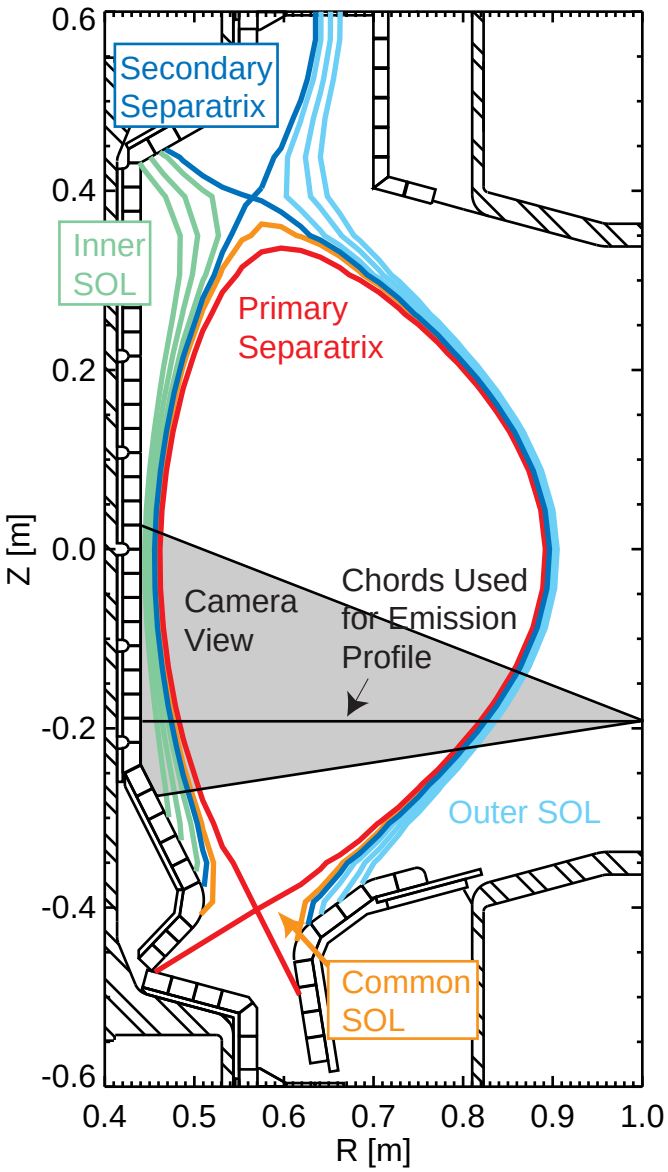


Figure 4-28: The inner, outer and common scrape-off layer in a typical lower single null discharge, along with the poloidal projection of the camera view.

$r_- < r_0 < r_+$ and $c_1 < 0$ yield the following relations that allow the reduction of free parameters:

$$
\begin{aligned}
c_0 \exp\left[\frac{r_- - r_0}{\lambda_-}\right] &= \epsilon_0 + c_1 \left(r_- - r_0\right)^2 && (4.27)\\
c_2 \exp\left[\frac{-r_+ + r_0}{\lambda_+}\right] &= \epsilon_0 + c_1 \left(r_+ - r_0\right)^2 && (4.28)\\
\frac{c_0}{\lambda_-} \exp\left[\frac{r_- - r_0}{\lambda_-}\right] &= 2c_1 \left(r_- - r_0\right) && (4.29)\\
-\frac{c_2}{\lambda_+} \exp\left[\frac{-r_+ + r_0}{\lambda_+}\right] &= 2c_1 \left(r_+ - r_0\right) && (4.30)\\
& && (4.31)
\end{aligned}
$$

The solution to these equations in terms of the five parameters $\epsilon_0$, $r_0$, $\lambda_-$, $\lambda_+$, and $c_2$ is

$$
\begin{aligned}
r_- &= r_0 + \lambda_- \left[1 - \left(1 - \frac{\epsilon_0}{\lambda_-^2 c_1}\right)^{1/2}\right] && (4.32)\\
r_+ &= r_0 - \lambda_+ \left[1 - \left(1 - \frac{\epsilon_0}{\lambda_+^2 c_1}\right)^{1/2}\right] && (4.33)\\
c_0 &= \left[\epsilon_0 + c_1 \left(r_- - r_0\right)^2\right] \exp\left(\frac{r_0 - r_-}{\lambda_-}\right) && (4.34)\\
c_2 &= \left[\epsilon_0 + c_1 \left(r_+ - r_0\right)^2\right] \exp\left(\frac{-r_0 + r_+}{\lambda_-}\right) && (4.35)
\end{aligned}
$$

The measured brightness profiles were fitted to the brightness profile of the assumed emission profiles including a constant brightness offset (presumably coming from the outer parts of the plasma through which the camera must view),

$$b(y) = 2 \int_y^a \epsilon(r) \frac{r\ dr}{\left(r^2 - y^2\right)^{1/2}} + b_0. \qquad (4.36)$$

Expanding Eq. 4.36 yields

$$b(y) = 2c_2 \left(a^2 - y^2\right)^{1/2} \exp\left(\frac{-a + r_0}{\lambda_+}\right) +$$

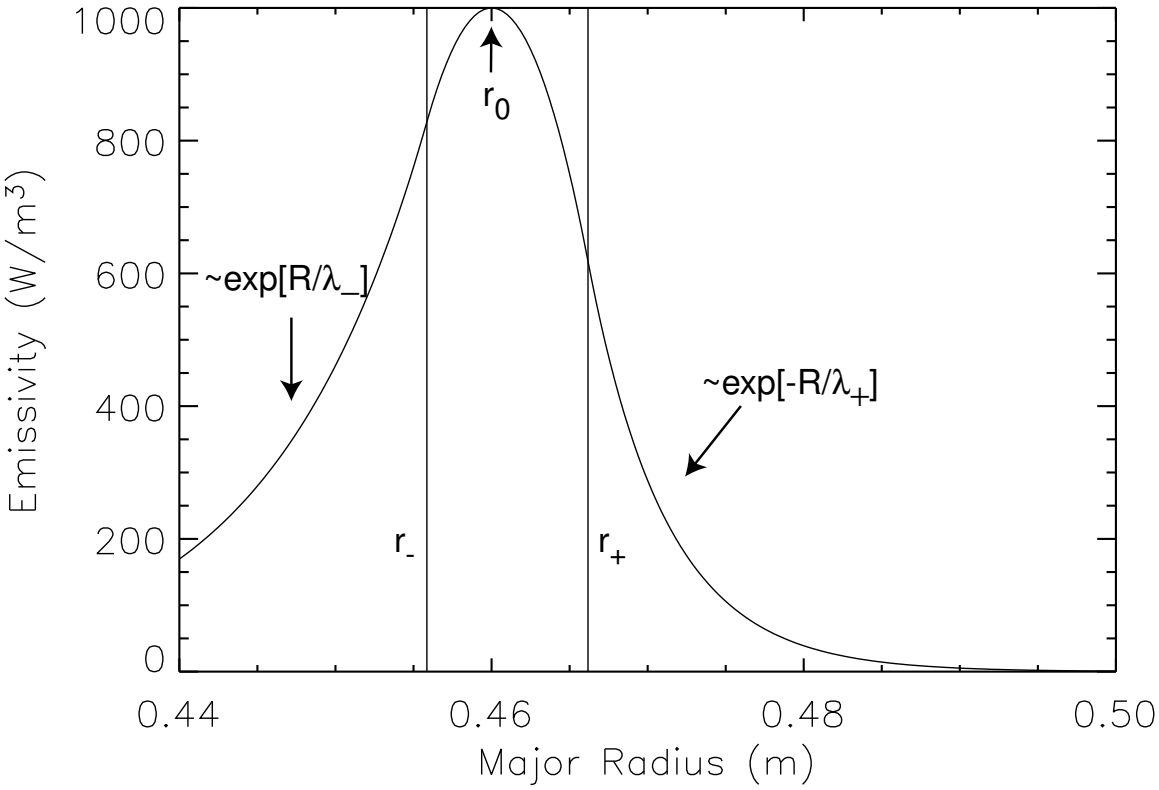


Figure 4-29: A sample of the emission profile assumed in the analysis of the $D_\alpha$ emission near the innerwall.

$$+\frac{2c_2}{\lambda_+}\int_y^a \left(r^2-y^2\right)^{1/2}\exp\left(\frac{-r+r_0}{\lambda_+}\right)dr+b_0, \tag{4.37}$$

for $r_+ \le y$,

$$\begin{aligned} b(y) &= 2\left(\epsilon_0+c_1r_0^2\right)\left(r_+^2-y^2\right)^{1/2}- \\ &\quad -4c_1r_0\left\{\frac{r_+}{2}\left(r_+^2-y^2\right)+\frac{y^2}{2}\ln\left[\frac{r_+ +\left(r_+^2-y^2\right)^{1/2}}{y}\right]\right\}+ \\ &\quad +2c_1\left[\frac{1}{3}\left(r_+^2-y^2\right)^{3/2}+y^2\left(r_+^2-y^2\right)^{1/2}\right]+ \\ &\quad +2c_2\left(a^2-y^2\right)^{1/2}\exp\left(\frac{-a+r_0}{\lambda_+}\right)- \\ &\quad -2c_2\left(r_+^2-y^2\right)^{1/2}\exp\left(\frac{-r_++r_0}{\lambda_+}\right)+ \\ &\quad +\frac{2c_2}{\lambda_+}\int_{r_+}^a\left(r^2-y^2\right)^{1/2}\exp\left(\frac{-r+r_0}{\lambda_+}\right)dr+b_0, \end{aligned} \tag{4.38}$$

for $r_- \le y \le r_+$, and

$$\begin{aligned} b(y) &= 2c_0\left(r_-^2-y^2\right)^{1/2}\exp\left(\frac{r_--r_0}{\lambda_-}\right)- \\ &\quad -\frac{2c_0}{\lambda_-}\int_y^{r_-}\left(r^2-y^2\right)^{1/2}\exp\left(\frac{r-r_0}{\lambda_-}\right)dr+ \\ &\quad +2\left(\epsilon_0+c_1r_0^2\right)\left[\left(r_+^2-y^2\right)^{1/2}-\left(r_-^2-y^2\right)^{1/2}\right]- \\ &\quad -4c_1r_0\left\{\frac{r_+}{2}\left(r_+^2-y^2\right)^{1/2}-\frac{r_-}{2}\left(r_-^2-y^2\right)^{1/2}+\frac{y^2}{2}\ln\left[\frac{r_+ +\left(r_+^2-y^2\right)^{1/2}}{r_- +\left(r_-^2-y^2\right)^{1/2}}\right]\right\}+ \\ &\quad +\frac{2c_1}{3}\left[\left(r_+^2-y^2\right)^{3/2}-\left(r_-^2-y^2\right)^{3/2}\right]+ \\ &\quad +2c_1y^2\left[\left(r_+^2-y^2\right)^{1/2}-\left(r_-^2-y^2\right)^{1/2}\right]+ \\ &\quad +2c_2\left(a^2-y^2\right)^{1/2}\exp\left(\frac{-a+r_0}{\lambda_+}\right)-2c_2\left(r_+^2-y^2\right)^{1/2}\exp\left(\frac{-r_++r_0}{\lambda_+}\right)+ \\ &\quad +\frac{2c_2}{\lambda_+}\int_{r_+}^a\left(r^2-y^2\right)^{1/2}\exp\left(\frac{-r+r_0}{\lambda_+}\right)dr+b_0, \end{aligned} \tag{4.39}$$

for $y \le r_-$. Equations (4.37 - 4.39) when used with equations (4.33 - 4.35) have six free parameters, $\epsilon_0$, the peak emission value, $r_0$, the location in radius of the emission

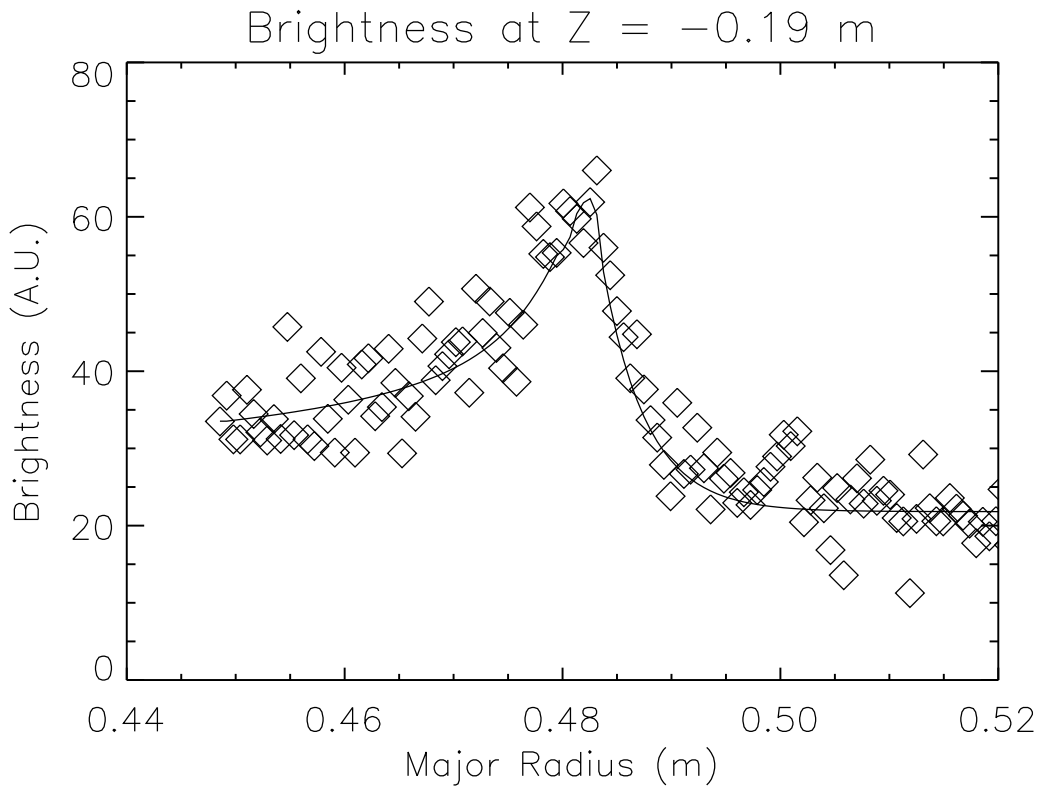


Figure 4-30: A typical brightness profile with the fitted function overplotted. The abscissa is the major radius of the viewing chord's impact parameter.

peak, $\lambda_-$, the scale length of the emission towards the radial axis, $\lambda_+$, the scale length of the emission away from the radial axis, $c_1$, the "peakedness" of the emission, and $b_0$ the brightness offset. The constant brightness offset can be attributed to the twice brightness from the low-field side of the plasma. Equations (4.37 -4.39) also have terms that are left in integral form. These integrals can be numerically integrated since the infinity originally present in Eq. 4.36 has be eliminated. Figure 4-30 shows a typical brightness profile with the fitted function overplotted. This fit can be done for all recorded frames.

### Magnetic Geometry

In a balanced double null discharge there exist two distinct regions of the scrape-off layer, a high-field side scrape-off layer (inner scrape-off layer) and a low-field side scrape-off layer (outer scrape-off layer). In an unbalanced double null configuration

(see figure 4-28) these two regions still exist outside the secondary separatrix. Between the primary and secondary separatrix there exists a region of the scrape-off layer in which the low- and high-field sides are magnetically connected (common scrape-off layer). Figure 4-28 shows the three regions (inner, outer, and commons scrape-off layer) in a typical lower single null discharge.

To investigate the influence the magnetic geometry has on the $D_\alpha$ emission near the inner wall, the magnetic configuration was scanned dynamically from a lower single null (LSN) to a double null (DN) through to an upper single null (USN). Figure 4-31 shows the three configurations that the magnetic geometry was scanned through. The global parameters for this experiment were typical of an L-mode discharge on Alcator C-Mod and kept nearly constant: $B_T = 5.4$ T, $I_p = 0.8$ MA, $\bar{n}_e \approx 10^{20}$ m$^{-3}$. The main magnetic effect of this scan is the location of the secondary separatrix with respect to the primary separatrix, from $\sim 1$ cm from the primary separatrix at the outboard midplane to having no secondary separatrix during double null back to being $\sim 1$ cm from the primary separatrix with a change in the null with which the secondary separatrix is associated.

**Observations**

By fitting the brightness profiles as described in section 4.3.2, the variation of the location of the emissivity peak ($r_0$), the HFS emission scale length ($\lambda_-$), and the LFS emission scale length ($\lambda_+$) were determined. The location of the emissivity peak during the configuration sweep described above is summarized in figure 4-32, and can clearly be seen to follow the secondary separatrix regardless of the null with which the secondary separatrix is associated. The HFS emission scale length, shown in figure 4-33, is relatively constant within the error of this measurement. The LFS emission scale length has a smaller error associated with its measurement and is systematically smaller when the discharge is near double null configuration. The LFS emission scale length measurements are summarized in figure 4-34.

All three of these observations can be explained by a steep plasma density decay beginning at the secondary separatrix and decaying towards the inner wall and a

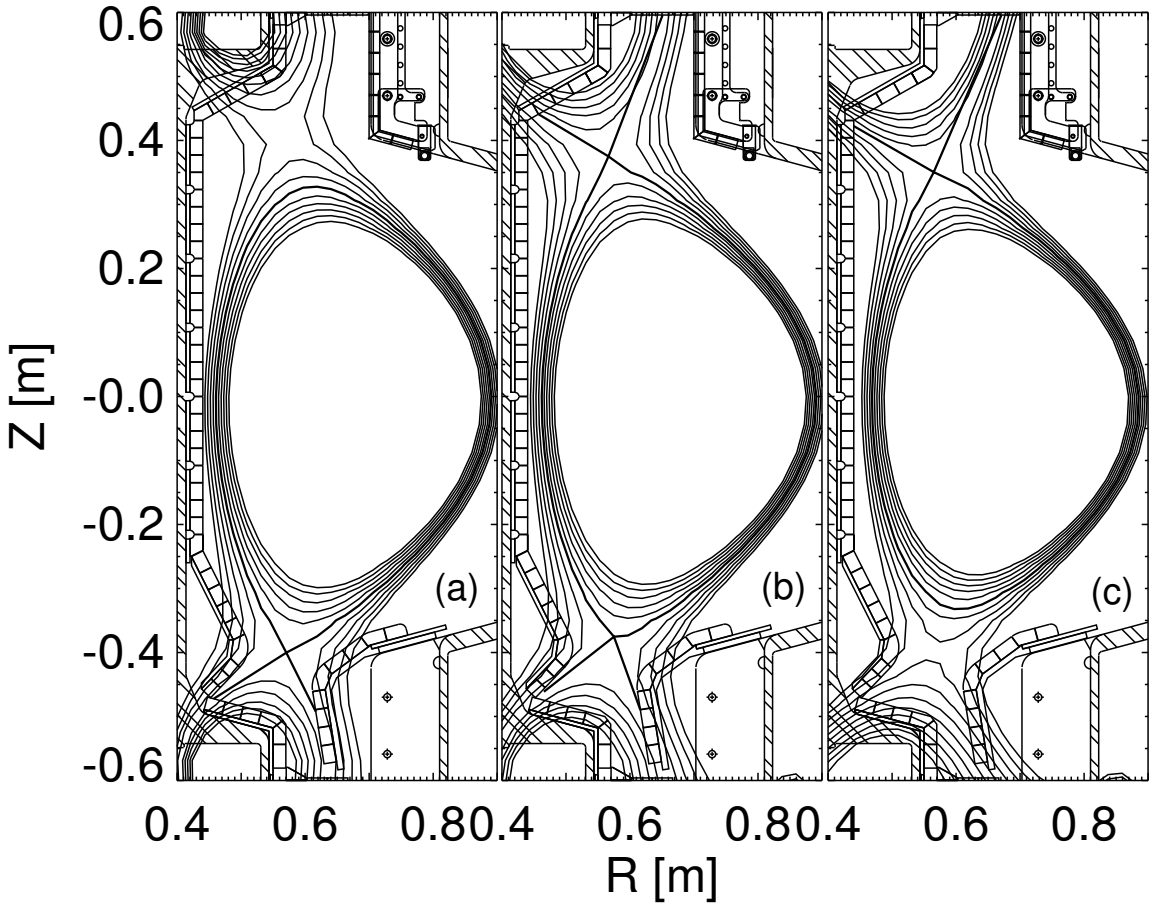


Figure 4-31: The three magnetic geometries that the plasma was scanned through to investigate the influence of the magnetic geometry on the $D_\alpha$ emission near the inner wall. Here (a) is a lower single null configuration, (b) is the double null configuration and (c) is the upper single null configuration.

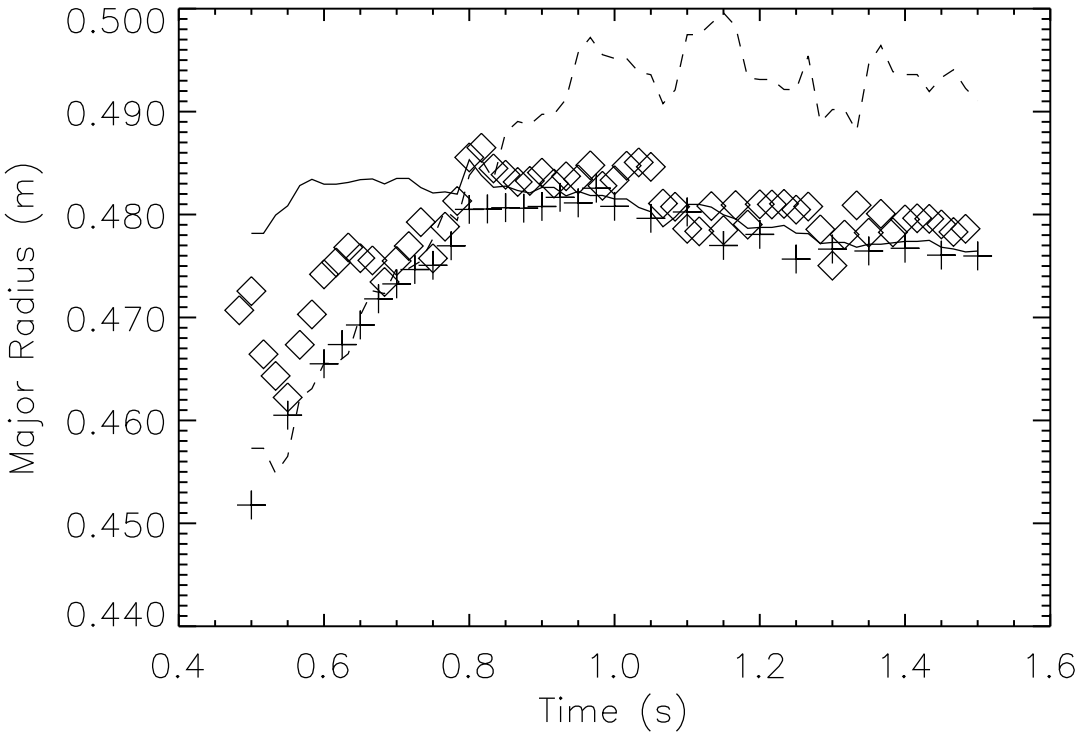


Figure 4-32: Plot showing the location of the peak in the emission from the observations ($\diamond$) and the location of the peak in the emission from the kinetic neutral code KN1D (+) with respect to the location of the flux surface associated with the lower (–) and upper (- -) null.

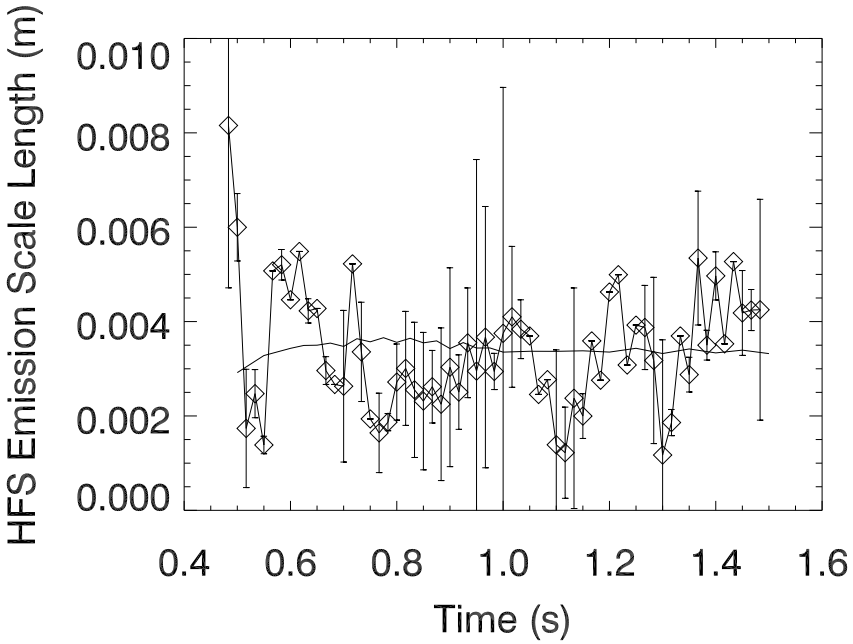


Figure 4-33: Plot showing the high-field-side emission scale length measured from the observations ($\diamond$) and the high-field-side emission scale length calculated from the kinetic neutral code KN1D (–).

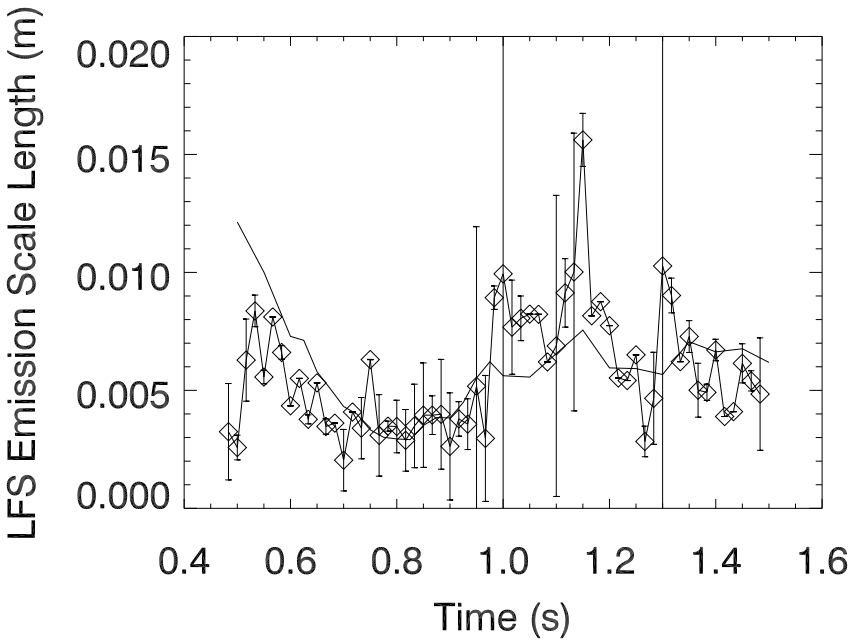


Figure 4-34: Plot showing the low-field-side emission scale length measured from the observations (⋄) and the low-field-side emission scale length calculated from the kinetic neutral code KN1D (–).

relatively flat plasma density profile in the common SOL. In this case the neutral atoms would travel freely until they came near the secondary separatrix where they would begin to ionize. In the common SOL the neutrals would have a nearly constant ionization rate and their density would decay exponentially with a 1/e length approximately equal to the the ionization mean-free-path. Since the $D_\alpha$ emissivity in the temperature range expected ($T_e \geq 5$ eV) has a weak dependence on temperature and a linear dependence on both the electron and neutral density,

$$\epsilon_{D_\alpha} \propto n_e n_o, \tag{4.40}$$

the emissivity will depend on the plasma and neutral profiles. On the HFS of the emission peak the neutrals have a nearly flat density profile and therefore the HFS emission scale length is indicative of the electron density scale length. On the LFS of the emission peak the electron density varies more slowly and LFS emission scale length is governed by the neutral density. The profile of the neutral density in this region has an exponential decay determined by the ionization mean-free-path and therefore the LFS emission scale length is indicative of this ionization mean-free-path. The peak in the emissivity occurs where the product of the electron and neutral densities are a maximum which occurs on the secondary separatrix.

### Modeling

A one dimensional space, two dimensional velocity, kinetic neutral code (KN1D) [32] was used to simulate the plasma-neutral interactions near the inner wall of the tokamak. This code requires as inputs the plasma profiles (temperature, density, and velocity) and the neutral pressure at the inner wall. KN1D uses many molecular and atomic processes to determine the distribution functions of both the atomic and molecular neutrals. The processes included are (1) charge exchange collisions, (2) electron-impact ionization and dissociations, (3) elastic self-collisions (atomic and molecular), and (4) a variety of elastic cross-collisions (atom-ion, atom-molecule, molecule-ion).

The inputs used in simulating the inner wall SOL region included using typical plasma profiles in the common SOL, as measured on the LFS midplane by a scanning Langmuir probe, but with a sharp decay of the plasma density in the inner SOL ($\lambda_n = 3$ mm) beginning at the at the secondary separatrix. Using the LFS common SOL values for the plasma profile in the HFS common SOL is adequate since the LFS emission scale length in the KN1D output only changed by a few percent when the common SOL density profiles was varied from a flat density to a flat temperature profile while keeping pressure constant on a flux surface. The input value of the neutral molecular pressure at the inner wall is unimportant since the absolute scale of the KN1D output $D_\alpha$ emissivity is a linear function of this neutral pressure. When the neutral pressure at the inner wall was chosen to agree with the measured emissivity profile the pressures required were in the range of 0.6 to 3 mTorr.

The results of the simulations show an excellent agreement with the location of the emission peak (figure 4-32) and the LFS emission scale length (figure 4-34) and only a moderate agreement with the HFS emission scale length (figure 4-33). Since the location of the emission peak is typically where the electron density begins its steep decent towards the inner wall and the KN1D location of the emission peak is consistently below the emission peak location obtained from the camera data, this suggests that the plasma profiles used as input to KN1D should begin the sharp decay in plasma density slightly to the high field side of the secondary separatrix. The LFS emission scale length has a decrease in the value as the magnetic configuration nears double null (at 0.8 s). This decrease in scale length is due to the secondary separatrix approaching regions of higher density. The higher density yields a shorter ionization mean-free-path for the neutrals and as described earlier a shorter emission scale length. The constancy of the HFS emission scale length is because the $D_\alpha$ emission profile on the HFS of the peak is dominated by the plasma density profile, which is given as an input to the code. Therefore the LFS emission scale length result from the model could be made to match the measured result more closely. Since the constant value result is within the error bars for the measurement and little more information could be obtained by forcing the two results to match the constant value was seen

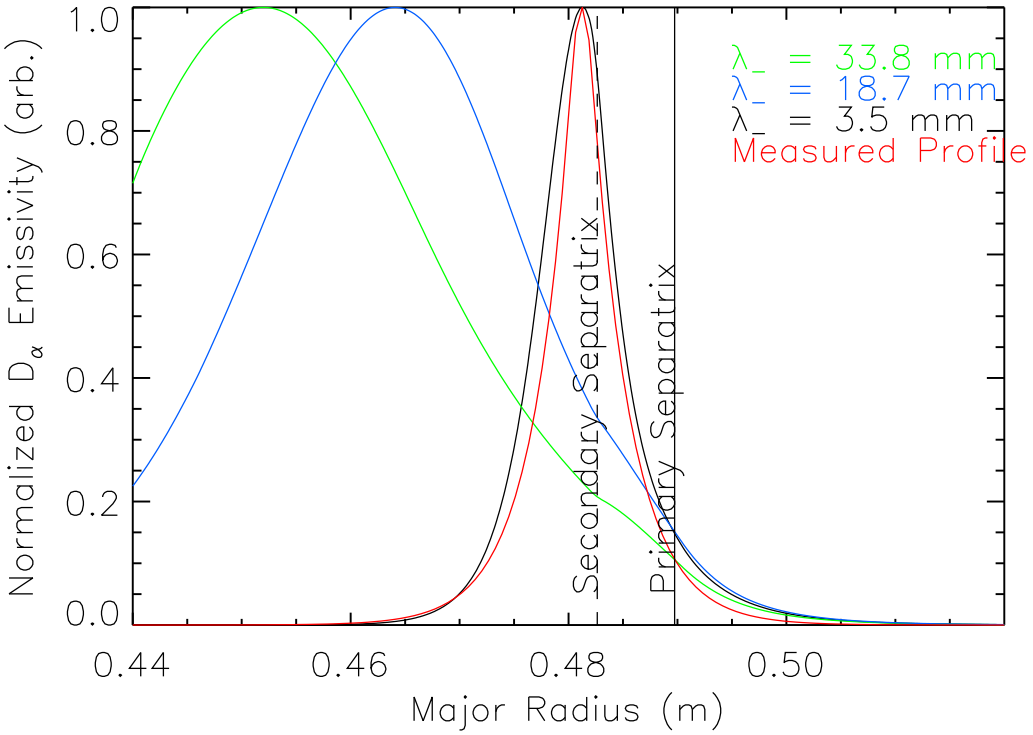


Figure 4-35: Plot of the $D_\alpha$ emission output from KN1D where the plasma density scale length is varied from 33.8 mm (the value if no change was made when compared to the outer SOL) to 3.5 mm (the best fit to the measured data).

as adequate. Figure 4-35 shows the $D_\alpha$emission profile for one modelled time slice varying the density scale length in the region between the secondary separatrix and the inner wall, showing that the strong density gradient beginning at the secondary separatrix is necessary to replicate the experimental observations. The three plasma density scale lengths used are (1) keeping the same plasma profile near the inner wall as is measured on the outboard side ($\lambda_- = 33.8$mm), (2) using a scale length that best matched the observed measurement ($\lambda_- = 3.5$mm), and (3) an intermediate value ($\lambda_- = 18.7$mm) to show the dependence of the solution on this scale length.

### Other Supporting Data

Subsequent measurements on Alcator C-Mod have supported the results presented above. These measurements were obtained by Brian LaBombard using a scanning

Langmuir probe recently installed on the inner wall.

The scanning Langmuir probe is a single tungsten wire in a carbon fiber body mounted at the midplane on the inner wall. The probe is mounted such that the wire is horizonal and has an axis in the vertical direction about which it rotations. The scanning motion is obtained by a solenoid whose placement and applied magnetic field, in conjunction with the toroidal magnetic field, applies a torque to the scanning probe allowing it to swing in the plasma by up to 1.5 cm. This probe is then used to obtain plasma temperature, density, and potential profiles of the inner wall region.

Figure 4-36 show a series of density profiles obtained by the inner wall scanning probe (ISP) compared to an outboard scanning probe (ASP) for different distances between the primary and secondary separatrices. In all cases the electron density does have a stronger decay in the region between the secondary separatrix and the inner wall. The density does begin its steepening on the LFS of the secondary separatrix as was suggested by the modeling results. These measurements validate the profiles used in the KN1D model.

### Conclusions

Summarizing the observed and simulated results, I note (1) the $D_\alpha$ emissivity peaks on the secondary separatrix, (2) the HFS emission scale length has no systematic dependence on the magnetic geometry, and (3) the LFS emission scale length decreases as the discharge approaches a double null configuration. The location of the emission and the independence of the HFS emission scale length can be explained by postulating a sharp plasma density decay beginning at the secondary separatrix and decreasing toward the inner wall. The HFS emission scale length is a measure of that plasma density decay length. The LFS emission scale length can be explained by the ionization mean-free-path of the neutrals into the common SOL, and therefore is a measure of the effective ionization mean-free-path for the thermal neutrals moving toward the plasma from the secondary separatrix.

The existence of a sharp decay of the plasma density beginning at the secondary separatrix can explained by considering the typical SOL paradigm. In the SOL

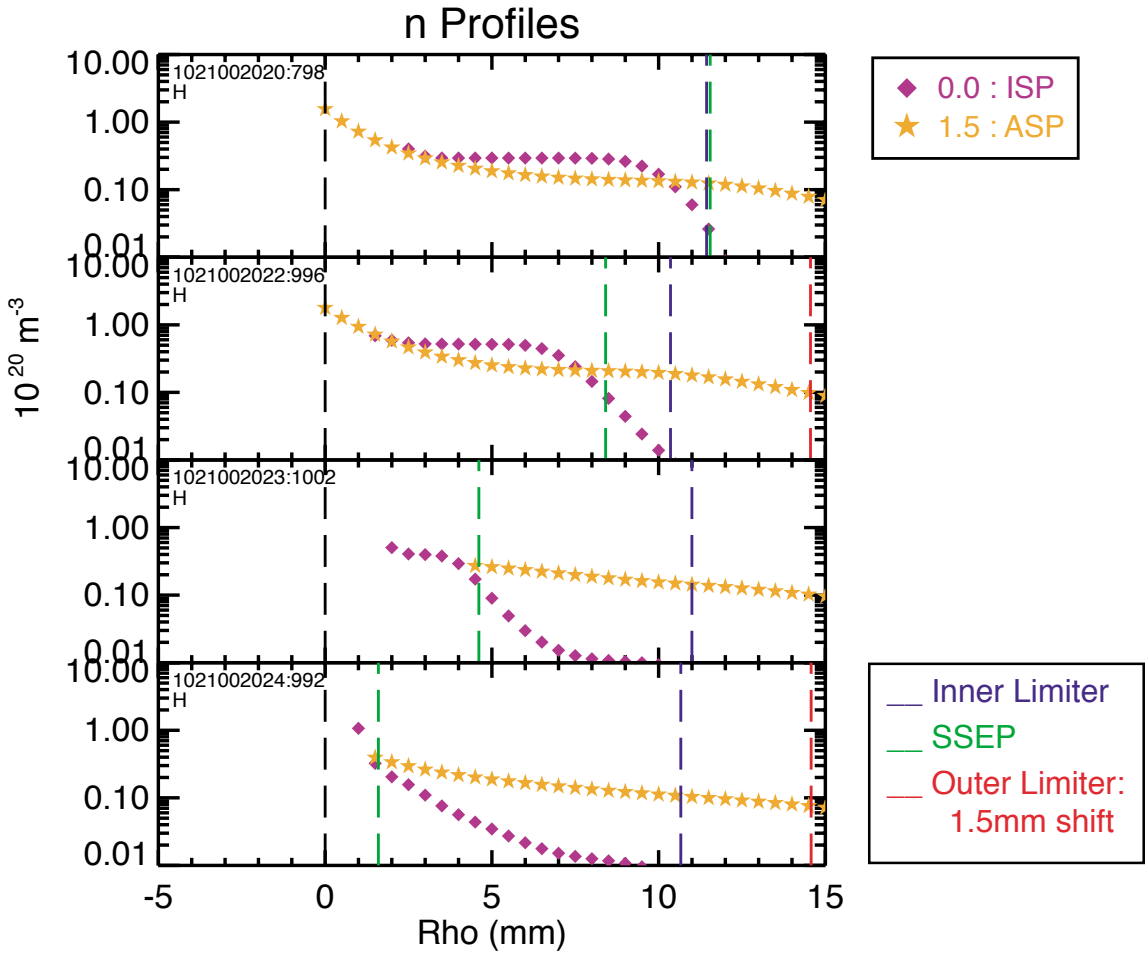


Figure 4-36: A series of density profiles obtained by the inner wall scanning probe (ISP) compared to an outboard scanning probe (ASP) for different distances between the primary and secondary separatrices. (B. LaBombard)

paradigm all plasma in the SOL flows along field lines to the divertor plate or limiter and the radial SOL plasma profiles are determined by this parallel transport. On the LFS of the common SOL and in the outboard SOL there is clear evidence that in some cases the perpendicular (radial) particle transport competes with or is larger than the parallel transport. This flattens the plasma profiles and is contrary to the typical SOL paradigm. [36, 33] In the HFS SOL I believe the profiles in the *common* SOL are set by the LFS dynamics, and that in the inner SOL the profiles are more in line with the SOL paradigm. This explanation is consistent with the previous observations mentioned in the beginning of this section. The density decay length was shorter at the HFS of Alcator C because it was not connected to the LFS. The fluctuations measured at the inner wall on ASDEX during single-null discharges were the effect of the LFS dynamics on the HFS common SOL, while the lack of measured fluctuations during double-null discharges occurred because the inner SOL was not connected to the LFS and therefore was not influenced by the transport there.

### 4.3.3 Divertor Continuum Emission

The electron temperature of an isothermal deuterium plasma can be calculated by taking the ratio of the emission of a deuterium line in local thermal equilibrium (LTE) and the emission of continuum assuming the continuum is entirely due to ion-electron bremsstrahlung and radiative recombination [18]. (This is the so-called "line-to-continuum ratio" method for determining $T_e$) In this case the ratio is strictly a function of electron temperature and all one has to do is measure these two quantities and a value for the electron temperature can be obtained. This was attempted on Alcator C-Mod using the deuterium $n = 5 \rightarrow 2$ transition ($D_\gamma$) and the continuum level between 420 and 430 nm. The measurements yielded temperatures consistently higher than the temperatures measured by fitting the high-$n$ deuterium Balmer lines to a Saha distribution (as described in Sec. 4.3.1) and by measuring the slope of the free-bound continuum between $\sim$ 85 and 91 nm. [58]. Figure 4-37 shows the theoretical ratio of the $D_\gamma$ emission to continuum emission (420-430nm) as a function of temperature.

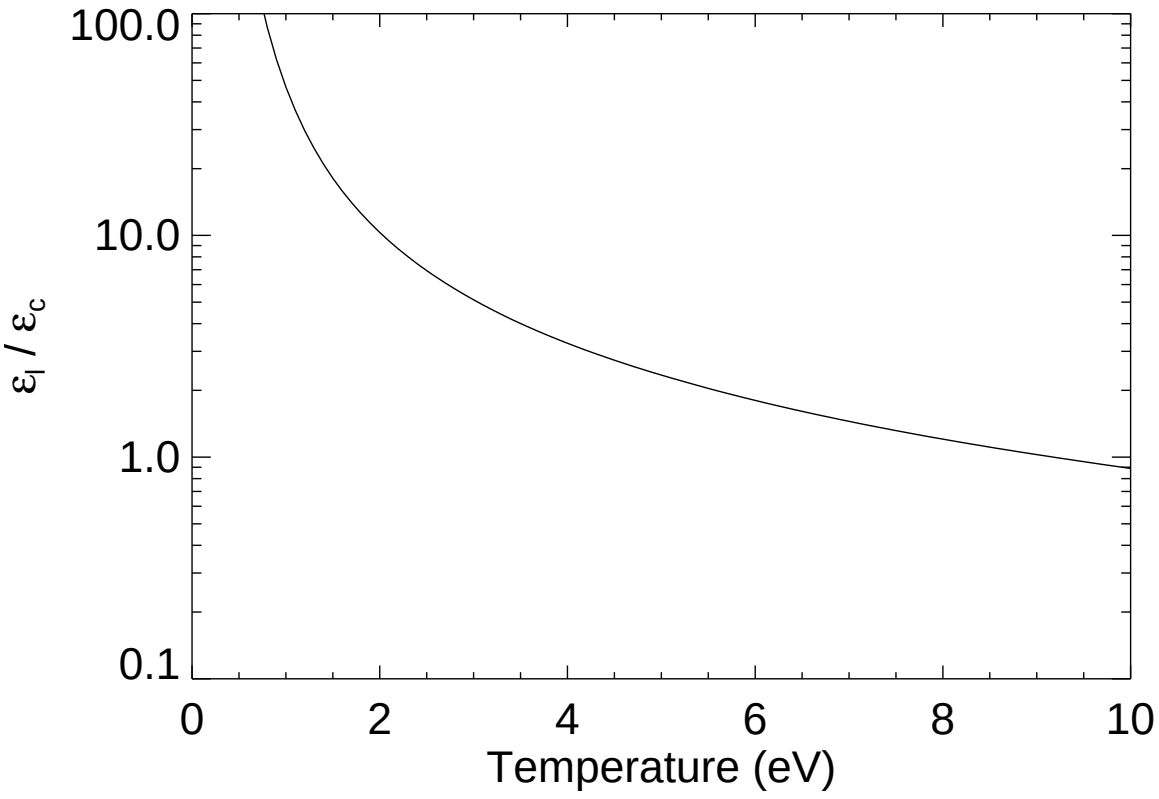


Figure 4-37: Plot of the ratio of the $D_\gamma$ emission to continuum emission (420-430 nm) as a function of electron temperature.

The failure of the line-to-continuum ratio method to produce electron temperature measurements consistent with the other methods discussed can be attributed to additional continuum being generated in the divertor other than bremsstrahlung or radiative recombination. The failure of the method is not due to the $D_\gamma$ line not being in LTE because 1) this assumption is also used when calculating the temperature using the high-$n$ Balmer series, and 2) the relative intensity agrees well with the expected fit of the intensities of the other lines. The unaccounted-for continuum emission is approximately an order of magnitude too high when compared to the temperatures measured by the VUV and the visible spectrometers. Other atomic sources of continuum emission have been calculated ($H^-$, atom-ion bremsstrahlung, etc.) and none have been able to account for the extra continuum emission.

It is shown that the emission profile of the continuum is peaked in the same region as the recombining plasma described in Sec. 4.3.1. The most probable source of this continuum is due to molecular effects. It is most probable only because the other atomic and plasma sources that have been considered have been eliminated as the cause. The qualitative analysis of these other sources are discussed. The hypothesis that the continuum is due to radiative dissociation of the deuterium molecule is presented. This emission occurs when a deuterium molecule is in an excited electronic state (i.e., $a^3\Sigma_g^+$) that decays into a repulsive electron state with no bound energy levels ($b^3\Sigma_g^+$) emitting a continuous spectrum of photons. [62, 26, 8, 11] Unfortunately, it is concluded that there is probably not enough $D_2$ or $D_2^+$ present in the detached plasma to account for the magnitude of the emission. Thus the continuum emission remains unexplained.

### Experimental Technique

Both the $D_\gamma$ and the continuum emission profiles are generated using the same technique as described in sections 4.2 and 4.1. The camera used to obtain $D_\gamma$ profiles is set up exactly as described in in section 4.1, with the exception being that it is filtered about 434 nm instead of 656 nm. The camera used to obtain the continuum emission profiles is set up the same as described in section 4.1 with the exception that

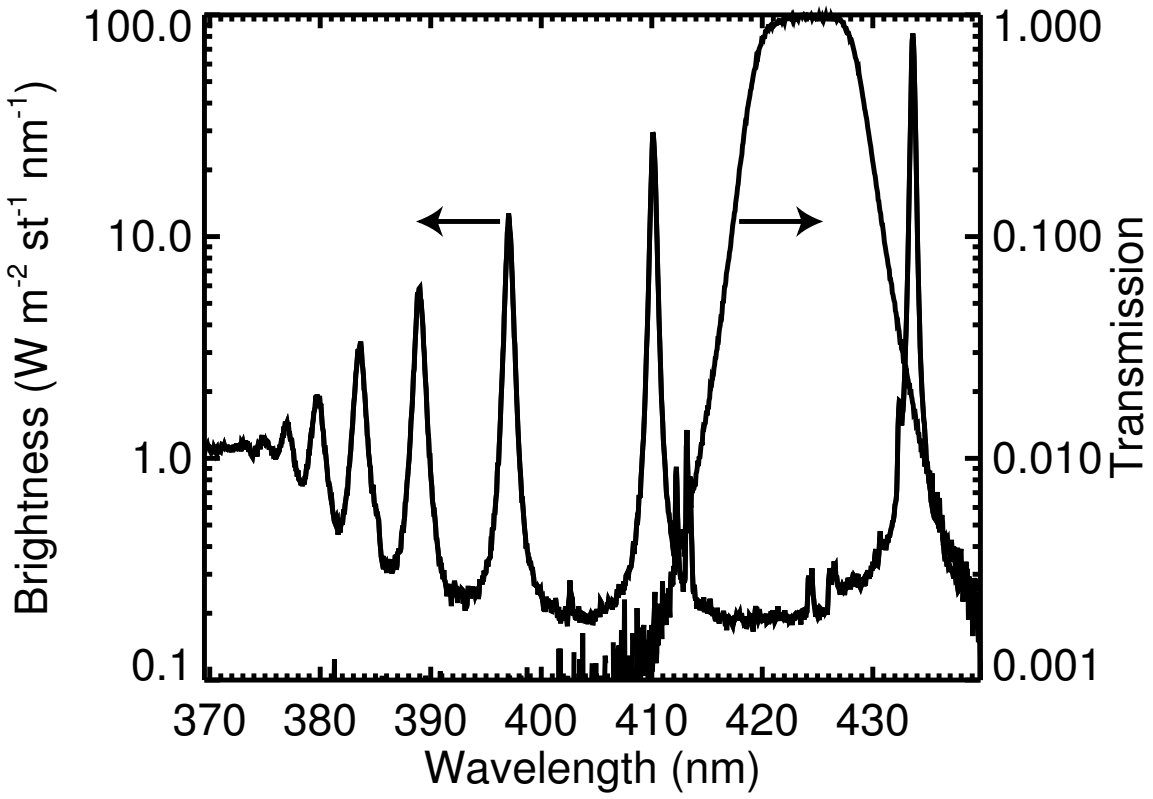


Figure 4-38: Plot of an experimental recombination spectrum with the continuum filter function overplotted. (Note the vertical scale is logarithmic)

the calibration is not for a single spectral line but for continuum emission passed by the filter. The filter for the continuum emission camera is a bandpass filter centered at 425 nm with a bandpass of 10 nm. There are no significant lines between 420 nm and 430 nm making it adequate for a measure of the continuum level. Since the filter is not a square function there is some $D_\gamma$ emission that is not entirely filtered out and can contribute up to 25% of the recorded signal. Figure 4-38 shows the continuum filter with a typical experimental recombination spectrum.

**Results**

Using the technique mentioned above, the $D_\gamma$ and continuum emissivity profiles were reconstructed for several plasma discharges where the inner and outer divertor regions were detached. Figure 4-39 and figure 4-40 show the $D_\gamma$ and continuum emissivity profiles from a typical detached discharge. It should be noted that the two profiles

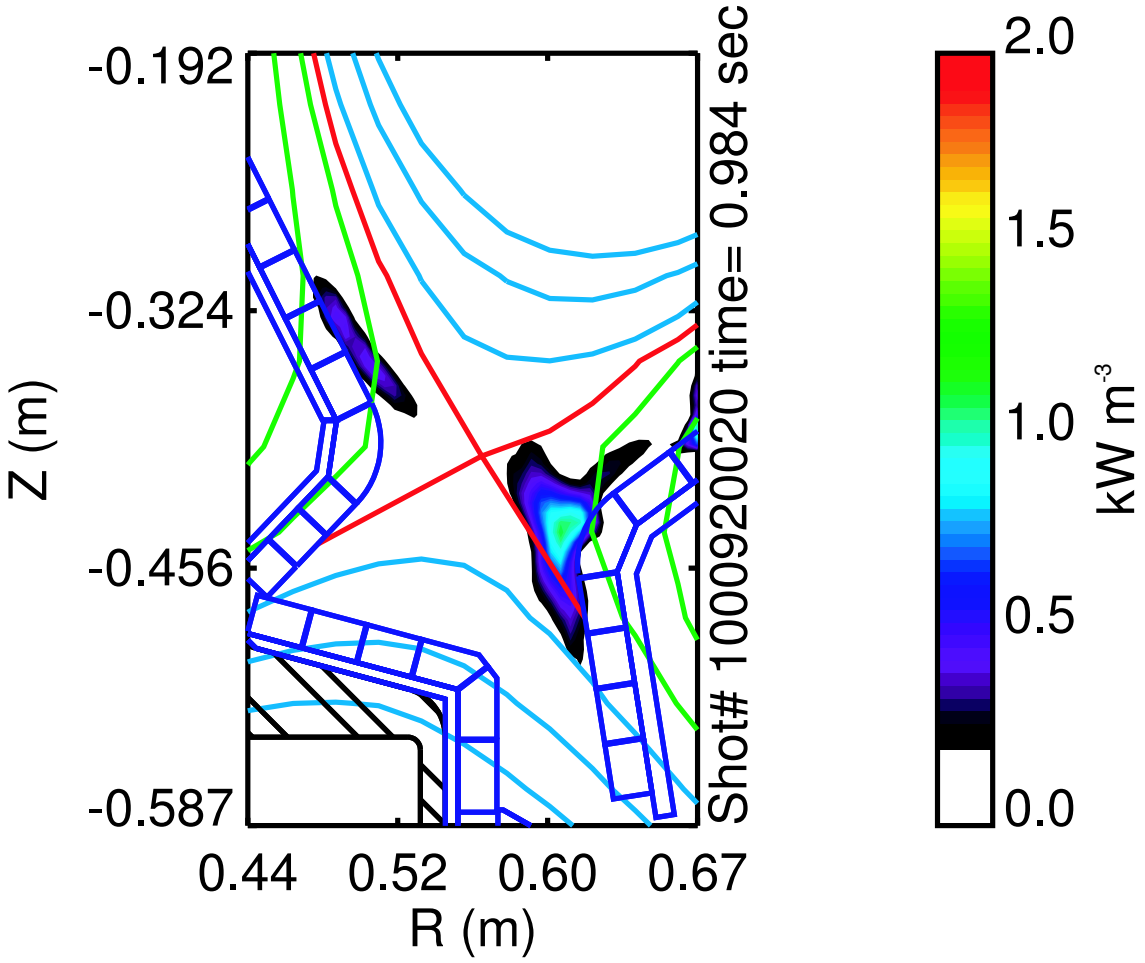


Figure 4-39: 2-D profile of the $D_\gamma$ emissivity during detached divertor operation.

are of the same order in emissivity. Using the curve in figure 4-37, when the $D_\gamma$ and continuum emissivities are of the same order the temperature is at least $\sim$ 2 eV, which is more than double the temperature measured using the high-$n$ Saha distribution technique. Also using the curve in figure 4-37 a temperature profile can be determined. Figure 4-41 shows the temperature profile using the ratio of figures 4-39 and 4-40 and the curve from figure 4-37. As is seen from figure 4-41 the temperatures all range between 4 and 40 eV. Although the distribution of the temperatures is what is expected (i.e., hotter towards the main plasma), the absolute values are well above those measured by any other method and well above the temperatures for which there would be a significant amount of atomic deuterium emitting $D_\gamma$ radiation.

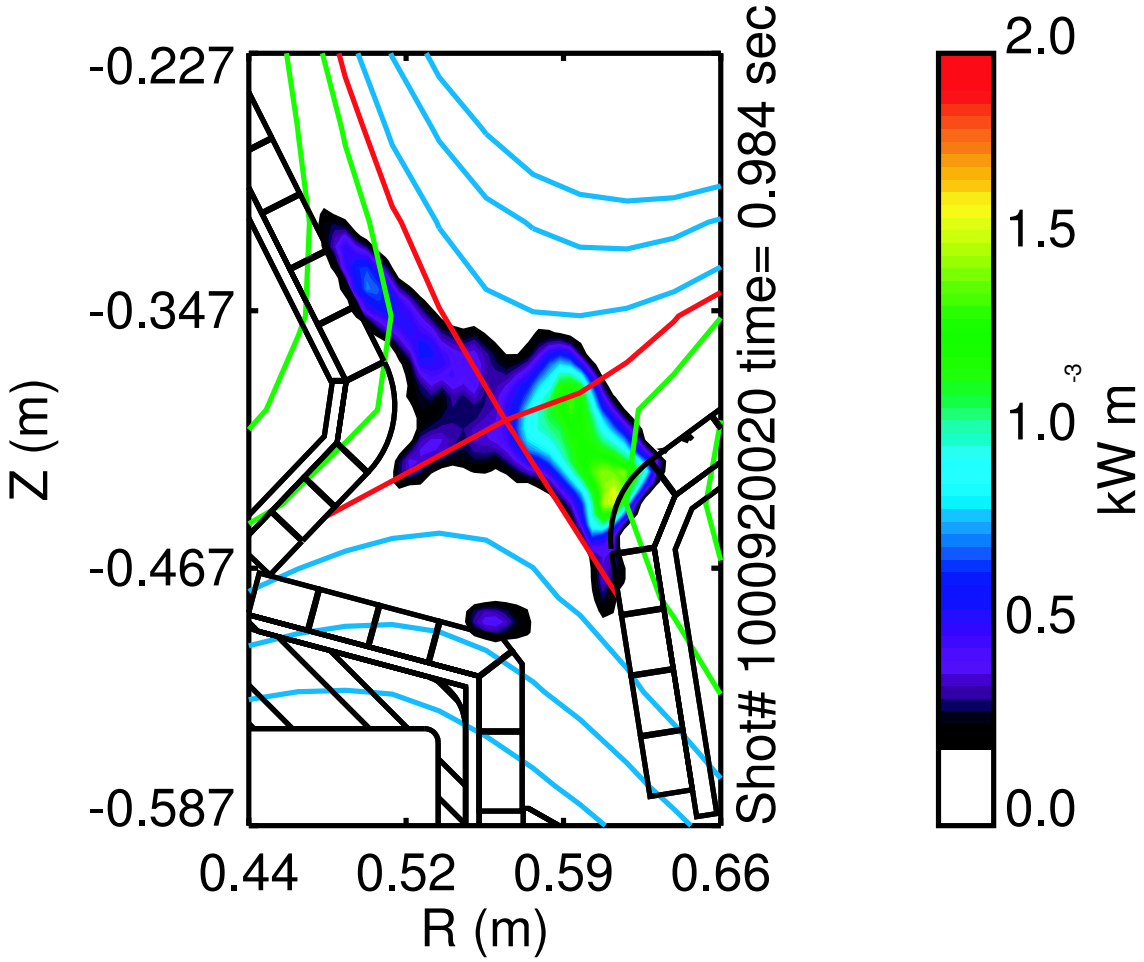


Figure 4-40: 2-D profile of the continuum (420→430 nm) emissivity during detached divertor operation.

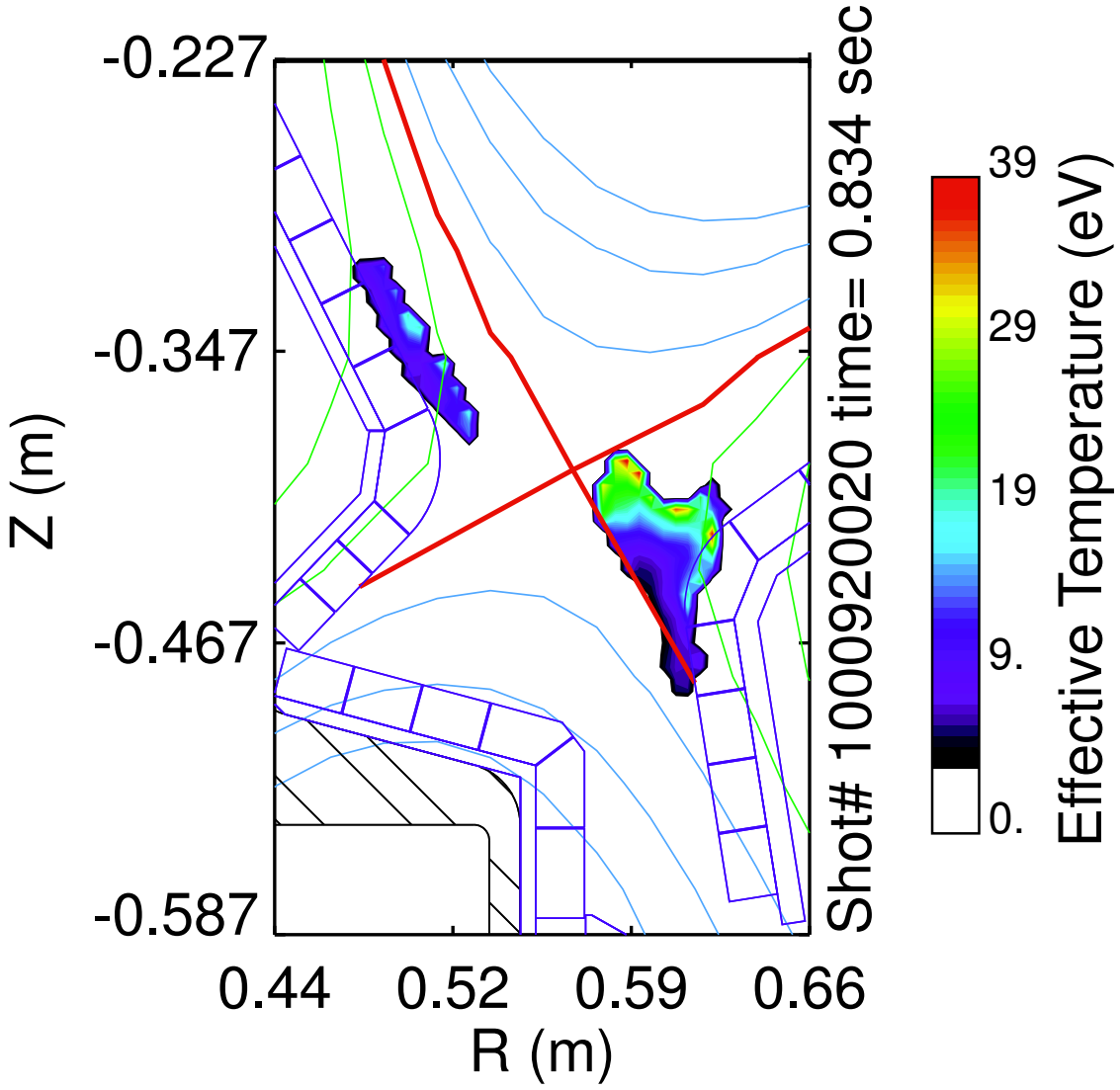


Figure 4-41: 2-D temperature profile of the divertor using the ratio of the $D_\gamma$ to continuum (420→430 nm) emissivities, assuming electron-ion bremsstrahlung and radiative recombination as the sole source of continuum.

**Discussion**

Since the temperature measurements are in disagreement with several other methods for measuring the electron temperature, the assumption that the continuum source is due to electron-ion bremsstrahlung and radiative recombination must be invalid. Several plasma and atomic sources of continuum, beyond the electron-ion bremsstrahlung and radiative recombination, have been considered:

1. electron - electron bremsstrahlung,

2. electron - atom bremsstrahlung,

3. $H^-$ attachment,

$$e^- \ + \ \mathrm{H} \ \rightarrow \ \mathrm{H}^- \ + \ h\nu, \tag{4.41}$$

   and

4. two ion - atom reactions.

$$\mathrm{H}^+ \ + \ \mathrm{H} \ \rightarrow \ \mathrm{H}^+ \ + \ \mathrm{H} \ + \ h\nu \tag{4.42}$$

$$\mathrm{H}^+ \ + \ \mathrm{H} \ \rightarrow \ \mathrm{H}_2^+ \ + \ h\nu \tag{4.43}$$

The electron - electron bremsstrahlung can be immediately dismissed as contributing significantly to the continuum level, because in the non-relativistic case the electron - electron bremsstrahlung is a factor of $\frac{2}{5}\frac{T_e}{m_e c^2}$ below the electron - ion bremsstrahlung continuum level.[4] The electron - atom bremsstrahlung can be calculated from Kirchhoff's Law using the inverse electron - atom bremsstrahlung absorption coefficients obtained from Table 1 in reference [55],

$$j_{\mathrm{aeb}}\left(n_o, n_e, T_e, \lambda\right) = \frac{2\pi h c^2}{\lambda^5} \frac{1}{e^{\frac{hc}{\lambda T_e}} - 1} \frac{\kappa_o}{n_o n_e T_e}, \tag{4.44}$$

where $j$ is in units of power per volume per wavelength, $\kappa_o$ is the tabulated value from Table 1 of reference [4], and all other parameters have their usual definitions. The

continuum due to $H^-$ attachment can be calculated by using the tabulated bound-free cross sections from reference [10] and the Milne relation, [50]

$$\frac{\sigma_{bf}}{\sigma_{fb}} = \frac{m^2 c^2 v^2}{\nu^2 h^2} \frac{g_e g_+}{2 g_n}, \tag{4.45}$$

where $\sigma_{bf}$ and $\sigma_{fb}$ are the bound-free and free-bound cross-sections, $m$ is the mass of the electron, $v$ is the velocity of the electron, and $g_e$, $g_+$, and $g_n$ are the statistical weight factors for the electron, the most positively charged state and the next charged state respectively,

$$j_{\mathrm{H}^-}\left(n_o, n_e, T_e, \lambda\right) = \frac{\left(hc\right)^4 c^2}{\left(m_e c^2\right)^2} \frac{g_{\mathrm{H}^-}}{g_e g_{\mathrm{H}}} n_e n_o \frac{\sigma_{\mathrm{bf}} f\left(v\right)}{\lambda^5 \left(\frac{hc}{\lambda} - \chi_{\mathrm{H}^-}\right)}, \tag{4.46}$$

where $g$ is the statistical weight factors for the electron, hydrogen atom and negative hydrogen ion, $\chi_{\mathrm{H}^-}$ is the ionization potential of the negative hydrogen ion (0.75 eV), $f\left(v\right)$ is a Maxwellian distribution of the electrons with temperature $T_e$,

$$f\left(v\right) = \frac{4\pi}{c} \left(\frac{m_e c^2}{2\pi T_e}\right)^{3/2} \frac{v^2}{c^2} \exp\left[-\frac{m_e c^2}{2T_e} \frac{v^2}{c^2}\right], \tag{4.47}$$

where the relation between electron velocity and wavelength is given by

$$\frac{hc}{\lambda} = \frac{1}{2} m_e v^2 + \chi_{\mathrm{H}^-}, \tag{4.48}$$

and $\sigma_{\mathrm{bf}}$ is the cross section tabulated in reference [10]. The last atomic continuum sources considered are the ion-atom interactions given by Eqns. 4.42 and 4.43. Reference [46] discusses the general derivation of the emission due to the ion - atom collisions and equation 3a in reference [45] gives the explicit function for this emission,

$$j_{\mathrm{iac}} = \frac{8\pi^3}{3} \frac{a_{\mathrm{O}}^3}{h\left(hc\right)^2 m_e c^2} n_{\mathrm{H}} n_i \left(\frac{hc}{\lambda}\right)^5 R_\omega^4 \exp\left[-\frac{U_u\left(R_\omega\right)}{T_i}\right], \tag{4.49}$$

where $R_\omega$ is the internuclear distance given by

$$\frac{hc}{\lambda} = U_u\left(R_\omega\right) - U_g\left(R_\omega\right), \tag{4.50}$$

$U_u$ is the upper state energy, $U_g$ is the lower state energy, and all other terms have their usual meaning. In equations 4.49 and 4.50 the potentials were given by the tabulated values in reference [3]. Figure 4-42 shows the potentials used in the calculation of the ion - atom continuum. The continuum contributions (2-4) as well as the electron - ion bremsstrahlung and the radiative recombination contribution have been calculated using the numerical code CRAMD (Collisional Radiative Atomic Molecular Data).[49, 48] CRAMD is a quasi-stationary, quasi-homogeneous collisional-radiative model of the atomic and molecular interactions with the background plasma. This treatment is more complete than simply using equations 4.44, 4.46, and 4.49 directly, because it includes interactions between the various species. Therefore, the continuum levels used in the following discussion are obtained from the CRAMD code.

Figure 4-43 shows the estimated contribution to the continuum due to the different plasma and atomic continuum sources. The spectrum is from a visible spectrometer viewing the divertor during discharge when the outer divertor region is deeply detached (see figure 4-40). The electron temperature and density measurements, using the ratio of the intensity of the high-$n$ Balmer lines and the Stark broadening of the same lines, yields $T_e = 1.3$ eV and $n_e = 1.26 \times 10^{21}$ m$^{-3}$. Using this electron temperature and density, setting the atomic density equal to the electron density (if anything an overestimate of the atomic density [56]), and assuming the length of the viewing chord through the emission is 5 cm (estimated from figure 4-40) the contributions from all the above processes were calculated and summarized in figure 4-43. This clearly shows that the atomic density, which is the only free parameter, must be two orders of magnitude above the electron density in order for the atomic contributions to the continuum make up the difference between the calculated plasma contributions and the measured continuum. An atomic density that is a factor of 100 above the electron density is a high value when compared to recent neutral and

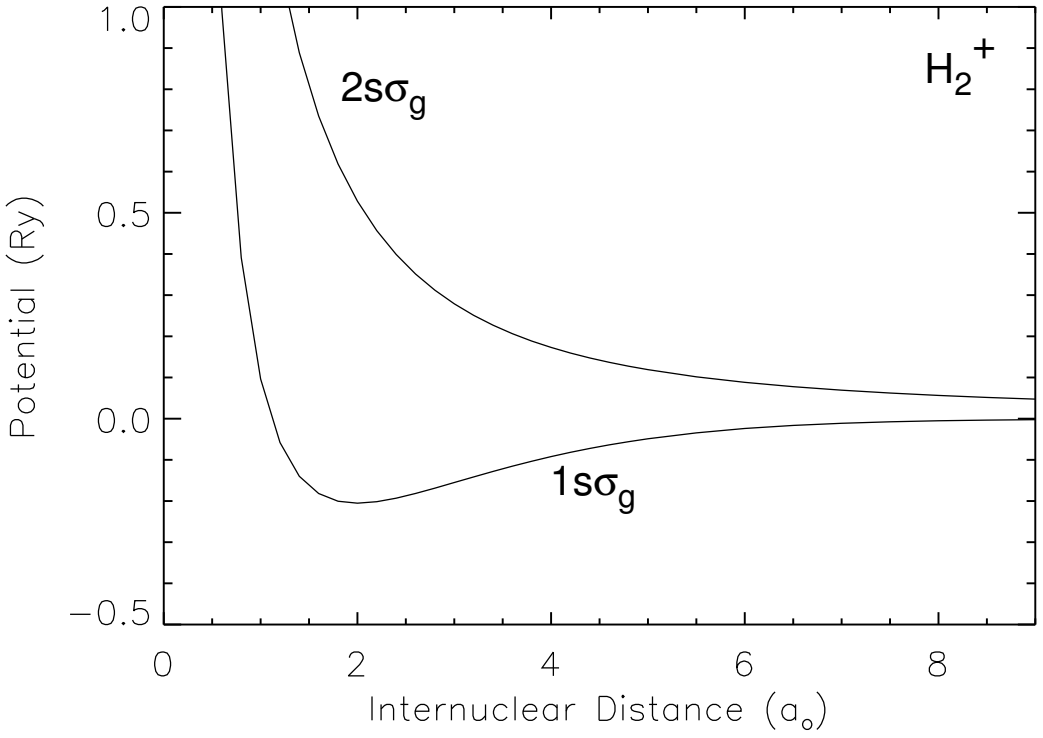


Figure 4-42: Plot of the potentials of the $1s\sigma_g$ state (lower curve) and the $2s\sigma_g$ state (upper curve) of the hydrogen molecular ion as a function of internuclear distance obtained from tabulated values in reference [3].

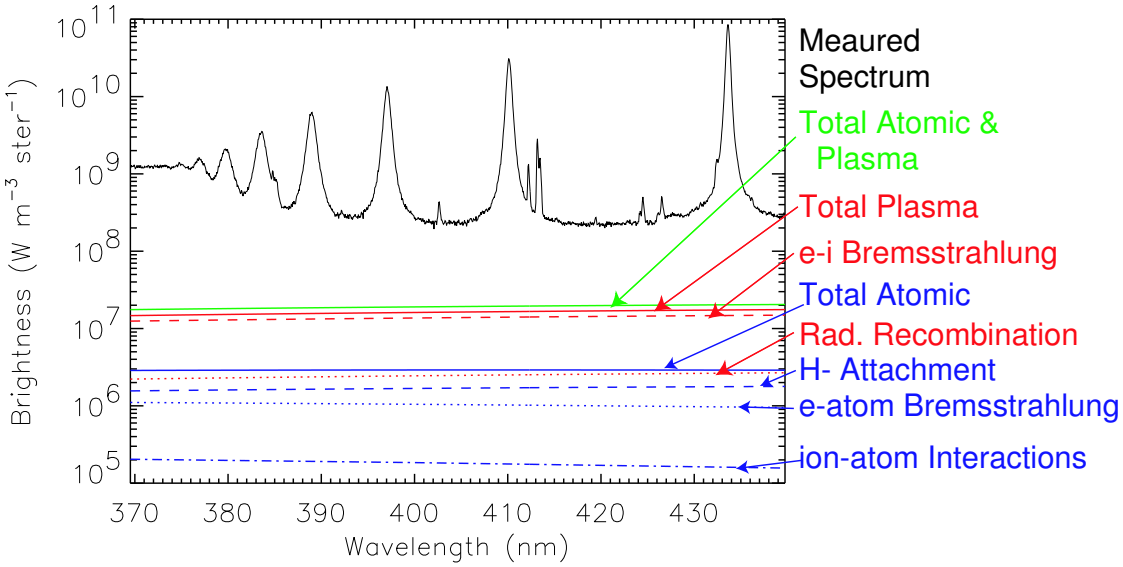


Figure 4-43: Plot of a sample measured recombination spectrum compared to expected plasma and atomic continuum. The electron temperature and density are calculated from the spectrum to be 1.3 eV and $1.26 \times 10^{21}$ m$^{-3}$. Overplotted is the electron-ion bremsstrahlung (- -), the radiative recombination ($\cdots$), and the total plasma contribution (–) to the continuum. Also plotted is the contribution due to $H^-$ attachment (- -), electron-atom bremsstrahlung ($\cdots$), ion-atom interactions ($\cdot$ -), and the total atomic continuum contribution (–) assuming equal electron and atom densities. Finally, the sum of the plasma and atomic continuum brightnesses are also overplotted (–).

plasma modelling results [56] and therefore it is expected that atomic contributions to the continuum level cannot explain the measured continuum.

Since the plasma and atomic continuum sources cannot account for the observed continuum, yet another mechanism has been investigated. A possible source of continuum could be due to radiative detachment of the $D_2$ molecule. When the $D_2$ molecule is in the $a^3\Sigma_g^+$ electronic state it will decay to the $b^3\Sigma_u^+$, which is an unbound state. This decay into the unbound state yields a continuum spectrum. Figure 4-44 shows the lowest singlet bound molecular state ($X^1\Sigma_g^+$), the lowest triplet bound molecular state ($a^3\Sigma_g^+$), and the lowest triplet unbound molecular state potential energies. The investigation into the continuum caused by the radiative detachment was originally published by Winans and Stueckelberg[63] and then investigated further by James and Coolidge[26, 9, 8] and more recently by Doyle[11] with calculations carried out

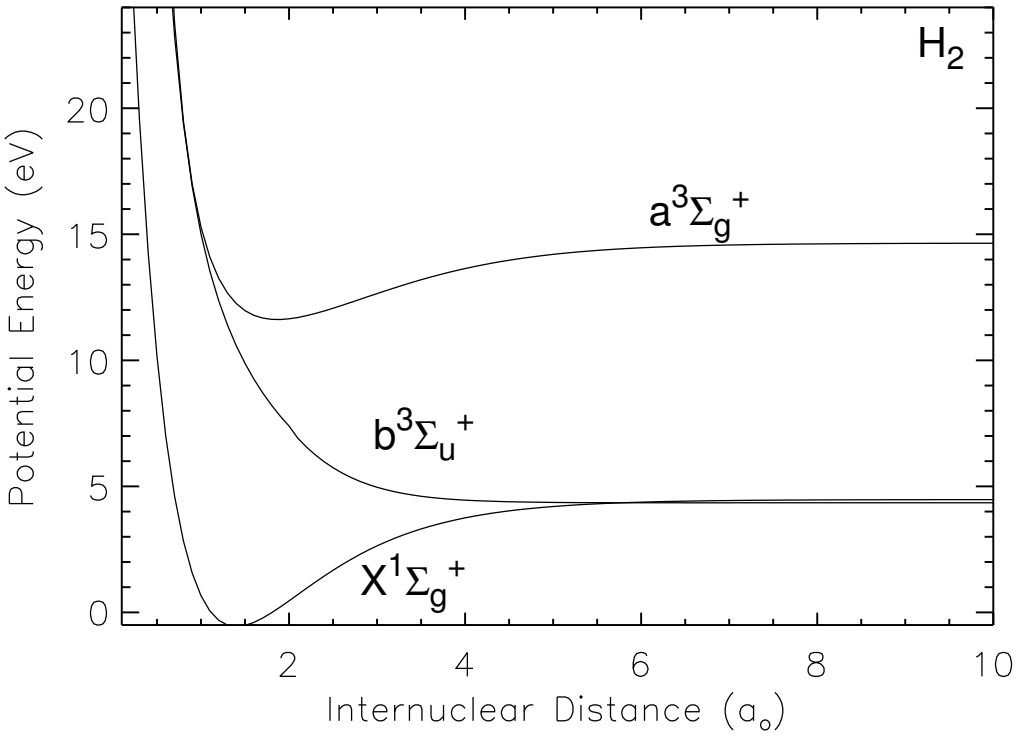


Figure 4-44: Plot of the potential energy of the $X^1\Sigma_g^+$, $a^3\Sigma_g^+$, and $b^3\Sigma_u^+$ $H_2$ molecular states.

to a high number of vibrational levels and accuracy by Fantz[13]. Using the tables published in reference [13] the continuum from the $D_2$ molecule can be calculated as a function of the number density of $D_2$ molecules in the $a^3\Sigma_g^+$ state and the vibrational temperature of those $D_2$ molecules. Since the vibrational temperature of the molecules is unknown in the following analysis it is assumed that the vibrational temperature is equal to the electron temperature. It is expected that this vibrational temperature is too high, but by using this temperature, the estimates yield a minimum density required to for the molecules to account for the continuum level measured.

With an assumption of $n_{H_2}(a^3\Sigma_g^+) = 2{\times}10^{-5}\ n_e$, nearly all of the continuum can be accounted for. Figure 4-45 shows the amount of continuum expected if $n_{H_2}(a^3\Sigma_g^+) = 2 \times 10^{-5}\ n_e$ for the same case as figure 4-43.

A density of $H_2$ in the $a^3\Sigma_g^+$ state that is 4 to 5 orders of magnitude below the electron density is required to explain the observed continuum. Therefore, the next

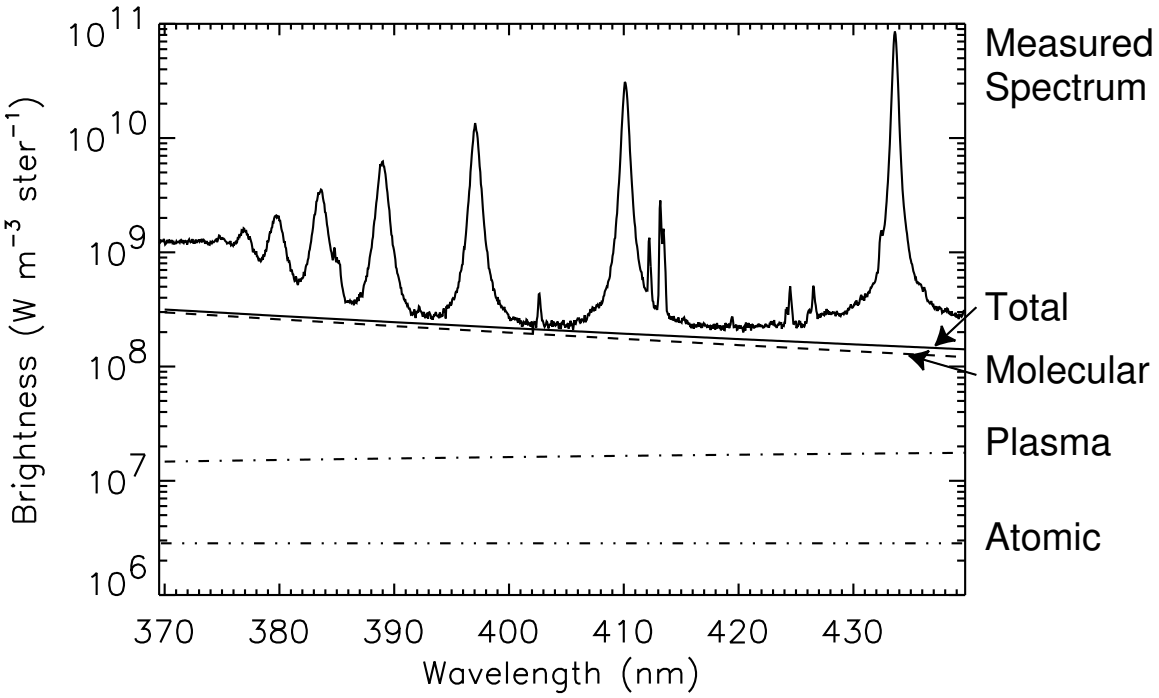


Figure 4-45: Plot of the recombining plasma from figure 4-43 with the plasma (-·-), atomic (-· · ·-), molecular (- -), and total (–) continuum levels assuming $n_e = n_o = 50000 n_{H_2}(a^3\Sigma_g^+) = 1.26 \times 10^{21}\mathrm{m}^{-3}$ and $T_e = T_{vib} = 1.3$ eV.

step is to determine the population mechanism for this state and determine whether the required molecular densities are reasonable. There are two main methods of populating the $\mathrm{a}^3\Sigma_g^+$ state, either through excitation from the $H_2$ ground state ($\mathrm{X}^1\Sigma_g^+$) or through recombination into the $\mathrm{a}^3\Sigma_g^+$ or higher states with a cascade down through the $\mathrm{a}^3\Sigma_g^+$ state. The first method to be considered is the excitation method. This is the easiest to consider since there is a published [28] reaction rate for the following reaction,

$$\mathrm{e}^- + \mathrm{H}_2\left(\mathrm{X}^1\Sigma_g^+\right) \rightarrow \mathrm{e}^- + \mathrm{H}_2 \left( \begin{array}{c} \mathrm{b}^3\Sigma_u^+ \\ \mathrm{a}^3\Sigma_g^+ \\ \mathrm{c}^3\Pi_u \end{array} \right) \rightarrow \mathrm{e}^- + \mathrm{H}(1s) + \mathrm{H}(1s), \tag{4.51}$$

shown in figure 4-46. By assuming the reaction rate for equation 4.51 is all for population of the $\mathrm{a}^3\Sigma_g^+$ state, it is possible to calculate a lower bound of the $H_2$ density. Equating the excitation rate with the radiative dissociation rate and solving

for the $H_2$ density yields

$$n_{H_2} = \frac{n_{H_2\left(a^3\Sigma_g^+\right)}}{n_e} \frac{A_{H_2\left(a^3\Sigma_g^+\right)}}{\langle \sigma v \rangle}. \tag{4.52}$$

Since $n_{H_2\left(a^3\Sigma_g^+\right)}/n_e \approx 2 \times 10^{-5}$, from reference [13] $A_{H_2\left(a^3\Sigma_g^+\right)} \approx 10^8$ s$^{-1}$, and from reference [28] $\langle \sigma v \rangle \approx 3.25 \times 10^{-18}$ m$^3$ s$^{-1}$ at $T_e = 1.3$ eV, the lower bound of the molecular deuterium density is approximately $6.2 \times 10^{20}$ m$^{-3}$. This density is over 60% of the electron density, which is much higher than expected from modelling [56]. The other population method to be considered is by recombinations into the $a^3\Sigma_g^+$ and higher states. This is analogous to the atomic system where the deuteron will recombine with electrons into the various energy levels and then radiatively cascade down to ground state. In the molecular case the $H_2^+$ molecule recombines with an electron which eventually decays into either the ground state ($X^1\Sigma_g^+$ or the $b^3\Sigma_u^+$ repulsive state. Reaction rates on the total recombination process for the molecular hydrogen ion are not known. I have chosen therefore to use the *atomic* reaction rates to estimate the total recombination rate. The recombination rates used are obtained from the code "collrad" which is based on the code described by Weisheit[61] using the cross section data from the Janev-Smith database[27]. These are the same rates used in the DEGAS2 monte carlo neutral modelling code[57], and include both the radiative recombination and the three-body recombination channels. Figure 4-47 shows the total recombination rate at three different electron densities as a function of electron temperature. The three-body recombination channel is dominant in the high density, low temperature plasmas discussed in this section. Therefore by assuming that ~60% of the recombinations populate the $a^3\Sigma_g^+$ (which then radiatively dissociates via continuum emission to the $b^3\Sigma_u^+$ state), the $n_{H_2^+}$ density required for a given $a^3\Sigma_g^+$ population density can be estimated, since

$$0.6 n_{H_2^+} n_e RR = n_{H_2(a^3\Sigma_g^+)} A_{H_2(a^3\Sigma_g^+)} \tag{4.53}$$

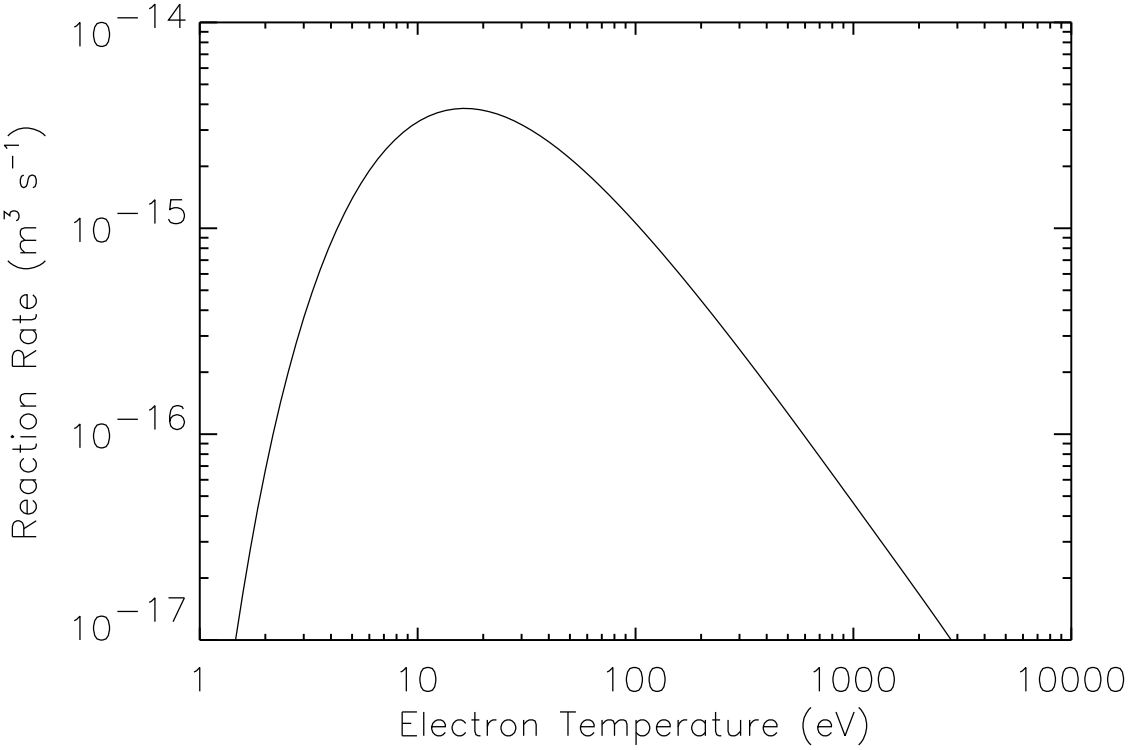


Figure 4-46: Plot of the reaction rate of equation 4.51 as a function of electron temperature.

where $RR$ is the total atomic specific recombination rate for a given electron density and temperature. Using the previously mentioned values for $n_{H_2(a^3\Sigma_g^+)}/n_e$, and $A_{H_2(a^3\Sigma_g^+)}$, and the value of $RR$ at $n_e = 10^{21}$ m$^{-3}$ and $T_e = 1.3$ eV ($2.3 \times 10^{-18}$ m$^3$ s$^{-1}$) yields a density of $H_2^+$ of $1.4 \times 10^{21}$ m$^{-3}$. This density is also well above the expected values from recent modelling results [56]. These modelling result give maximum values for the $H_2$ density of $\sim 10^{19}$ m$^{-3}$ and $H_2^+$ densities of $\sim 10^{17}$ m$^{-3}$, which are several orders of magnitude below densities required by this analysis. Therefore, although the molecular continuum could explain the level of continuum seen in the divertor during detached divertor operation an adequate mechanism has not yet been found to explain the population density of molecules in the $a^3\Sigma_g^+$ state consistent with recent modelling efforts. This analysis requires $n_{H_2} = 3 \times 10^{20}$ m$^{-3}$and/or $n_{H_2^+} = 10^{21}$ m$^{-3}$ to explain the observation.

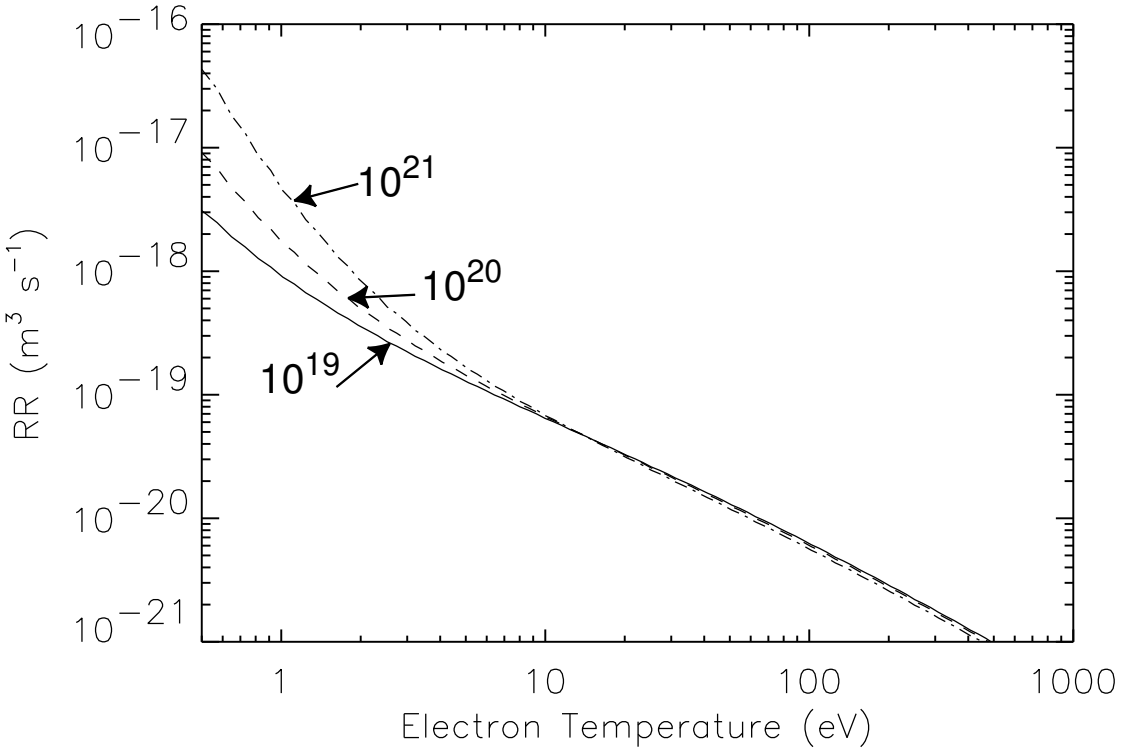


Figure 4-47: Plot of the total atomic recombination rate as a function electron temperature at three densities, $10^{19}$ $m^{-3}$ (–), $10^{20}$ $m^{-3}$ (- -), $10^{21}$ $m^{-3}$ (-·-).

| | Model | Presented Analysis |
|---|---|---|
| $n_0/n_e$ | $10^{-1}$ | $10^2$ |
| $n_{H_2}/n_e$ | $10^{-2}$ | 0.5 |
| $n_{H_2^+}/n_e$ | $10^{-4}$ | 1 |

Table 4.1: Comparison of density ratios from plasma and neutral modelling code (DEGAS) and the required density ratios from the analysis presented. The DEGAS ratios are from the detached inner divertor region.

**Conclusions**

In an attempt to generate two-dimensional electron temperature profiles in the divertor of Alcator C-Mod, two CCD cameras filtered to view different regions of the visible spectrum were recorded. Using interference filters, one of the cameras was filtered for the $n = 5 \rightarrow 2$ deuterium transition ($D_\gamma$), and the other camera was filtered to view the spectral range from 420 to 430 nm. Two dimensional profiles of the emissivity were generated using the technique described in sections 4.2 and 4.1.

Using the ratio of these emissivity profiles it should be possible to obtain electron temperature profiles using the line-to-continuum-ratio technique described in reference [18]. The temperatures obtained with this technique were consistently too high when compared to other temperature measurements in the divertor region. The failure of this technique can be attributed to "excess" continuum emission above that expected from electron-ion bremsstrahlung and radiative recombination alone.

In an attempt to explain the "excess" continuum various plasma, atomic, and molecular processes were considered. The atomic processes were found to account for the total continuum only if the atomic deuterium density was two orders of magnitude larger than the electron density in the region of emission. Molecular processes could also account for the continuum level observed, but only if the either the neutral deuterium molecule or the ionized deuterium molecule had a density on the same order as the electron density. All of the densities required to explain the continuum are larger than the densities of the respective species expected by plasma and neutral transport modeling (see table 4.1).

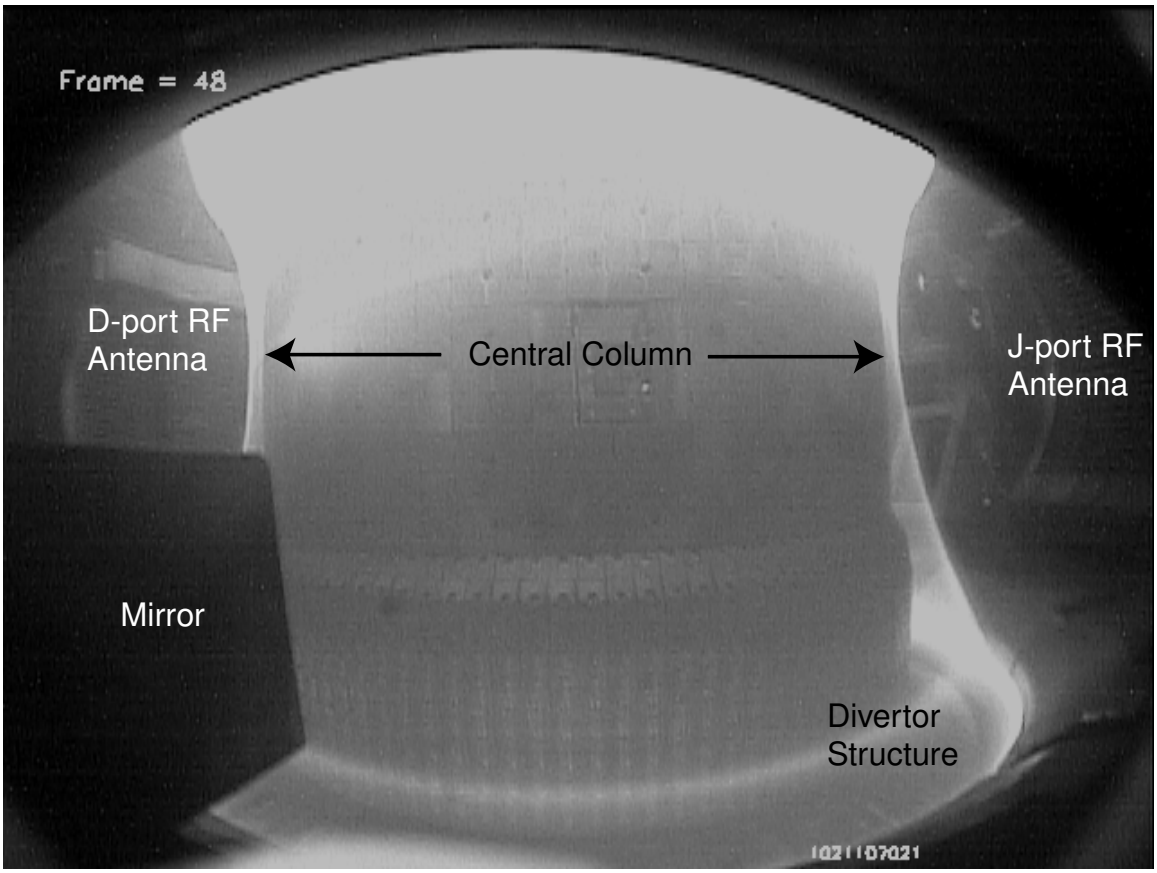


Figure 4-48: Labelled image from the "A-port" wide angle camera showing the central column, the "D-port" RF antenna structure, "J-port" RF antenna structure, the divertor structure, and a mirror in the camera's field of view.

## 4.4 Qualitative Examples

The following section presents examples of recorded images from the visible imaging system. To assist the reader as to the orientation of the images, Figure 4-48 shows an image from the "A-port" wide angle camera and figure 4-49 shows an image from the "F-port" wide angle camera (180° from "A-port") when the vessel is illuminated by a region of intense visible light from the plasma in the upper divertor of the tokamak. Important features for in the view are labelled in these figures.

Besides its usefulness in the understanding of various physical phenomena, the visible imaging system of Alcator C-Mod has significant operational benefits. The visible imaging system has been used in identifying the causes of impurity injections during the discharges, in identifying failures of invessel components, and as a general

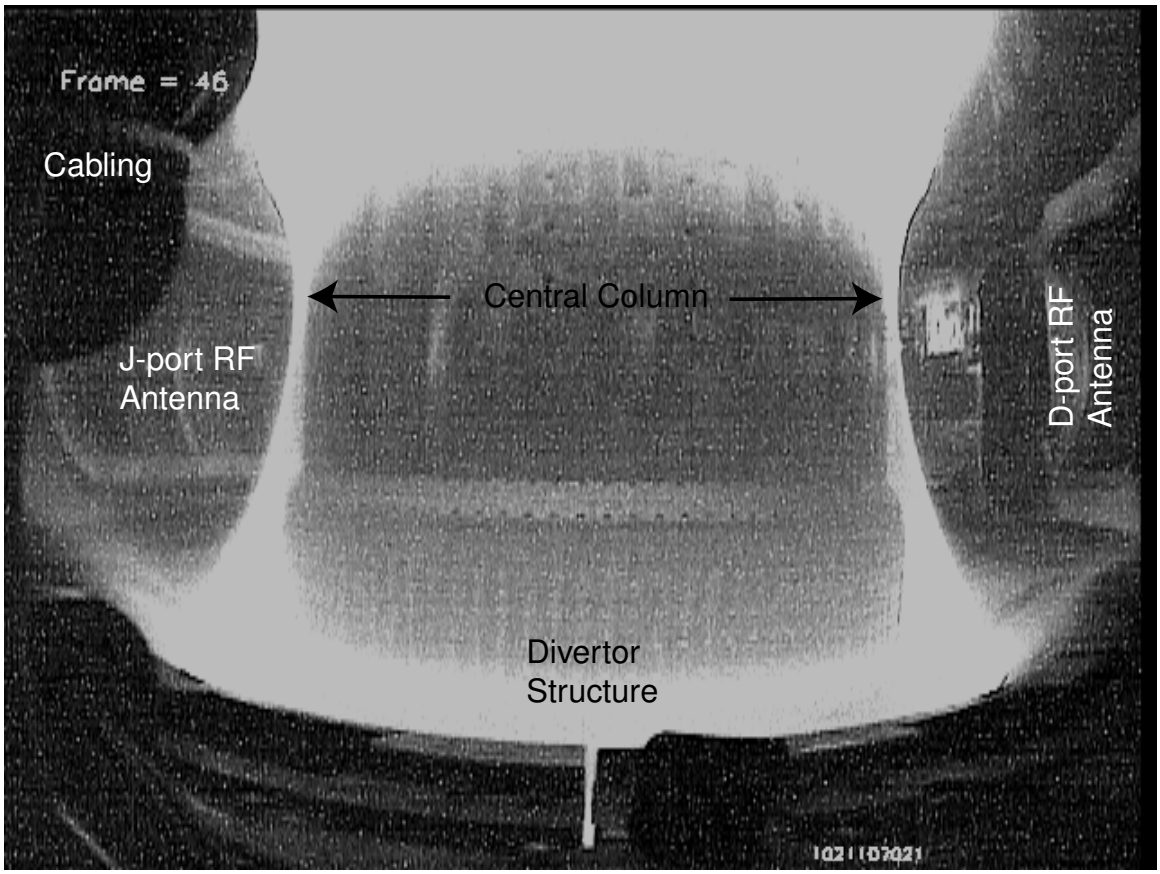


Figure 4-49: Labelled image from the "F-port" wide angle camera showing the central column, the "D-port" RF antenna structure, "J-port" RF antenna structure, and the divertor structure.

monitor of vessel and plasma conditions. In all cases mentioned above the visible imaging system was left unfiltered, recording the entire visible spectrum. The following sections give more details about the operational uses of the system.

### 4.4.1 Identifying Causes of Impurity Injection

There are three main causes of impurity injection in Alcator C-Mod. Injections have originated from either the RF antenna structure, from the Langmuir scanning probes or from the molybdenum protection tiles that line the inside of the vacuum vessel. The impurity injections from the RF antenna structures have typically originated from either the protection tiles that border the antennas or from the Faraday screens directly in-front of the antennas straps. Figure 4-50 shows an injection from the protection tiles around the 4 strap ("J-port") antenna structure and figure 4-51 shows an injection from the "J-port" Faraday screen. The content of the injections was determined by viewing the visible spectrum with a spectrometer using viewing fibers colinear to the CCD camera views. In the case of the impurities from the protection tiles it was determined that the injections were molybdenum when molybdenum tiles where installed and boron-nitride when boron-nitride tiles were installed. In the case of the Faraday screen a significant increase in the titanium emission was measured. Thus, in combination with the TV images, it was determined that the flakes of TiC coating from the Faraday screen were being injected.

The Langmuir scanning probes can be another significant source of impurity injections. There are three Langmuir scanning probes, one scanning horizontally above the midplane on outside edge, another scanning vertically from an outside divertor plate, and a third mounted to the inner wall at the midplane scanning horizontally. Two of the scanning Langmuir probes are directly in the view of the CCD cameras while the third one (outer midplane probe) is mounted directly above the viewing cameras and therefore its injections are only observed when they are bright enough to be seen in reflection off of the inner wall. The Langmuir scanning probes rarely scan into the plasma far enough to cause significant impurity injections, but when they do their injections are sometimes seen by the visible imaging system. Figures 4-

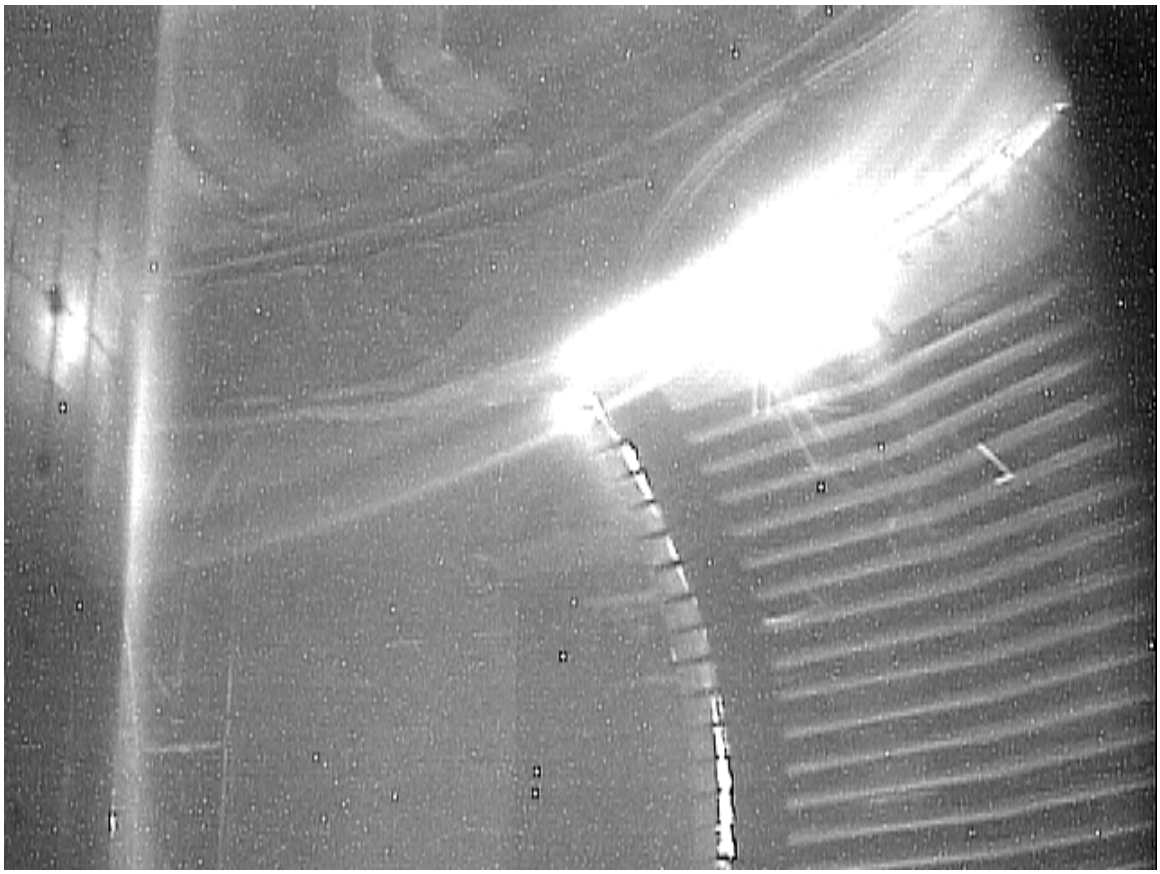

Figure 4-50: Recorded image from the visible imaging system showing an impurity injection from the RF antenna protection tiles. The central column can be seen on the left side of the view and the bars of the Faraday screen in-front of the RF antenna straps.

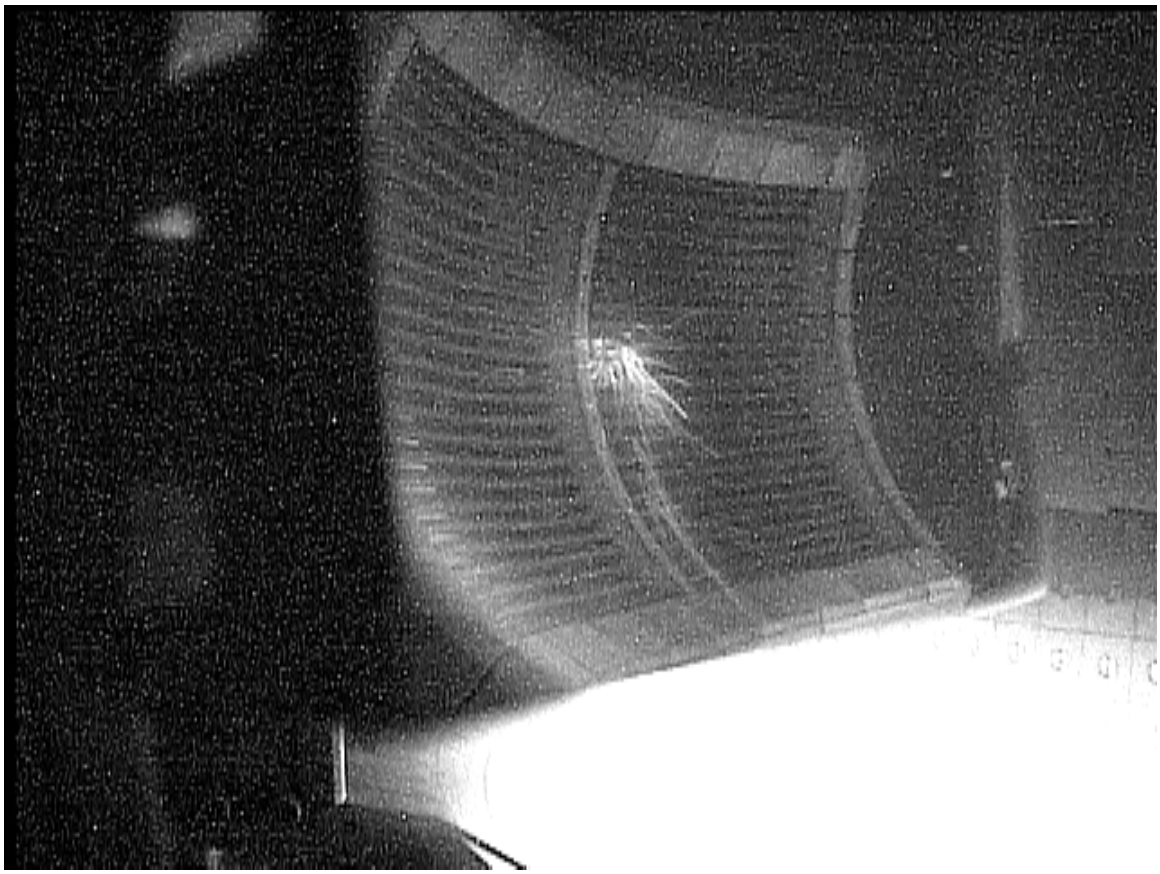

Figure 4-51: Recorded image from the visible imaging system showing an impurity injection from the RF antenna Faraday screen. The image of the RF antenna is obtained by the use of a mirror located in the center of the view.

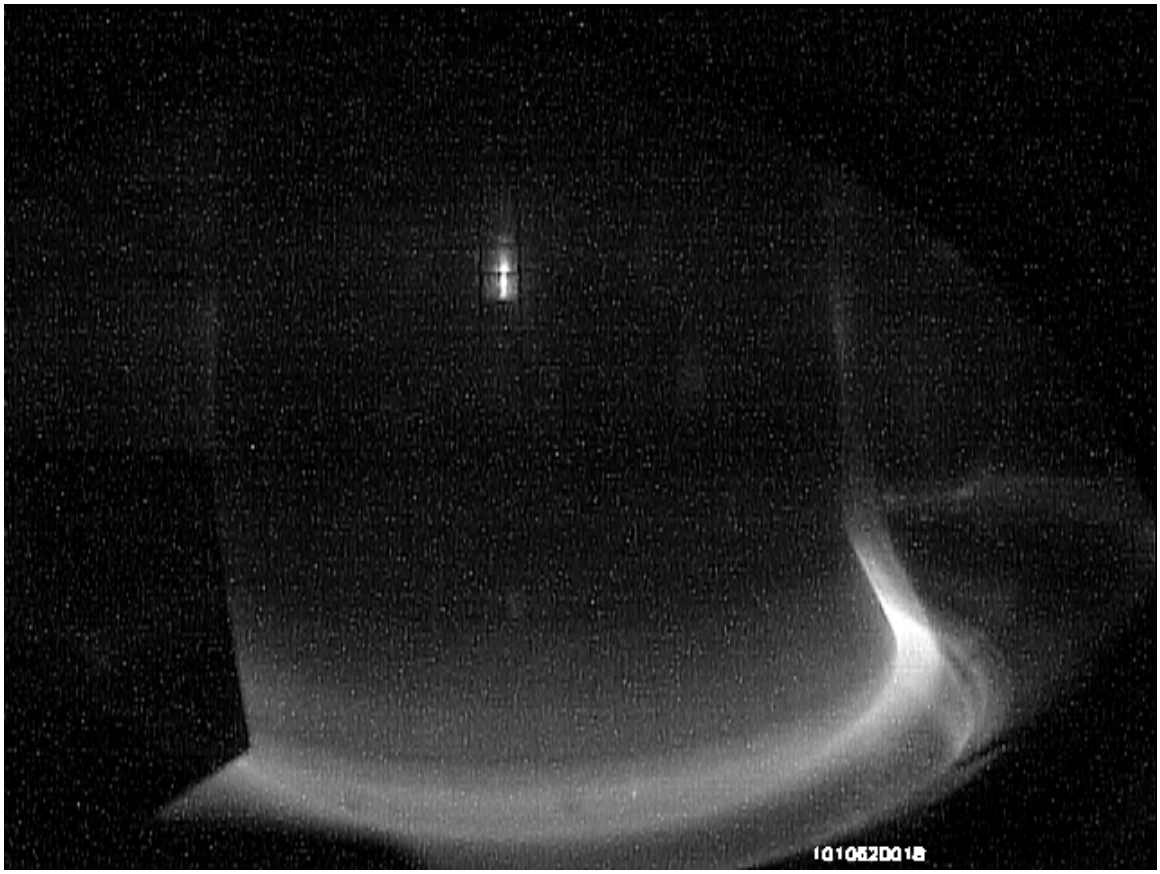


Figure 4-52: Recorded image from the visible imaging system ("A-port" wide angle) showing an impurity injection from the outer Langmuir scanning probe. Although the probe itself cannot be seen in this image, the reflection of the localized injection emission can be seen on the inner wall.

52, 4-53 and 4-54 show the outer (in reflection), divertor and inner scanning Langmuir probes injecting impurities into the plasma discharge.

The third class of injection observed by the visible imaging system are injections originating from the molybdenum protection tiles that line the inside of Alcator C-Mod. These injections often look like sparks originating from between two tiles and extending into the plasma. These injections are almost always composed of molybdenum as evidenced by the significant increase of molybdenum radiation observed by visible, VUV, and X-ray spectrometers. Figure 4-55 shows a typical injection from the molybdenum tiles.

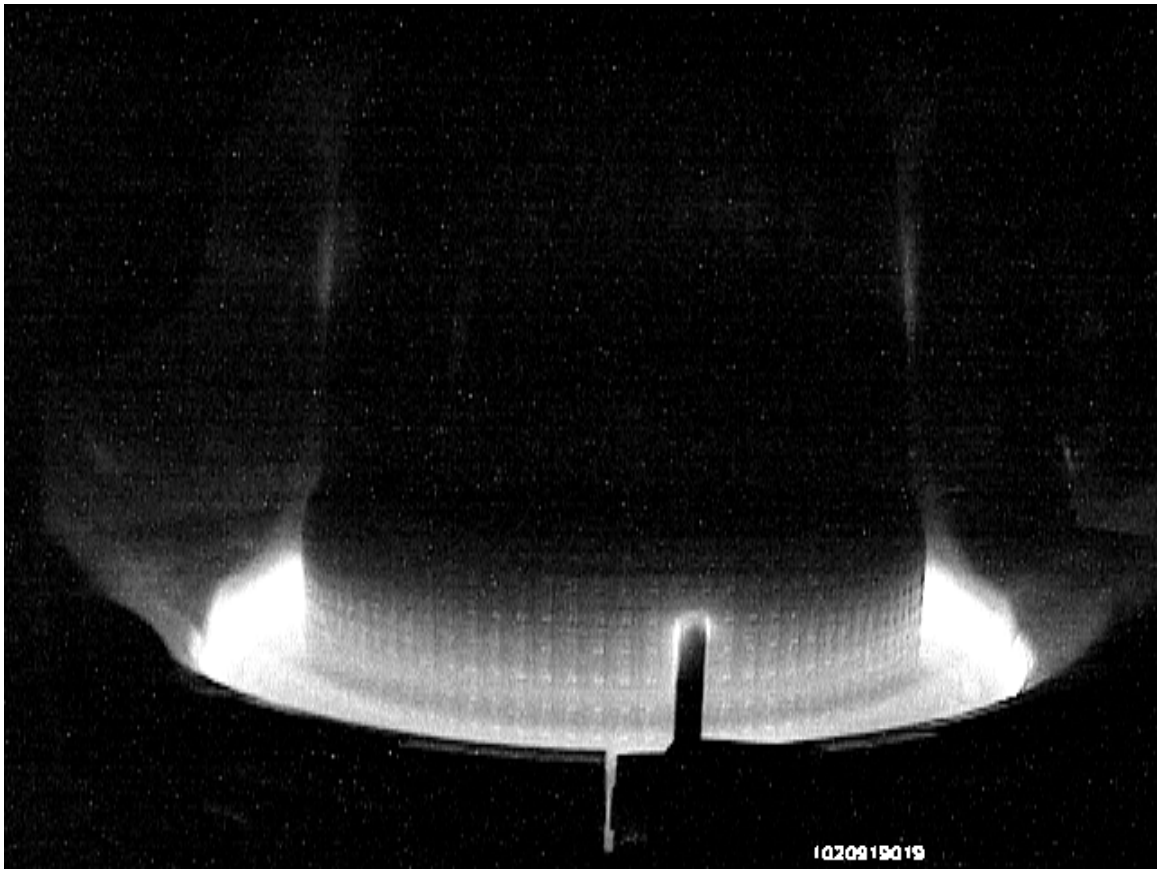


Figure 4-53: Recorded image from the visible imaging system ("F-port" wide angle) showing recycling from the divertor Langmuir scanning probe.

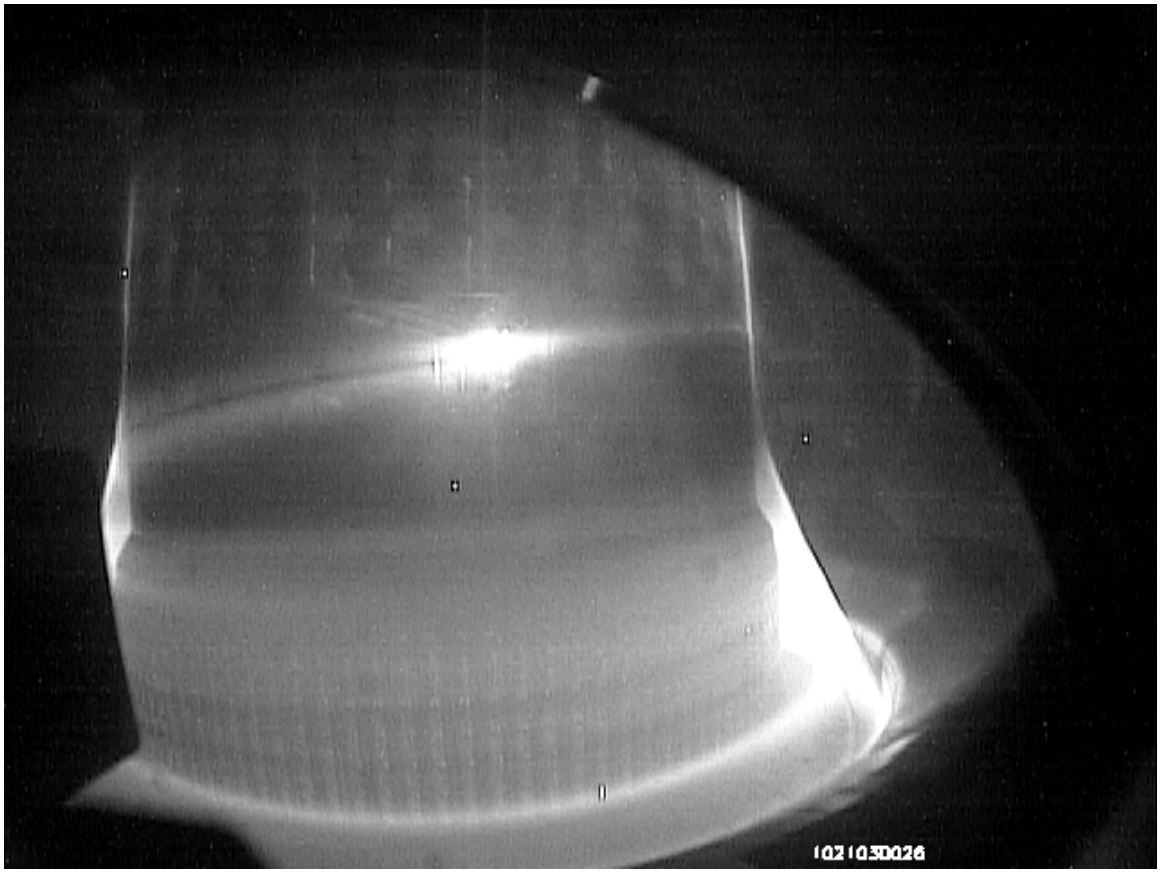


Figure 4-54: Recorded image from the visible imaging system ("A-port" wide angle) showing an impurity injection from the inner Langmuir scanning probe.

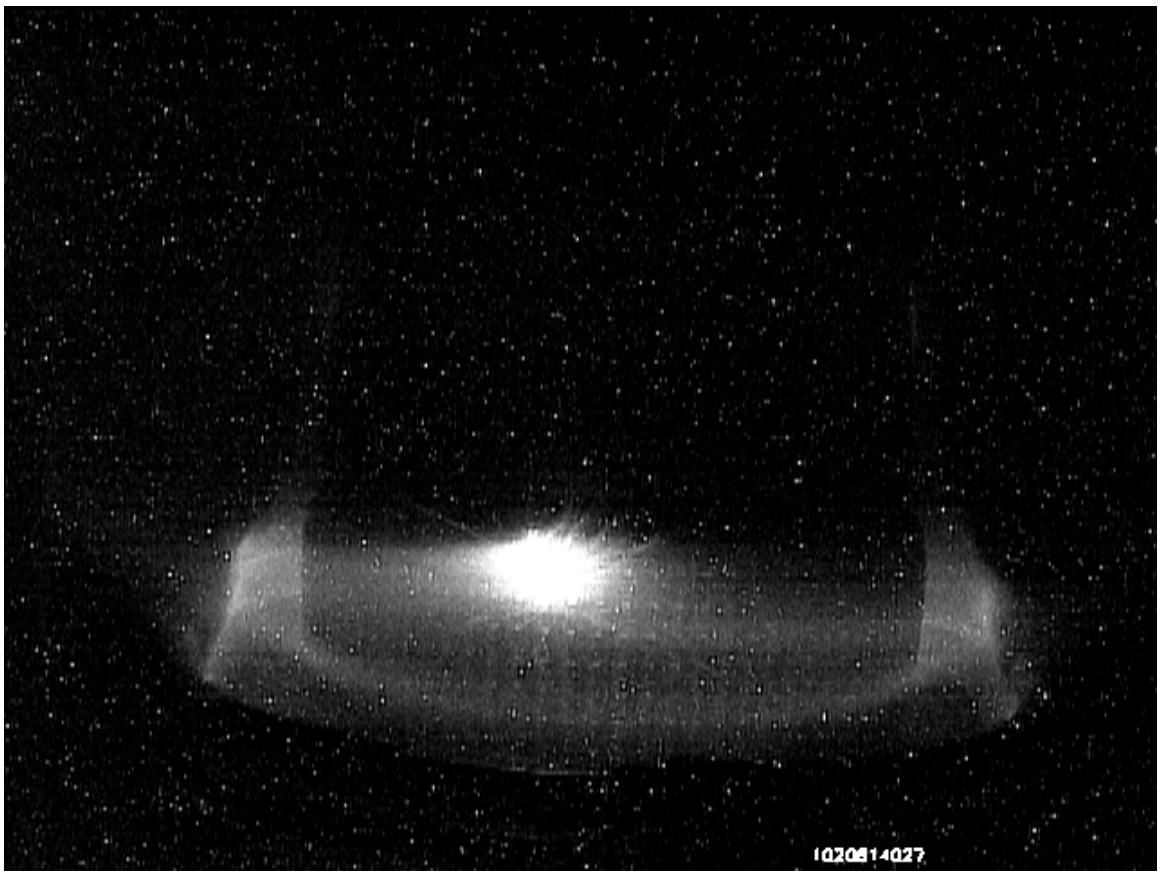


Figure 4-55: Recorded image from the visible imaging system ("F-port" wide angle) showing an impurity injection from the molybdenum tiles.

### 4.4.2 Identifying Failure of Invessel Components

The visible imaging system has been useful in identifying when certain invessel components fail. Three specific incidents are noted, the bending of a viewing dump, the complete dislocation of a viewing dump, and the breaking and falling of boron nitride protection tiles from an RF antenna structure.

The bent viewing dump can be seen in the comparison of figure 4-56, which is an image taken before the viewing dump is bent, to figure 4-57, taken after the viewing dump has bent. This viewing dump is used to reduce the reflections to fibers with a vertically downward view. The bent viewing dump would not have been noticed on the data, but would have caused erroneous interpretation of some of the line spectra obtained from this view, since the spectral line shapes would not be indicative of the view, but from the source of the reflected light.

Another invessel component failure involved a viewing dump that was attached to the outboard side of the vacuum vessel. This viewing dump was used with the visible bremsstrahlung system [44] installed on Alcator C-Mod. The viewing dump was spot welded to the inside of the stainless steel vacuum vessel. During the course of a campaign the viewing dump was dislodged from the side of the vacuum vessel and fell into the divertor. This was a serious problem since good discharges could not be achieved. The initial evidence that something was wrong was difficulty in producing non-disrupting plasmas. The imaging system identified the cause of the problems. The dislodged viewing dump was found in the images of both the divertor viewing cameras. A vacuum break was required to retrieve the broken dump. Figure 4-58 shows the final location of the viewing dump.

The final example of an invessel component failure identified by the visible imaging system is the breaking of boron nitride protection tiles from the "J-port" RF antenna structure. These tiles encircle the Faraday screen which covers the RF antenna straps and are used as an electrically insulating protective structure for the antenna. During the 2002 run campaign these tiles experienced unexpected forces from disruptions. These forces caused the tiles to break at the location where they were fastened to the

Figure 4-56: "F-port" Wide-angle view image taken before the viewing dump (in the near field) is bent. In this image the cabling on the left side of the view is clearly visible.

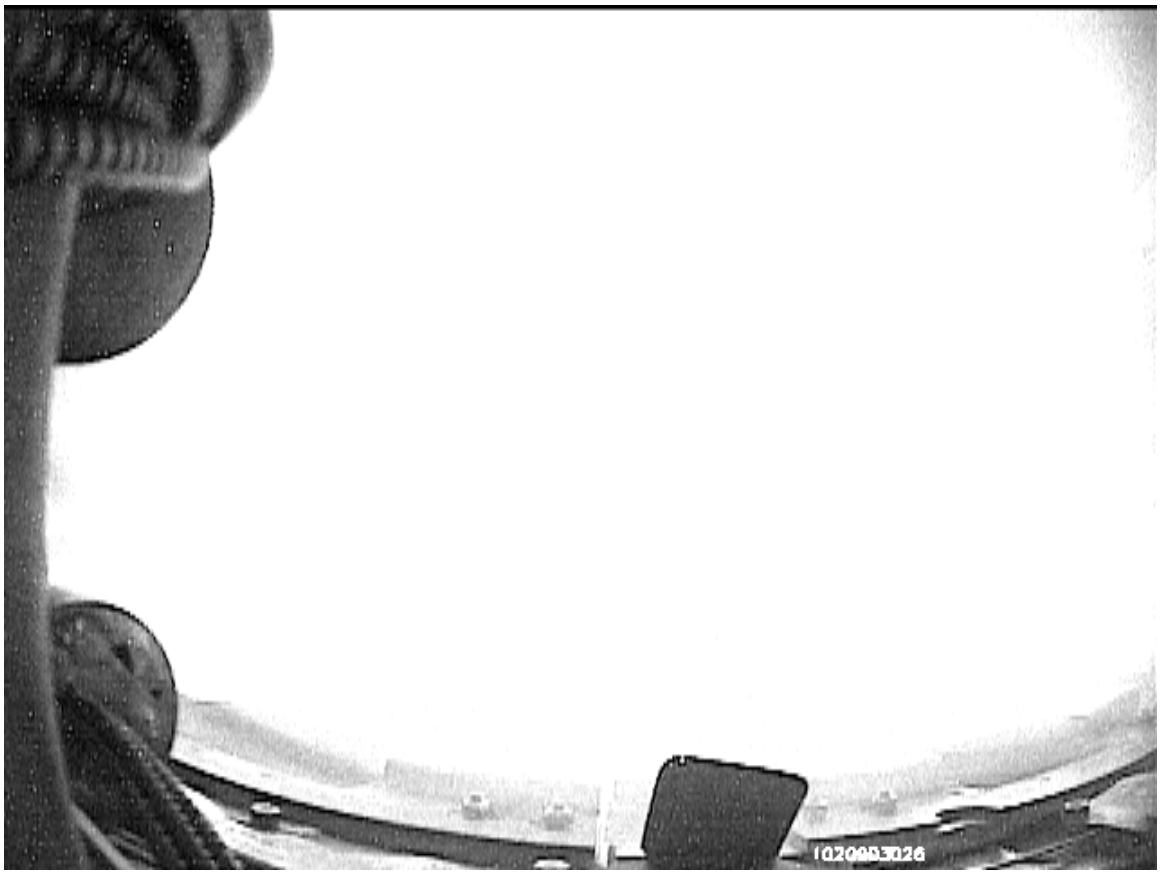

Figure 4-57: "F-port" Wide-angle view image taken after the viewing dump (in the near field) is bent.

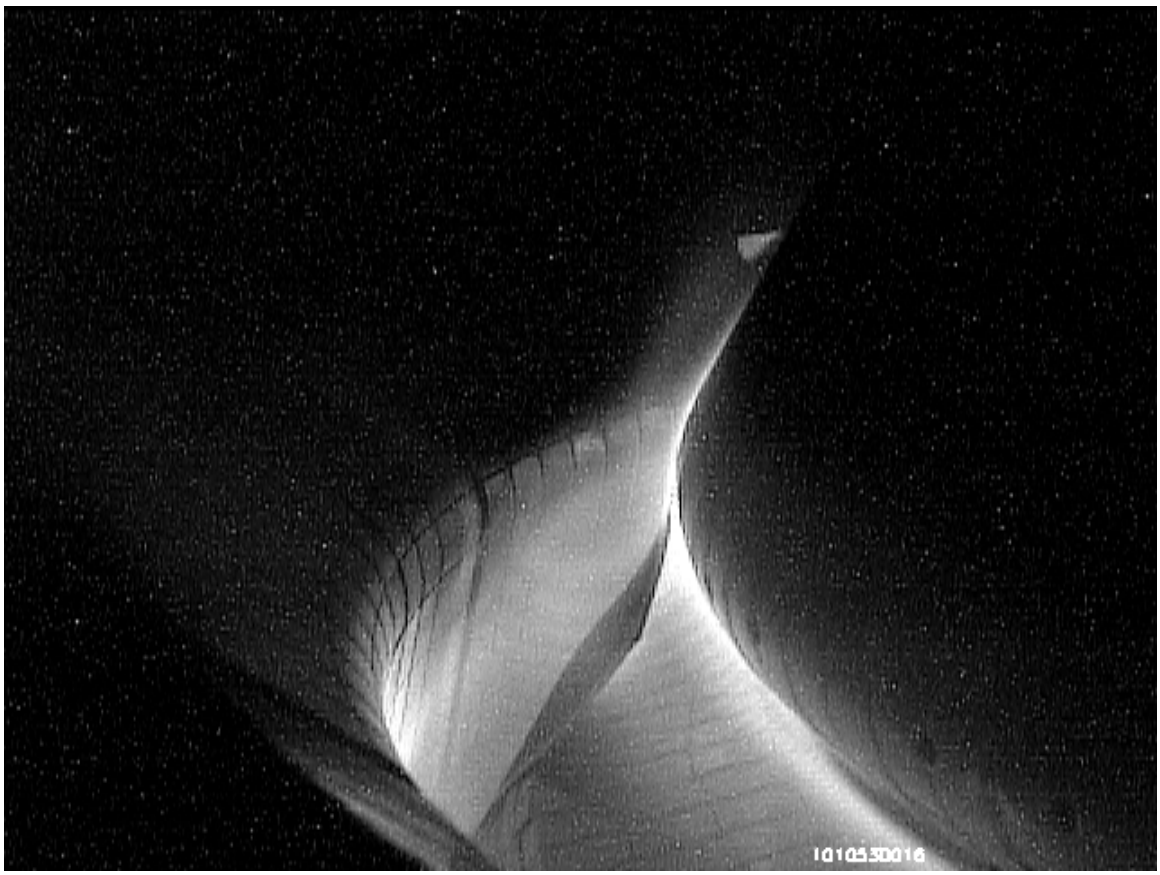

Figure 4-58: An image from the divertor viewing camera showing the final resting place of the visible bremsstrahlung viewing dump.

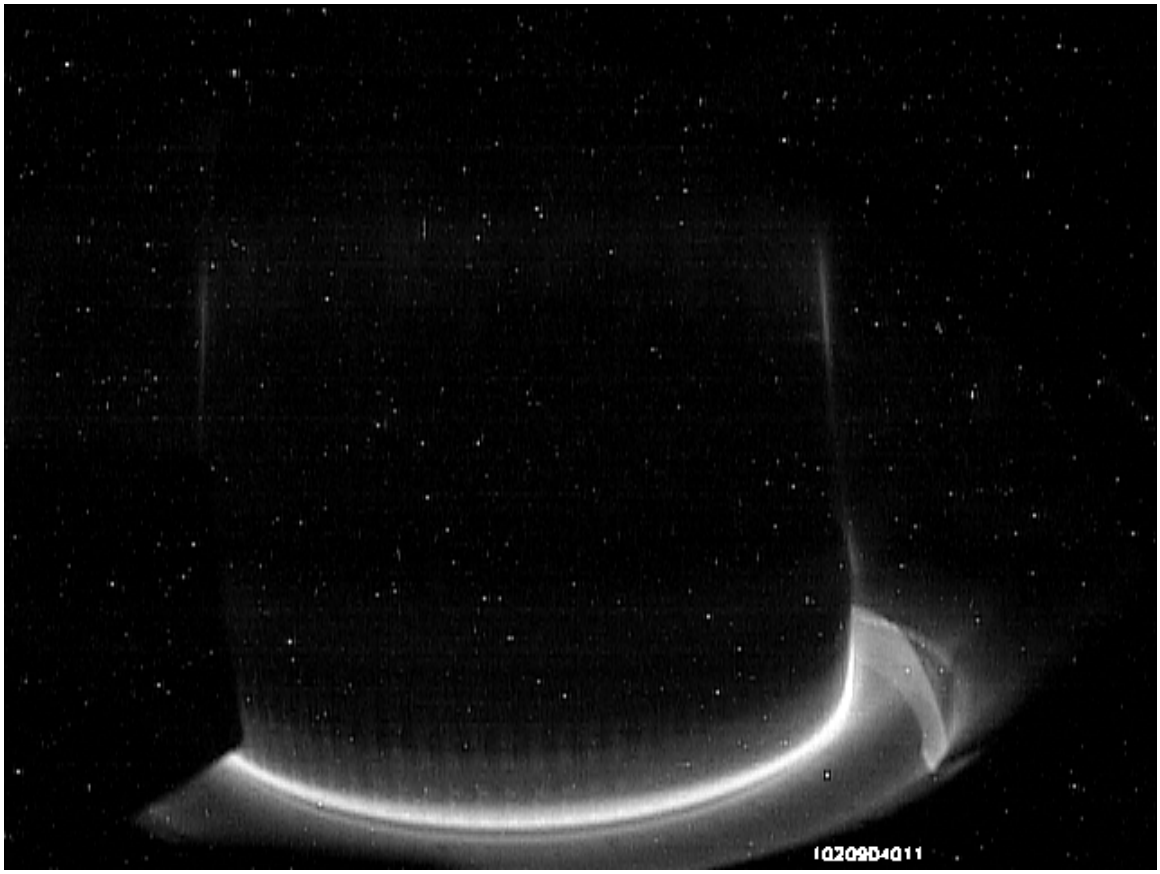

Figure 4-59: "A-port" Wide-angle view of the vacuum vessel before the boron nitride protection tiles fell into the divertor.

rest of the support structure. Once the tiles broke they fell into the divertor region and were seen by the visible imaging system. By comparing figure 4-59, before the tiles have fallen into the divertor, to figure 4-60, after the tiles have fallen into the divertor, one can see where the tiles came to rest. This failure also caused severe enough problems with the operation of the plasma discharges that a vacuum break was required to retrieve the broken tiles.

### 4.4.3 Monitor of Vacuum Vessel and Plasma Behavior

The visible imaging system is also used to monitor the vacuum vessel and plasma behavior before, during, and after the plasma discharge. Three examples of monitoring are discussed in this section:

1. during electron cyclotron discharge cleaning (ECDC),

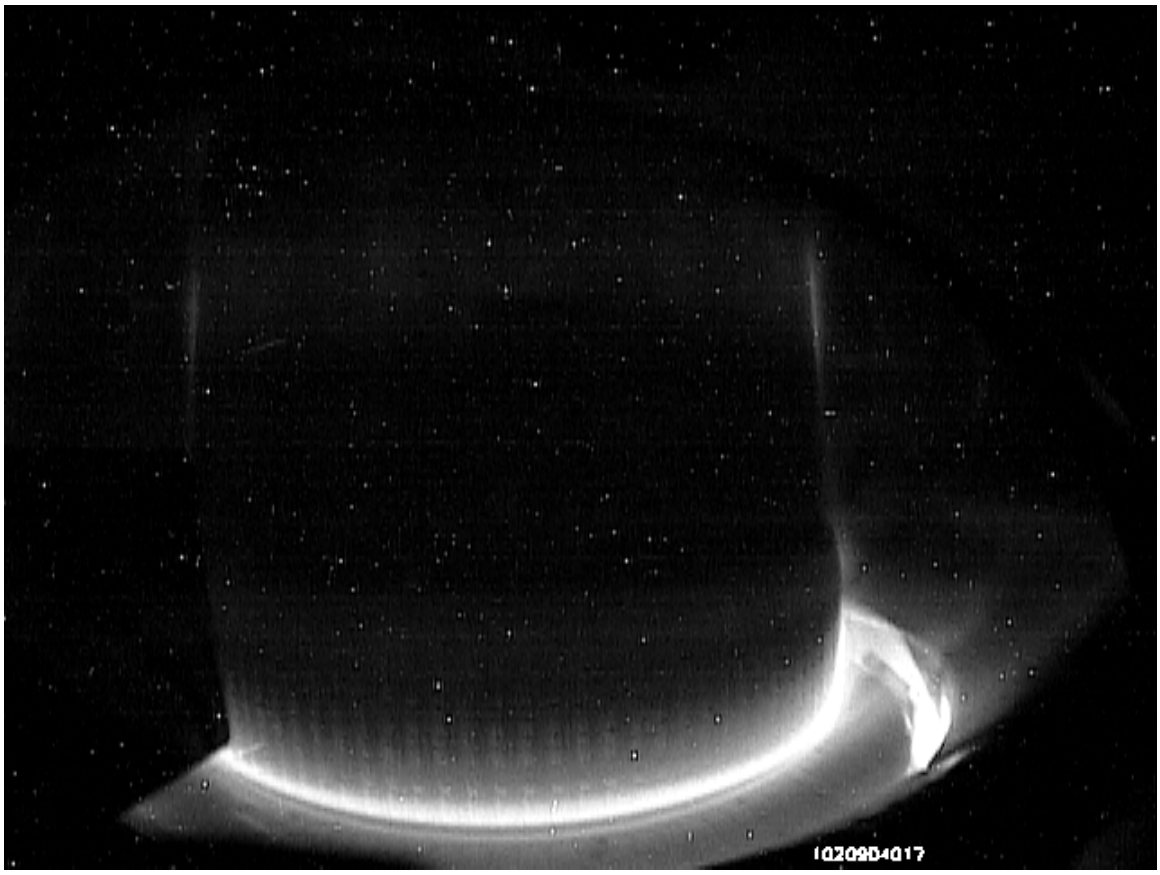


Figure 4-60: "A-port" Wide-angle view of the vacuum vessel after the boron nitride protection tiles fell in to the divertor. The outline of the boron nitride tiles can seen in the lower right of the divertor structure.

2. during a plasma discharge, and

3. after a disruption

In an effort to rid the vacuum vessel surfaces of $D_2O$, $O_2$, etc., prior to the running of research plasma discharges, ECDC is conducted each day before the discharge plasmas begin. In ECDC a low density plasma is created by launching into the vacuum vessel microwaves with a frequency at the cyclotron frequency for electrons with a low value of the toroidal magnetic field (0.08 T). The toroidal magnetic field is then scanned in magnitude moving the cyclotron resonance layer across the entire vacuum vessel. This allows the plasma to impact all the material surfaces in the vacuum vessel. This scanning of the plasma is monitored by the visible imaging system to check the extent and rate of the sweeping of the electron cyclotron resonance layer.

The plasma and vacuum vessel are also monitored during plasma discharges. The images recorded during plasma discharges give an immediate feedback to the operations staff as to how well the plasma behaved. This survey view is also able to indicate whether there has been a transition to high confinement mode (H-mode) or an internal transport barrier (ITB). By comparing figure 4-61, which is a standard L-mode discharge, to figure 4-62, which is an H-mode discharge, one can determine visually that an H-mode was achieved. The increased brightness in figure 4-62 is due to an increase in bremsstrahlung emission from the core region of the plasma due to an increase in plasma density during H-mode operation. By comparing figure 4-61 to figure 4-63, which is a discharge with an internal transport barrier, one can determine visually that a particle internal transport barrier has been achieved. The internal transport barrier is visually identifiable by a small torus of enhanced emission over the standard L-mode emission pattern. This enhanced emission is due to the increase in bremsstrahlung emission because of the increase in density inside the internal transport barrier.

The visible imaging system continues to record after the discharge has ended, and therefore has been able to record "sparks" generated by the disruption of a plasma discharge. These "sparks" are similar to those seen during a discharge except that

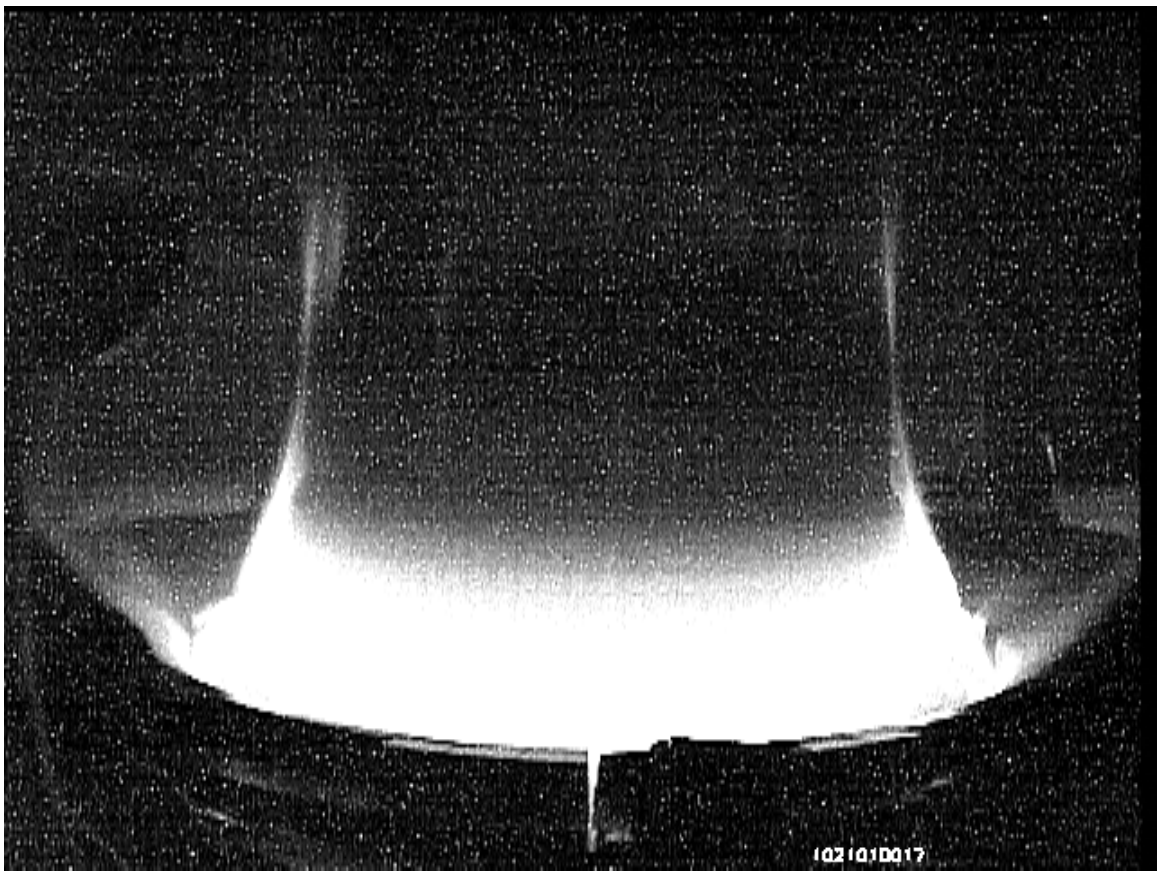


Figure 4-61: Sample image of a standard L-mode discharge as viewed from the "F-port" wide-angle viewing camera.

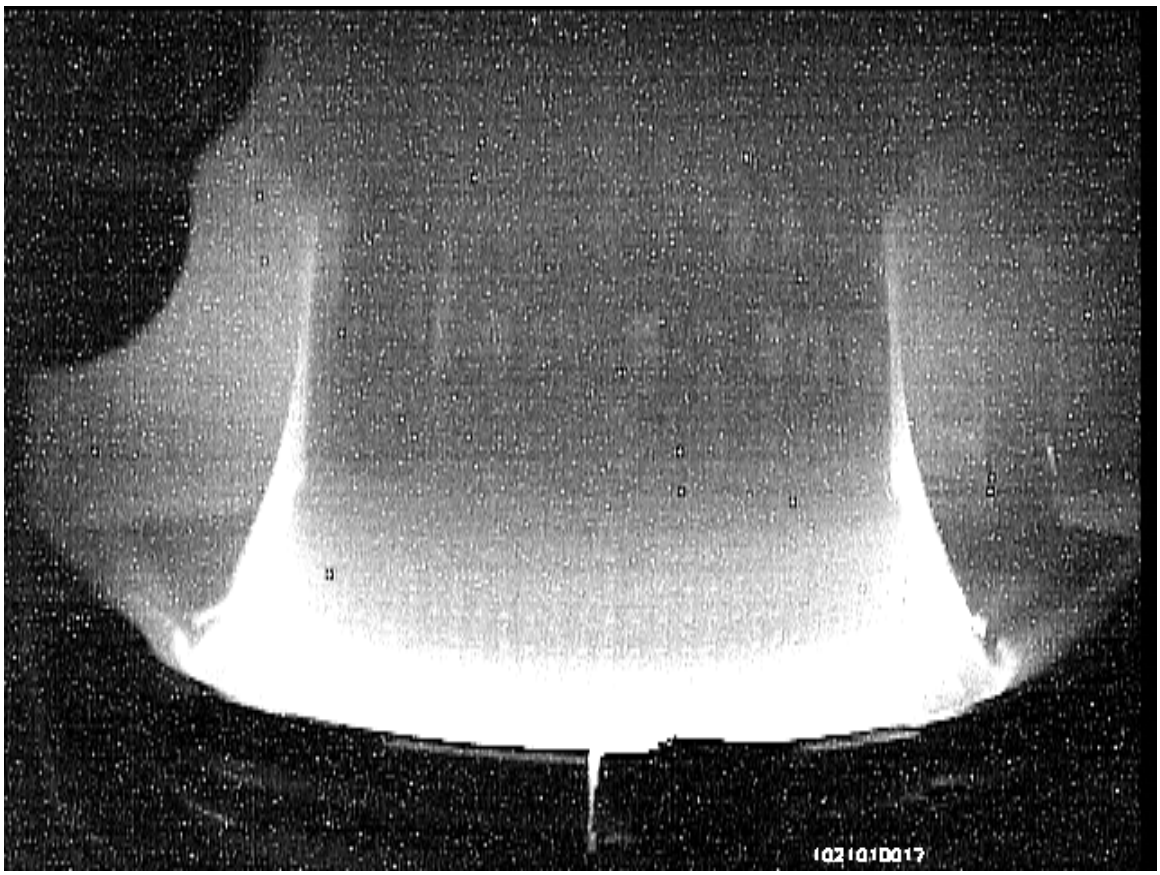


Figure 4-62: Sample image of a standard H-mode discharge as viewed from the "F-port" wide-angle viewing camera.

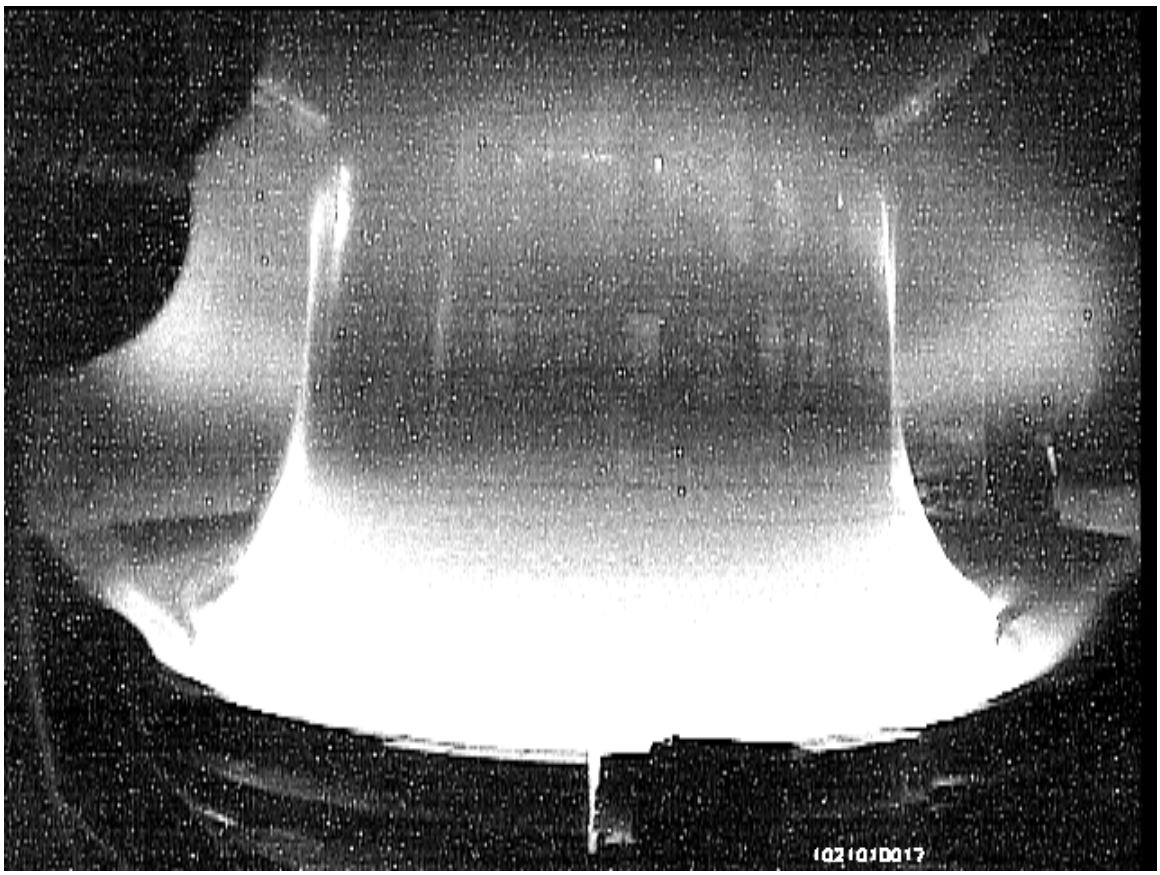


Figure 4-63: Sample image of an internal transport barrier discharge as viewed from the "F-port" wide-angle viewing camera.

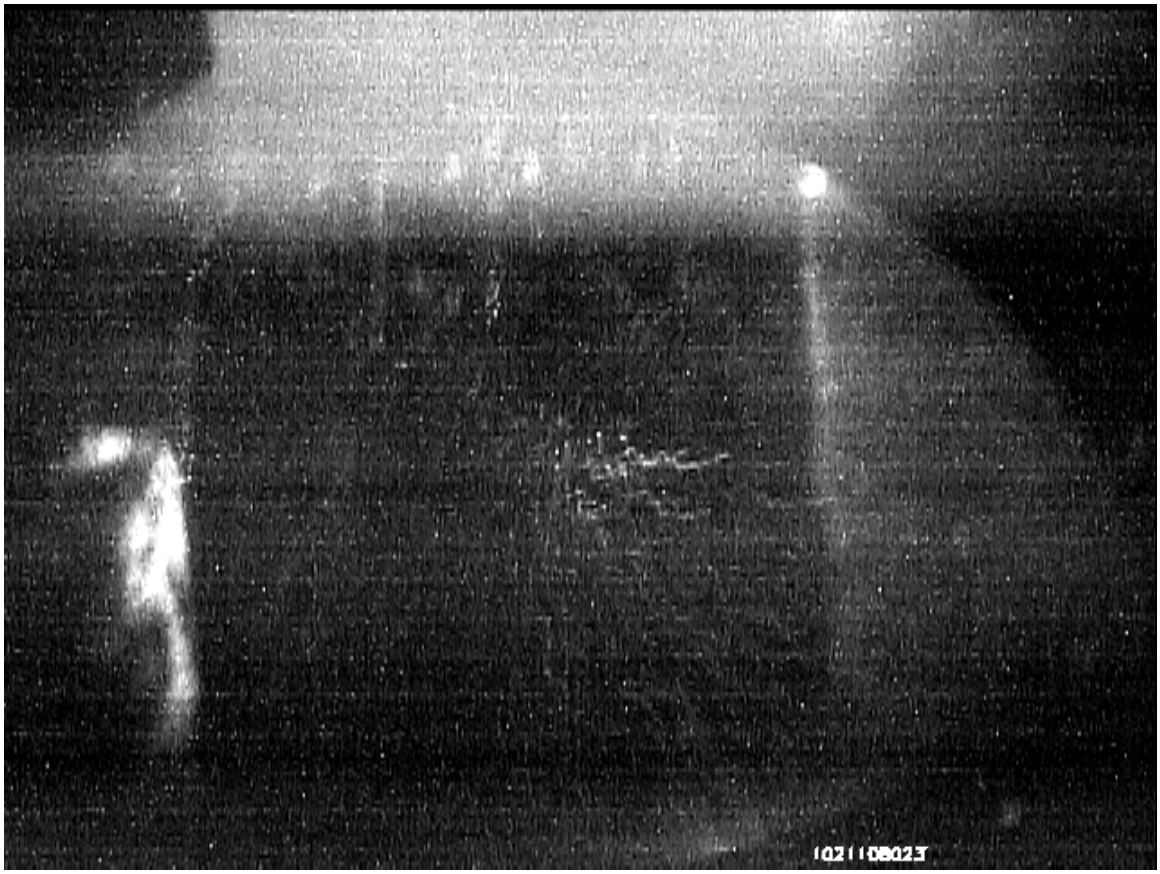

Figure 4-64: Typical image of "sparks" occurring after a discharge plasma disruption as viewed from a wide-angle viewing camera.

they occur after the plasma has been extinguished. The only way to locate where the post-discharge "sparks" originating from is by following the trail of the debris backwards in time and comparing where trail originates from to a pre-disruption image. Figure 4-64 shows the typical image of "sparks" that occur after a discharge plasma disruption.

# Chapter 5

# Summary

This dissertation has focussed on the development of and results from a visible imaging system on the Alcator C-Mod tokamak for the purpose of addressing the value of this system as both a qualitative and quantitative diagnostic of magnetically confined plasmas. The development of the visible imaging system has been addressed in sections 4.1 and 4.2, which include the discussions of the physical setup and data analysis techniques. A number of results obtained by using this system, as well as a discussion of the operational benefits, are described in detail in sections 4.3 and 4.4.

The visible imaging system on Alcator C-Mod consists of six CCD cameras. The entire visible imaging system is on the air side of the vacuum vessel allowing for changes and maintenance to be done without requiring a vacuum break. The cameras are recorded at 60 images per second with an exposure time that can be varied from 0.1 to 16.7 ms. Two of these cameras view the divertor region tangentially, two view RF antenna structures and two are used as a wide-angle survey of the vacuum vessel. All of these cameras can be filtered for a specific spectral region and calibrated to generate absolute brightness profiles from recorded images. The calibrated images from the divertor viewing cameras are then used to generate two dimensional emissivity profiles of the spectral region for which they are filtered.

The calibrated images recorded by the divertor viewing cameras are used to generate emissivity profiles by mapping the individual pixels' views through the divertor region and numerically solving the set of overdetermined linear equations. The pixels'

views are mapped to an emissivity grid defined on a poloidal plane. This mapping is done by assuming that the emission is toroidally symmetric and by using the thin chord approximation. The relation between the brightness measurement and the emission in each grid element is an overdetermined linear set of equations that are solved, in a least squares sense, using the conjugate-gradient method. This process has been optimized for the physical system used on Alcator C-Mod.

A number of phenomena were investigated using the quantitative information provided by the camera images. Three are described in detail.

Using the technique and physical setup described in sections 4.1 and 4.2 the volumetric recombination rate profiles have been measured and found to have a structure that depends on a poloidal temperature gradient in the outer scrape-off layer. The two dimensional volumetric recombination rate profiles where obtained using $D_\gamma$ emissivity profiles from the visible imaging system and electron density and temperature measurements from Langmuir probes and visible spectroscopy. Significant recombination was observed in the private flux region of the divertor during moderate density discharges ($\bar{n}_e \sim 0.8-1.9\times10^{20}$ m$^{-3}$). This meant that there was a significant density of plasma inside the PFZ, an unexpected observation. Using Braginskii's equations and deriving a radial drift, it was determined that the temperature gradient along the outer divertor leg could generate the flux of plasma consistent with the recombination rate observed in the private flux region.

A sharp break in the slope of the radial density profile was found at the location of the secondary separatrix near the inner wall of Alcator C-Mod using $D_\alpha$ emissivity profiles from the visible imaging system and a kinetic neutral code (KN1D [32]). The $D_\alpha$ emission was found to peak on the secondary separatrix. The decay lengths of the $D_\alpha$ emission was found to depend on either the neutral mean-free-path (emission decay length towards the plasma core) or as the electron density (emission decay length towards the inner wall). This decay length towards the inner wall begins at the secondary separatrix and is found to be shorter then the decay length on the same flux surfaces on the low-field-side of the plasma core. Recent Langmuir probe measurements from the inner wall region have confirmed the result found here.

Two dimensional emissivity profiles of the visible continuum (420-430 nm) have been measured and found to be an order of magnitude too large when compared to expected levels from electron-ion bremsstrahlung and radiative recombination based on measured values of electron densities and temperatures. Various atomic and molecular processes were considered as processes that might account for the enhanced continuum levels. The atomic processes included: electron-atom bremsstrahlung, $H^-$ attachment, ion-atom bremsstrahlung, and $H_2^+$ attachment. For these processes to generate the level of continuum observed, the atomic density would have to be two orders of magnitude larger than the electron density. The molecular process considered is a radiative dissociation of the deuterium molecule ($a^3\Sigma_g^+ \rightarrow b^3\Sigma_u^+$). The deuterium molecule can decay radiatively from an excited electronic state into an unbound electronic state, thus dissociating the molecule and generating continuum emission. Two mechanisms for populating the excited state were considered, excitation from ground and cascading decays from $H_2^+$ volume recombination. With both of these mechanisms it was estimated that the $H_2$ and the $H_2^+$ densities would need to be on the same order of the electron density, if the molecular process is the cause of the enhanced continuum. All the above mentioned processes require densities (molecular, atomic, and molecular ion) that are too high when compared to those predicted by divertor plasma modelling, therefore it is not likely that any of these processes are the cause of the observed continuum emission in the divertor and the cause remains unknown.

In addition to these scientific results the visible imaging system has significant operational benefits. The system has been used in identifying the causes of impurity injections during discharges, in identifying the failure of invessel components, and as a general monitor of vessel and plasma behavior. There are three main causes of impurity injection in Alcator C-Mod. The injections typically either originate from the RF antenna structure, the Langmuir scanning probes or from the molybdenum protection tiles that line the inside of the vacuum vessel. All of these types of injections have been observed and are monitored by the visible imaging system. This system has been useful in identifying when certain invessel components fail. Three specific

incidents were noted, the bending of a viewing dump, the complete dislocation of a viewing dump, and the breaking and falling of boron nitride protection tiles from an RF antenna structure. In its capacity as a vacuum vessel and plasma behavior monitor, the system is used to observe during electron cyclotron discharge cleaning, during, and after the discharge, and sometimes recording the flight of debris around the vacuum vessel after a disruption.

## 5.1 Conclusions

The research question of chapter 3 – Can visible imaging spectroscopy be a valuable qualitative and quantitative diagnostic for magnetically confined plasmas? – has been answered in the affirmative in chapter 4 by the following new results:

**The measurement of significant plasma recombination in the private flux region of the Alcator C-Mod divertor is explained by a radial flux of plasma generated by a poloidal temperature gradient.** Using spectroscopic measurements we observe that there is a significant recombination rate in the private flux zone. This requires significant plasma flux to this region. From Braginskii's equations a cross-field radial drift is derived to explain the existence and behavior of the private flux region plasma. The dominant drift is interpreted as due to a poloidal temperature gradient. The flux from this drift is consistent with attached case of the outer divertor where the recombination rate in the private flux region is found to be approximately linear with the strike point pressure. This plasma flux is also consistent with the observed behavior of the volumetric recombination rate in the various regions of the divertor (inner divertor, outer divertor, and private flux region).

**The measurement of location and shape of the $D_\alpha$ emission near the inner wall is explained by a sharp break in slope of the radial density profile at the secondary separatrix.** The location of the emission and the independence of the emission scale length on the high-field side of the secondary separatrix is explained by a sharp decay of the plasma density beginning at the secondary separatrix and

decreasing toward the inner wall. This agrees with the generally-accepted scrape-off layer paradigm, in which all the plasma flows *along* magnetic field lines to the divertor plate and the radial plasma profiles are determined by this parallel transport. The difference between the SOL paradigm and the observation is that the SOL paradigm is expected to begin at the primary, *not* the secondary separatrix. Also, this effect is only seen on the high-field side of the plasma and not the low-field side. This sharp decay in the region between the secondary separatrix and the inner wall implies that during double null discharges the neutrals from the inner wall region can enter the closed flux surfaces more readily due to reduced screening by the plasma. This also implies that during double null discharges impurities from the inner wall region can enter the plasma more easily, contaminating the core plasma. The emission scale length on the low-field side of the secondary separatrix is explained by the ionization mean-free-path of the neutrals into the common scrape-off layer. This scale length is therefore a measure of the effective ionization mean-free-path for the neutrals originating at the secondary separatrix.

**The continuum emission in the divertor of Alcator C-Mod cannot be explained by any atomic or molecular process considered in this dissertation, unless the density of the atomic deuterium, molecular deuterium, or the ionized molecular deuterium is significantly above values predicted by divertor plasma models.** The visible continuum emission in the divertor of Alcator C-Mod is an order of magnitude above that expected from electron-ion bremsstrahlung and radiative recombination, using measured values of electron temperature and density. The atomic processes considered to explain this discrepancy include electron-atom bremsstrahlung, $D^-$ attachment, ion-atom bremsstrahlung, and $D_2^+$ attachment. For the atomic process to account for the continuum measured the atomic density must be two orders of magnitude above the electron density. The molecular process considered is the radiative dissociation process of the $a^3\Sigma_g^+$ state decaying into the repulsive state $b^3\Sigma_u^+$. Two population mechanisms, excitation from ground state and recombination of $D_2^+$, were considered to populate the $a^3\Sigma_g^+$ state. For either population mechanism to yield the observed continuum the densities re-

quired were on the order of the electron density ($10^{21}$ $m^{-3}$). All of these densities are over two orders of magnitude above the densities predicted by divertor plasma models. Thus the enhanced continuum remains unexplained.

**The visible imaging system has significant benefits on the operation of the Alcator C-Mod tokamak.** The visible imaging system has been used in identifying the causes of impurity injections during plasma discharges, in identifying the failure of invessel components, and as a general monitor of the vessel and plasma behavior. The examples of observed impurity sources include the RF antenna, the scanning Langmuir probes and the molybdenum protection tiles. Some failed invessel components have been observed and include viewing dumps and boron nitride protection tiles from the RF antenna structure. The cameras have also been useful in observing the behavior of the plasma by providing a visual identification of the L-Mode, H-Mode and ITB plasma operation.

## 5.2 Future Work

In the course of developing and operating the visible imaging system on Alcator C-Mod several questions have arisen that this system can address in a substantial way:

**What is the cause of the strong plasma flow towards inner wall MARFE's?** A MARFE or Multifacited Axisymetric Radiation From the Edge [38, 53, 21] is a region of cold dense plasma typically located in a toroidal band about the inner column of a tokamak. Alcator C-Mod has a gas capillary located on the midplane of the inner column. Experiments have been conducted where a MARFE forms near the inner column and the capillary is puffing deuterium. The observation, during these discharges, is that when this gas from the capillary interacts with the plasma and the gas emits deuterium line radiation having a comet-like structure where the "tail" always points along a magnetic field line towards the MARFE. Figures 5-1 and 5-2 show the MARFE and the plume generated when the MARFE is located above and below the capillary. It is assumed that the comet-like structure is caused by plasma flows dragging the neutral gas along with it, leading to the question: what is the

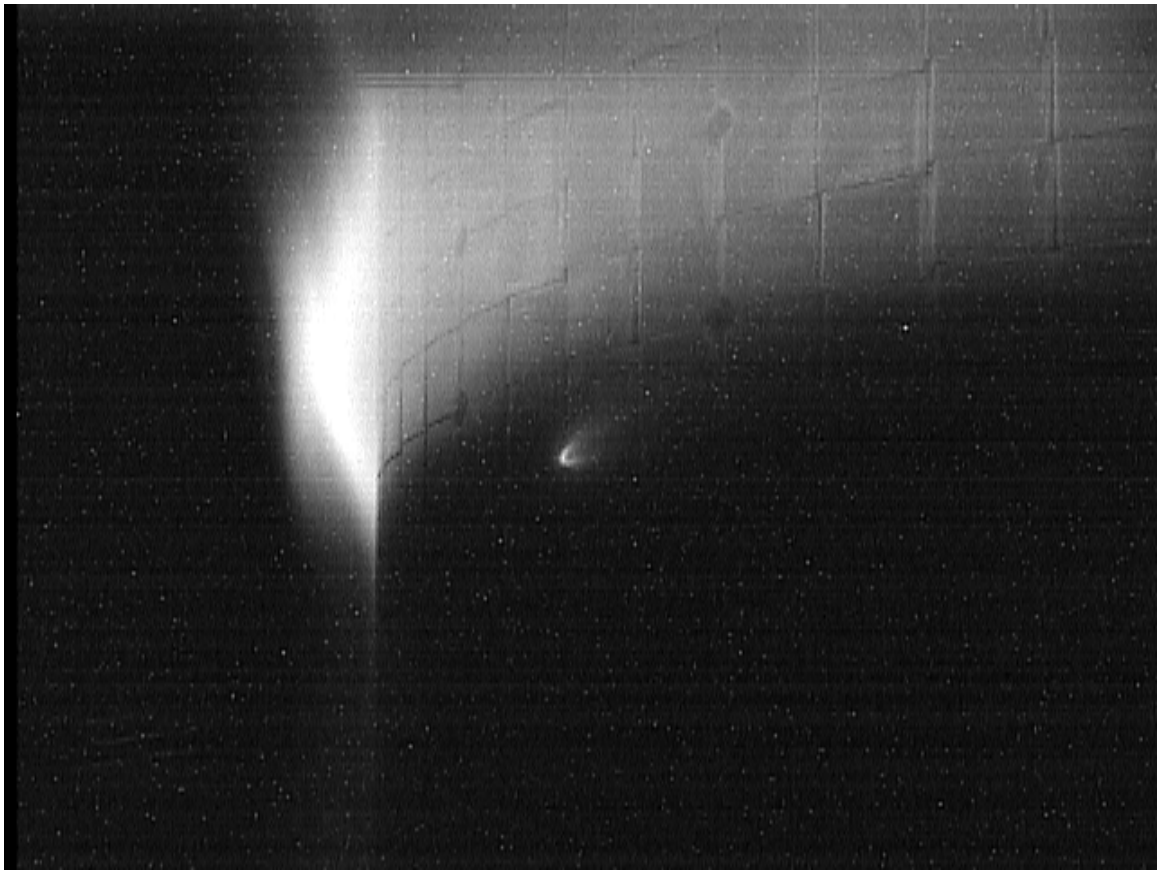

Figure 5-1: Recorded image of the inner wall showing the plume from a gas puff with the MARFE above the gas puff and the plume tail pointing towards the MARFE.

cause of the strong plasma flow towards the MARFE's?

**Why is there a region of strong $D_\gamma$ emission in closed flux surfaces during high density discharges?** In recent density disruption experiments the formation of a region with significant $D_\gamma$ emission was formed inside the closed flux region. These experiments were nearly double null, but still having a lower single null. This region formed shortly after the inner wall gas puff began and remained for the remainder of the discharge. Figure 5-3 shows the emissivity profile of the $D_\gamma$ emission at a time shortly after this region was formed.

**What is the difference in performance between the old (pre-2002) divertor structure and the new (post-2002) divertor structure?** Between the campaign of 2001 and 2002 on Alcator C-Mod a new inner divertor structure was installed. This new structure creates a more open divertor. The performance differ-

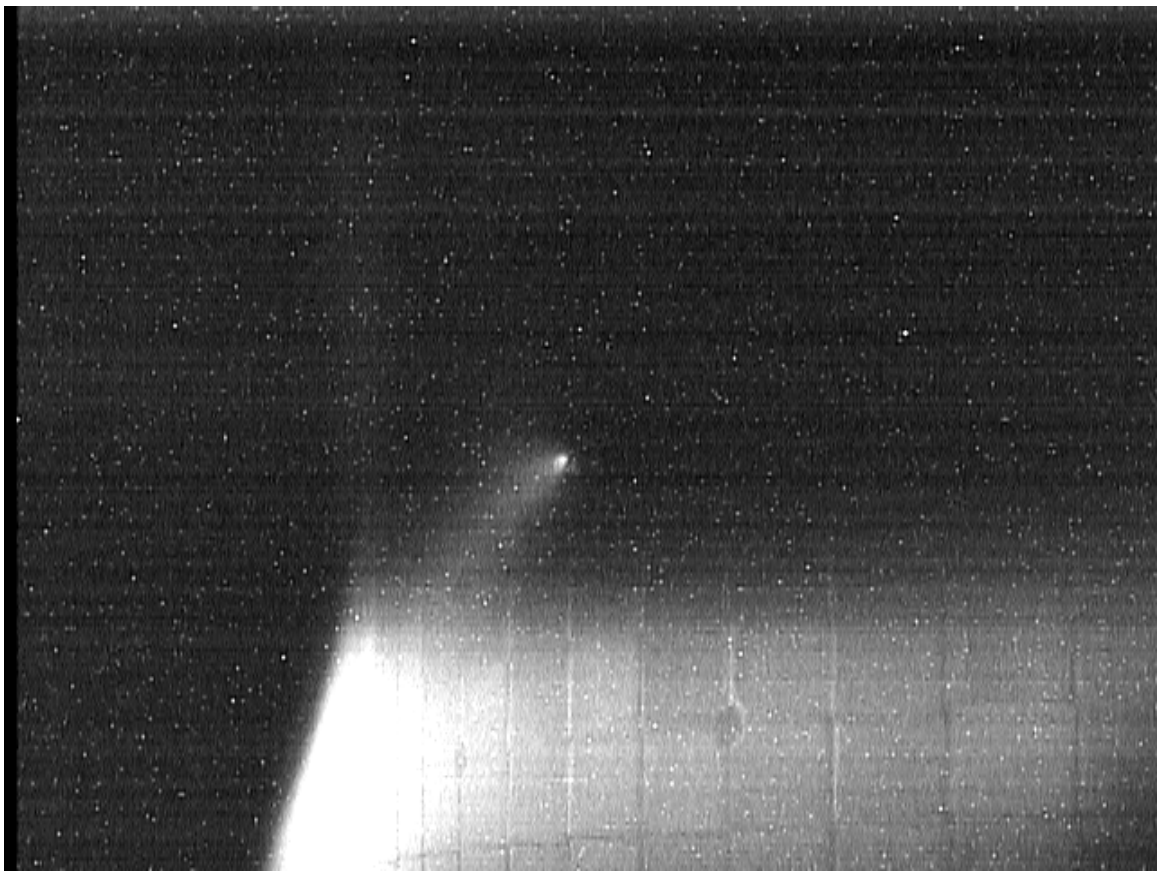

Figure 5-2: Recorded image of the inner wall showing the plume from a gas puff with the MARFE below the gas puff and the plume tail pointing towards the MARFE.

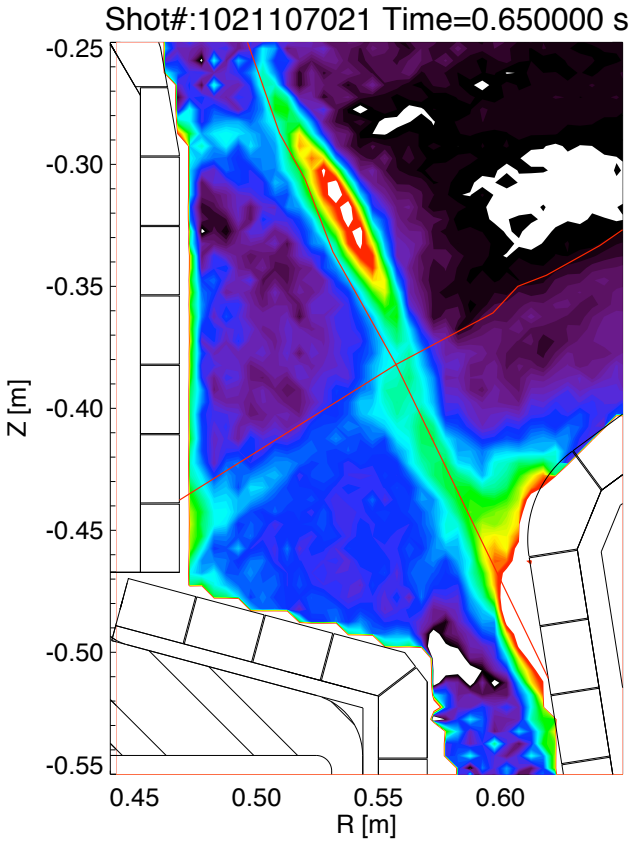


Figure 5-3: Two dimensional profile of $D_\gamma$ emission shortly after the the emission in the closed flux surfaces is formed.

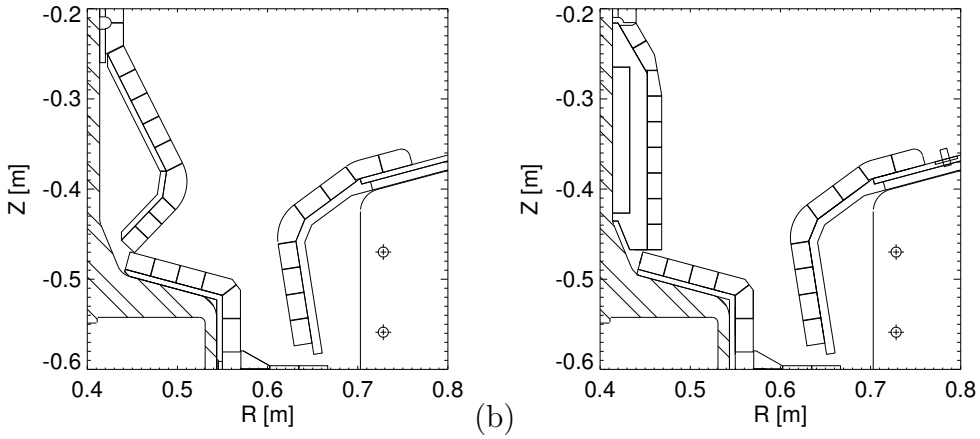


Figure 5-4: The divertor structure (a) before the 2002 campaign and beginning with the 2002 campaign.

ences have not been studied in detail. The visible imaging system can be a significant diagnostic in determining differences by comparing the emission profiles of two similar discharges with different divertor structures. Figure 5-4 and shows the old and new divertor structures.

**What is the cause of the visible continuum observed in the divertor of Alcator C-Mod?** This dissertation shows that the continuum is not due to any atomic continuum generating processes and is probably not due to the molecular processes considered. It is therefore likely that it is due to a process, probably involving molecules, that has not been considered. The visible imaging system could be used to help determine the cause of the continuum, by being filtered for different spectral regions and by observing the continuum levels in a helium plasma.

# Bibliography

[1] Aaron Allen. Capture, storage, and analysis of video images on the alcator c-mod tokamak. Master's thesis, Massachusetts Institute of Technology, February 1997.

[2] R. Aymar, V. A. Chuyanov, M. Huguet, Y. Shimomura, ITER Joint Central Team, and ITER Home Teams. Overview of iter-feat – the future internation burning plasma experiment. *Nuclear Fusion*, 41(10):1301–10, 2001.

[3] D. R. Bates, Kathleen Ledsham, and A. L. Stewart. Wave functions of the hydrogen molecular ion. *Philosophical Transactions of the Royal Society of London. Series A, Mathematical and Physical Sciences*, 246(911):215–240, 1953.

[4] T. J. Birmingham, J. M. Dawson, and R. M. Kulsrud. Contribution of electron-electron collisions to the emission of bremsstrahlung by a plasma. *Physics of Fluids*, 9(10):2014–2025, Oct 1966.

[5] S. I. Braginskii. Transport processes in a plasma. In *Reviews of plasma physics. Vol. I.*, pages 205–311. Consultants Bureau, New York, N. Y., 1963.

[6] T. Brown, R. Ellis, H. M. Fan, P. Heitzenroeder, C. Kesser, D. Meade, C. Neumeyer, J. Schmidt, R. Woolley, K. Young, I. Zatz, J. Schultz, R. Thome, P. Titus, I. Burgess, B. Nelson, D. Swain, M. Gouge, G. Johnson, R. Bulmer, M. Ulrickson, H. Khater, M. Sawan, D. Petti, B. Merrill, L. Cadwallader, D. Dilling, D. Driemeyer, F. Cole, L. Waganer, C. Baxi, J. Wesley, V. Christina, E. Peterson, F. Tepes, A. Berger, and J. Rathke. Fusion ignition research ex-

periment - fire - engineering status report for fiscal year 2001. Technical report, Princeton Plasma Physics Laboratory, Jan 2002.

[7] T. F. Chan. An improved algorithm for computing the singular value decomposition. *ACM Trans. Math. Soft.*, 8:72–83, 1982.

[8] A. S. Coolidge. Experimental verification of the theory of the continuous spectra of $h_2$ and $d_2$. *Physical Review*, 65(7–8):236–246, Apr 1944.

[9] A. S. Coolidge and H. M. James. Wave functions and potential curves for excited $h_2$. *Journal of Chemical Physics*, 6:730–734, 1938.

[10] M. Daskhan and A. S. Ghosh. Photodetachment cross section of the negative hydrogen ion. *Physical Review A*, 28(5):2767–2769, Nov 1983.

[11] R. O. Doyle. The continuous spectrum of the hydrogen quasi-molecule. *J. Quant. Spectrosc. Radiat. Transfer*, 8:1555–1569, 1968.

[12] M. Endler, H. Niedermeyer, L. Giannone, E. Holzhauer, A. Rudyj, G. Theimer, N. Tsois, and ASDEX Team. Measurements and modelling of electrostatic fluctuations in the scrape-off layer of asdex. *Nuclear Fusion*, 35(11):1307–1339, 1995.

[13] U. Fantz, B. Schalk, and K. Behringer. Calculation and interpretation of the contiuum radiation of hydrogen molecules. *New Journal of Physics*, 2, 2000.

[14] M. E. Fenstermacher, S.L. Allen, T.E. Evans, D.N. Hill, R.C. Isler, C.J. Lasnier, A.W. Leonard, T.W. Petrie, G.D. Porter, W.P. West, D.G. Whyte, and R.D. Wood. Evolution of 2d deuterium and impurity radiation profiles during transitions from attached to detached divertor operation in diii-d. *Journal of Nuclear Materials*, 266–269:348–351, 1999.

[15] M. E. Fenstermacher, W. H. Meyer, R. D. Wood, D. G. Nilson, R. Ellis, and N. H. Brooks. A tangentially viewing visible tv system for the diii-d divertor. *Review of Scientific Instruments*, 68(1):974–977, jan 1997.

[16] G. H. Golub and Reinsch C. Singular value decomposition and least squares solutions. *Numer. Math.*, 14:403–420, 1970.

[17] G. H. Golub and C. F. Van Loan. *Matrix Compuations*. The Johns Hopkins University Press, Baltimore, Maryland, 1983.

[18] Hans R. Griem. *Principles of Plasma Spectroscopy*, volume 2 of *Cambridge Monographs on Plasma Physics*. Cambridge University Press, Cambridge, UK, 1997.

[19] M. R. Hestenes and E. Stiefel. Methods of conjugate gradients for solving linear systems. *J. Res. Nat. Bur. Stand.*, 49:409–436, 1952.

[20] F. L. Hinton and G. M. Staebler. Collisional transport near the separatrix of a tokamak and the h-mode. *Nuclear Fusion*, 29(3):405–414, 1989.

[21] I. H. Hutchinson. Thermal front analysis of detached divertors and marfes. *Nuclear Fusion*, 34(10):1337–1348, 1994.

[22] I. H. Hutchinson, B. LaBombard, J. A. Goetz, B. Lipschultz, G. M. McCracken, J. A. Snipes, and J. L. Terry. The effects of field reversal on the alcator c-mod divertor. *Plasma Physics and Controlled Fusion*, 37:1389–1406, 1995.

[23] Interactive Data Language (IDL), Research Systems Inc, 4990 Pearl East Circle, Boulder, CO 80301.

[24] K. Itami, P. Coad, W. Fundamenski, C. Ingesson, J. Lingertat, G. F. Matthews, and A. Tabasso. Observation of detachment in the jet mkiigb divertor using ccd camera tomography. *Journal of Nuclear Materials*, 290-293:633–638, 2001.

[25] Keith Jack. *Video Demystified*. LLH Publishing, 3rd edition, 2001.

[26] H. M. James and A. S. Coolidge. Continuous spectra of $h_2$ and $d_2$. *Physical Review*, 55:184–190, Jan 1939.

[27] R. K. Janev and Smith J. J. Atomic and plasma-material interaction data for fusion. *Supplement to Nuclear Fusion*, 4, 1993.

[28] R. K. Janev, W. D. Langer, K. Evans, Jr., and D. E. Post, Jr. *Elementary Processes in Hydrogen-Helium Plasmas*, volume 4 of *Atoms and Plasmas*. Springer-Verlag, New York, 1987.

[29] A. S. Kukushkin, H. D. Pacher, G. Janeschitz, A. Loarte, D. P. Coster, G. Matthews, D. Reiter, R. Schneider, and V. Zhogolev. Basic divertor operation in iter-feat. *Nuclear Fusion*, 42:187–191, 2002.

[30] C. Kurz, J. A. Snipes, J. L. Terry, D. Labombard, B. Lipschultz, and G. M. McCracken. Determination of $h_\alpha$ emissivities from line integrated brightness measurements on alcator c-mod. *Review of Scientific Instruments*, 66(1):619–621, 1995.

[31] Christian Kurz. *Tomography of Light Emission from the Plasma Edge of Alcator C-Mod*. PhD thesis, Massachusetts Institute of Technology, June 1995.

[32] B. LaBombard. Kn1d: A 1-d space, 2-d velocity, kinetic transport algorithm for atomic and molecular hydrogen in an ionizing plasma. PSFC-RR-01-3.

[33] B. LaBombard, R. L. Boivin, M. Greenwald, J. Hughes, B. Lipschultz, D. Mossessian, C. S. Pitcher, J. L. Terry, and S. J. Zweben. Particle transport in the scrape-off layer and its relationship to discharge density limit in alcator c-mod. *Physics of Plasmas*, 8(5):2107–17, May 2001.

[34] B. LaBombard, D. Jablonski, B. Lipschultz, G. McCracken, and J. Goetz. Scaling of plasma parameters in the sol and divertor for alcator c-mod. *Journal of Nuclear Materials*, 220–222:976–981, April 1995.

[35] B. LaBombard and B. Lipschultz. Poloidal asymmetries in the scrape-off layer plasma of the alcator c tokamak. *Nuclear Fusion*, 27(1):81–99, 1987.

[36] B. LaBombard, M. V. Umansky, R. L. Boivin, J. A. Goetz, J. Hughes, B. Lipschultz, D. Mossessian, C. S. Pitcher, and J. L. Terry. Cross-field plasma transport and main-chamber recycling in diverted plasmas on alcator c-mod. *Nuclear Fusion*, 40(12):2041–60, Dec 2000.

[37] URS-600 Uniform Radiance Source, Labsphere, P. O. Box 70, North Sutton, NH 03260.

[38] B. Lipschultz, B. LaBombard, E. S. Marmar, M. M. Pickrell, J. L. Terry, R. Watterson, and S. M. Wolfe. Marfe: and edge plasma phenomenon. *Nuclear Fusion*, 24(8):977–989, 1984.

[39] B. Lipschultz, J. L. Terry, C. Boswell, A. Hubbard, B. LaBombard, and D. A. Pappas. Ultrahigh densities and volume recombination inside the separatrix of the alcator c-mod tokamak. *Physical Review Letters*, 81(5):1007–1010, 1998.

[40] B. Lipschultz, J. L. Terry, C. J. Boswell, J. A. Goetz, A. E. Hubbard, S. I. Krasheninnikov, B. LaBombard, D. Pappas, C. S. Pitcher, F. Wising, and S. Wukitch. The role of particle sinks and sources in alcator c-mod detached divertor discharges. *Physics of Plasmas*, 6(5):1907–1916, May 1999.

[41] B. Lipschultz, J. L. Terry, C. J. Boswell, S. I. Krasheninnikov, B. LaBombard, and D. Pappas. Recombination and ion loss in c-mod detached divertor discharges. *Journal of Nuclear Materials*, 266–269:370–375, March 1999.

[42] D. Lumma, J. L. Terry, and B. Lipschultz. Radiative and three-body recombination in the alcator c-mod divertor. *Physics of Plasmas*, 4(7):2555–2566, Jul 1997.

[43] H. A. Macleod. *Thin-Film Optical Filters*. American Elsevier Publishing Company, Inc., New York, 1969.

[44] E. S. Marmar, R. L. Boivin, R. S. Granetz, J. W. Hughes, B. Lipschultz, S. McCool, D. Mossessian, D. S. Pitcher, J. E. Rice, and J. L. Terry. High resolution visible continuum imaging diagnostic on the alcator c-mod tokamak. *Review of Scientific Instruments*, 72(1):940–943, 2001.

[45] A. A. Mihajlov and M. S. Dimitrijević. Influence of ion-atom collisions on the absorption of radiation. *Astronomy and Astrophysics*, 155:319–322, 1986.

[46] A. A. Mihajlov and M. M. Popović. Spontaneous electromagnetic radiation caused by binary ion-atom collisions in the quasiresonant case. *Physical Review A*, 23(4):1679–1687, Apr 1981.

[47] C. C. Paige and M. A. Saunders. Lsqr: An algorithm for sparse linear equations and sparse least squares. *ACM Trans. Math. Soft.*, 8(1):43–71, Mar 1982.

[48] A. Yu. Pigarov. Collisional radiative kinetic of molecular assisted recombination in edge plasmas. *Physica Scripta*, T96:16–31, 2002.

[49] A. Yu. Pigarov and S. I. Krasheninnikov. Applications of the collisional-radiative, atomic-molecular model to the recombining divertor plasma. *Physics Letters A*, 222:251–257, Nov 1996.

[50] George B. Rybicki and Alan P. Lightman. *Radiative Processes in Astrophysics*, chapter 10, pages 284–285. John Wiley and Sons, 1979.

[51] G. M. Staebler. Transport modelling of divertor bias experiments. *Nuclear Fusion*, 31(4):729–738, 1991.

[52] P. C. Stangeby and A. V. Chankin. Simple models for the radial and poloidal $e \times b$ drifts in the scrape-off layer of a divertor tokamak: Effects on in/out asymmetries. *Nuclear Fusion*, 36(7):839–852, 1996.

[53] P. C. Stangeby and G. M. McCracken. Plasma boundary phenomena in tokamaks. *Nuclear Fusion*, 30(7):1225–1379, 1990.

[54] J.A. Stillerman, T.W. Fredian, K.A. Klare, and G. Manduchi. Mdsplus data acquisition system. *Review of Scientific Instruments*, 68(1):939–942, Jan 1997.

[55] J. L. Stilley and J. Callaway. Free-free absorption coeffient of the negative hydrogen ion. *Astrophysical Journal*, 160:245–260, April 1970.

[56] D. Stotler. private communication.

[57] D. Stotler and C. Karney. Neutral gas transport modelling with degas2. *Contributions to Plasma Physics*, 34(2–3):392–397, 1994.

[58] J. L. Terry, B. Lipschultz, C. J. Boswell, Pappas D. A., A. Yu. Pigarov, S. I. Krasheninnikov, and B. LaBombard. $t_e$ measurements in the cold regions of alcator c-mod divertor plasmas. In B. Schweer, G. Van Oost, and E. Vietzke, editors, *26th EPS Conference on Controlled Fusion and Plasma Physics*, volume 23J, pages 325–328, London, UK, 1999. European Physical Society, Institue of Physics.

[59] J. L. Terry, J. A. Snipes, and C. Kurz. The visible, imaging diode arrays on alcator c-mod. *Review of Scientific Instruments*, 66(1):555–557, 1995.

[60] Toshiba IK-CU43A Camera control Unit, Toshiba IK-SM43H Remote-head camera and cable, Toshiba America Information Systems, Inc., P. O. Box 19724, Irvine, CA 92623-9724.

[61] J. C. Weisheit. Recombination in dense plasmas. *Journal of Physics B Atomic and Molecular Physics*, 8(15):2556–2564, 1975.

[62] J. G. Winans and E. C. G Stueckelberg. The origin of the continuous spectrum of the hydrogen molecule. *Proc. N. A. S.*, 4:867–871, 1928.

[63] J. G. Winans and E. C. G. Stueckelberg. The origin of the continuous spectrum of the hydrogen molecule. *Proceedings from the National Academy of Science*, 14:867–871, 1928.

[64] F. Wising, D. A. Knoll, S. I. Krasheninnikov, T. D. Rognlien, and D. J. Sigmar. Simulation of the alcator c-mod divertor with an improved neutral fluid model. *Contributions to Plasma Physics*, 36(2–3):136–139, 1996.